Indentation Response of Body Centered Cubic Molybdenum Single Crystals

MS (Research) Thesis

By

Pawar Prathamesh Chandrashekhar

DEPARTMENT OF MECHANICAL ENGINEERING

INDIAN INSTITUTE OF TECHNOLOGY INDORE

June 2021

Indentation Response of Body Centered Cubic Molybdenum Single Crystals

A THESIS

Submitted in partial fulfillment of the
requirements for the award of the degree
of
Master of Science (Research)

By

Pawar Prathamesh Chandrashekhar

DEPARTMENT OF MECHANICAL ENGINEERING

INDIAN INSTITUTE OF TECHNOLOGY INDORE

JUNE 2021

INDIAN INSTITUTE OF TECHNOLOGY INDORE

CANDIDATE'S DECLARATION

I hereby certify that the work which is being presented in the thesis entitled **Indentation Response of Body Centered Cubic Molybdenum Single Crystals** in the partial fulfillment of the requirements for the award of the degree of **MASTER OF SCIENCE (RESEARCH)** and submitted in the **DEPARTMENT OF MECHANICAL ENGINEERING, Indian Institute of Technology Indore**, is an authentic record of my own work carried out during the time period from July 2019 to June 2021 under the supervision of **Dr. Indrasen Singh**, Assistant Professor, Indian Institute of Technology Indore, India, **Dr. Eswar Prasad Korimilli**, Assistant Professor, Indian Institute of Technology Indore, India and **Dr. Swapnil D. Patil**, Lead Research Scientist,, General Electric Global Research Centre, Bangalore, India.

The matter presented in this thesis has not been submitted by me for the award of any other degree of this or any other institute.

08/10/2021

Signature of the student with date

(**Pawar Prathamesh Chandrashekhar**)

This is to certify that the above statement made by the candidate is correct to the best of my knowledge.

08-10-2021

Signature of Thesis Supervisor with date

(**Dr. Indrasen Singh**)

13.10.2021

Signature of Thesis Supervisor with date

(**Dr. Eswar Prasad Korimilli**)

13/10/2021

Signature of Thesis Supervisor with date

(**Dr. Swapnil D. Patil**)

Pawar Prathamesh Chandrashekhar has successfully given his MS (Research) Oral Examination held on 8th October 2021.

13/10/2021

08-10-2021

K. Eswara Mond

13.10.2021

16.10.2021

Signature of Chairperson (OEB) with date

Signature(s) of Thesis Supervisor(s) with date

20/10/2021

Signature of Convener, DPGC with date

Signature of Head of Discipline with date

ACKNOWLEDGEMENTS

I would like to express my sincerest gratitude to my supervisors Dr. Indrasen Singh, Dr. Eswar Prasad Korimilli and Dr. Swapnil D. Patil for giving me the opportunity to work under their supervision and suggesting the idea of this project. Without their kind encouragement and constant support, it would not have been possible to accomplish this great task. It is a great honour to work under their supervision.

I am thankful to Dr. Satyajit Chatterji and Dr. Sumanta Samal, my research progress committee members for their valuable suggestions and comments which helped me to improve my work. I am also grateful to the HOD of the Mechanical Engineering Department Dr. Santosh K. Sahu for his help and kind cooperation.

I would like to thank Prof. Neelesh Kumar Jain, Director (Officiating), IIT Indore for providing me an opportunity to explore my research capabilities at the IIT Indore.

I am thankful to Dr. Rajesh Korla and Sai Ram Goud sir, IIT Hyderabad for helping me in nanoindentation experimentation. I also like to thank the Sophisticated Instrumentation Center (SIC) and the Department of Metallurgical Engineering and Materials Science, IIT Indore for providing the experimentation facilities.

I would like to specially thank my seniors Hirmukhe sir, Ramanand sir and Harsh sir for their valuable help and constant cooperation on all occasions. I am thankful to Anurag, Sumit, Akhilesh, and Apurva for creating a great friendly working environment. I am extremely thankful to all my friends from IIT Indore, for their support and helps over the last two years.

I am grateful to my family for their continued love, support, and encouragement throughout my master's study, especially when nothing seems to work. Without them, it was impossible for me to finish this task. Finally, I would like to thank the Almighty for his unending blessing and for giving me the strength and ability to accomplish this work.

Prathamesh C. Pawar

Abstract

Molybdenum (Mo), a body-centered cubic (BCC) metal, has been found to be a potential candidate for various applications including semiconductor, defense, and medical industries, owing to their high yield (~324 MPa) and compressive strength (~400 MPa), superior fracture strength (), very high melting point (~2890 K), good thermal conductivity (~138 W/(mK) at 300 K) and exceptional corrosion resistance. Tension and compression experiments have shown that the mechanical response of Mo crystal depends on the applied strain rate, ambient temperature, and crystallographic orientations. Further, experimental and numerical studies performed on other BCC single crystals show that the hardness and pile-up patterns depend on their crystallographic orientation. It must be mentioned that most of the studies are performed on Ta, W, BCC Fe and Ti alloys, and little attention has been given to the Mo crystals. Consequently, deformation response of Mo crystals is not well understood.

Therefore, nano- and micro-indentation experiments on Mo single crystals oriented along (100), (110) and (111) are performed to understand their indentation response, in this thesis. Atomic force microscopy is used to analyze the impression of the indents. Results show that nano- as well as micro-hardness depends of the orientation, and (110) orientation offers the highest resistance to plastic deformation. Most importantly, nano-hardness decrease with increase in load. The micro-hardness is found to be lower than the nano-hardness which is attributed to the larger strain gradients during nanoindentation in contrast to the micro-indentation. Further, the micro-hardness also decreases with increasing indentation load up to 1000 mN. The nanoscale and microscale intrinsic material lengths marginally depend on crystal orientation and are found to be around 0.55-0,65 and 10.89-12.45, respectively. The pile-ups patterns produced through micro-indentation on the surfaces of (100), (110), and (111) oriented Mo single crystals have shown four-, two-, and three-fold symmetry, respectively. The crystal plasticity model proposed by Daphalapurkar et al. (2018) is implemented in commercially available software package Abaqus (6.17) by writing user element (UEL) subroutine

LIST OF PUBLICATIONS

1) Authors: Prathamesh Pawar, Raineesh Babu, Swapnil Patil, Indrasen Singh and Korimilli Eswar Prasad

   Title: Effect of crystallographic orientation on the hardness and indentation size effect in molybdenum single crystals.

   Journal: International Journal of Refractory Metals and Hard Materials (under review)

TABLE OF CONTENTS

LIST OF FIGURES

LIST OF TABLES

NOMENCLATURE

Chapter 1: Introduction and Literature review

τ	Resolved shear stress
τ_{max}	Maximum resolved shear stress
H	Hardness
P_{max}	Maximum indentation load
h	Indentation depth/displacement of the indenter
A_c	Projected contact area
h_c	Contact depth
h_{max}	Maximum indentation depth
a	Contact radius
S	Contact stiffness
E_r	Reduced modulus
E	Young's modulus
h_f	Residual indentation depth
H_0	Macro-hardness or size-independent hardness
h^*	Characteristic length scale
ρ_T	Total dislocation density
ρ_G	Density of geometrically necessary dislocations
ρ_S	Density of statistically stored dislocations
f	Correction factor
χ	Strain gradient
$\hat{l}$	Material intrinsic length scale

Chapter 3: Crystal Plasticity constitutive model and numerical implementation

F	Total deformation gradient tensor
F^e	Elastic deformation gradient tensor
F^p	Plastic deformation gradient tensor
m^α	Unit vector perpendicular to the slip plane
s^α	Unit vector along the slip direction

$s^{\mathrm{e}(\alpha)}$	Vector along the slip direction in current configuration
$m^{\mathrm{e}(\alpha)}$	Vector perpendicular to the slip plane in current configuration
l	Spatial velocity gradient
l^p	Plastic part of the spatial velocity gradient
l^e	Elastic part of the spatial velocity gradient
L^p	Plastic flow rate
D^p	Plastic parts of rate of deformation
Ω^p	The plastic spin tensor
L	Fourth-order elasticity moduli tensor
σ	Cauchy stress
τ	Kirchhoff stress tensor
τ^{α}	Schmid stress
$\dot{\tau}$	Rate of Kirchhoff stress
$\tau^{\nabla e}$	Jaumann rate of Kirchhoff stress determined using lattice spin
τ^{∇}	Material Jaumann rate of Kirchhoff stress
τ^{α}_{eff}	Effective resolved shear stress
$\tau^{e(\alpha)}$	Generalized resolved shear stress
$\dot{\gamma}_0$	Reference shear rate (RSR)
$\dot{\gamma}^{\alpha}$	Plastic slip rate on the slip system α
$\dot{\gamma}^{\beta}$	Plastic slip rate on the slip system β
g^{α}	Slip resistance of the α^{th} slip system
$h_{\alpha\beta}$	Latent hardening modulus
h_{α}	Self-hardening modulus
$q_{\alpha\beta}$	Amplification factors in the hardening
$h_{\alpha/0}$	Initial hardening modulus
$h_{\alpha/s}$	Saturation hardening modulus
$g_{\alpha/0}$	Initial slip resistance
$g_{\alpha/s}$	Saturation slip resistance
p & q	Collection of input parameters

ACRONYMS

BCC	Body Centered Cubic
FCC	Face Centered Cubic
HCP	Hexagonal Close Packed
Mo	Molybdenum
ISE	Indentation Size Effect
SGP	Strain Gradient Plasticity
AFM	Atomic Force Microscopy
IIT	Instrumented Indentation Test
GNDs	Geometrically Necessary Dislocations
SSDs	Statistically Stored Dislocations
CP	Crystal Plasticity
CRSS	Critically Resolved Shear Stress
CPFEM	Crystal Plasticity Finite Element Modeling
FEM	Finite Element Modeling
UEL	User Element
GA	Genetic Algorithm

Chapter 1

Introduction and Literature Review

1.1 Introduction

Molybdenum (Mo), a refractory BCC metal, is a potential material for several industrial applications due to its fascinating material properties like high yield and compressive strength (~324 and ~400 MPa), good elasticity modulus (~325 GPa), superior fracture strength, very high melting point (~2890 K), good thermal conductivity (~138 W/(mK) at 300 K, excellent density (~ 10200 kg/m^3) and exceptional corrosion resistance (MaTecK Germany; Lunk and Hartl, 2017). Therefore, Mo is considered to be a good candidate for various applications such as semiconductor and solid-state devices, aerospace and defense components, automobile parts and medical equipment (Shields, 2013; Lunk and Hartl, 2017). Tension and compression experiments have shown that the mechanical response of Mo crystal depends on the applied strain rate, ambient temperature, and crystallographic orientations (Guiu and Pratt, 1966; Sherwood et al., 1967; Irwin et al., 1983).

The hardness experiments performed on various BCC metals such as Tantalum, Titanium alloys, Tungsten single crystals have shown that the hardness of these material depends on the crystallographic orientation. Further, the hardness is found to drop with increase in indentation load which is referred to as indentation size effect (ISE). Moreover, the pile-up patterns on the indented surfaces are affected by crystal as well as azimuthal orientation of the indenter. Despite the abundance of published literature on BCC single crystals, little work has been devoted in understanding the indentation response of Mo single crystals. Therefore, the deformation behavior, in particular the indentation response of Mo single crystals is not well understood. The following questions pertaining to the indentation response of Mo single crystals arise which need to be addressed before deployment of these materials: what is the effect of crystallographic orientations on the hardness of Mo crystals? Do Mo crystals show indentation size effect irrespective of their orientation, or is it noticeable only on few selected plane/orientations? In order to address these questions, nano- and micro-indentation hardness experiments on Mo single crystals are performed

in this thesis. Atomic force microscopy (AFM) is used to examine the shape and extent of the material pile-up. An effort has also been made to implement a crystal plasticity constitutive model in commercially available software package Abaqus (6.17) so that the complementary finite element (FE) simulations of indentation could be performed in the future.

1.2 Crystallography

The solid materials can be classified as crystalline and non-crystalline, based on the arrangement of their atoms. The atoms are arranged in a periodic manner over large atomic distances in a crystalline material, while the arrangement of atoms in a non-crystalline solid is random or non-periodic in nature. Almost all metals, some polymers and many ceramics are crystalline in nature under normal solidification conditions. Most of the metals solidify into one of the following three cubic crystal structures:

- Face Centered Cubic (FCC)
- Body Centered Cubic (BCC)
- Hexagonal Close Packed (HCP)

The arrangements of atoms in unit cells of these cubic structures are illustrated in Figure l.1. The planes and directions in FCC and BCC crystals are specified with respect to an orthogonal coordinate system with origin at a corner of unit cell in terms of *miller indices*. A crystallographic plane is specified as the reciprocal of the length of its intercept on three axes which are reduced to a lowest denominator and represented as (*hkl*). For example, the miller indices for plane PQRS in Figure 1.1(a) and (b) are (010). The group of crystallographically equivalent planes are referred to as family of planes and are represented by {*hkl*}. The family of planes {100} represent six crystallographic planes (100), (010), (001), $(\bar{1}00)$, $(0\bar{1}0)$ and $(00\bar{1})$. A direction is represented as [*uvw*], where *u*, *v* and *w* are the projection of a direction along three axes reduced to a lowest denominator. For example, the direction, OQ in unit cell in Figure. 1.1(a) and (b) is represented by [111]. The family of directions are represented by <*uvw*>. By contrast, the planes and directions in an HCP crystal are represented using Miller-Bravais system with four indices *h, k, i* and *l* based on the four axes, a_1, a_2 a_3 and a_4 as shown in Figure 1.1(c). Here, the third index $i = -(h + k)$.

Further, HCP and FCC structures are closed packed structures because atomic packing density is 74% in these two cases. On the other hand, atomic packing density for BCC is only 68% and

hence it is not a closed packed structure. The plastic deformation generally takes place in a plane with highest atomic densities which are also referred to as *close-packed planes*. The closed packed planes for FCC and HCP are octahedral planes {111} and basal planes {0001}, respectively. However, there is no one plane with predominant atomic density in the case of BCC crystals. The directions <110>, <111> and <1120 > are the direction with maximum atomic density and hence referred to as close-packed direction in FCC, BCC and HCP crystals, respectively.

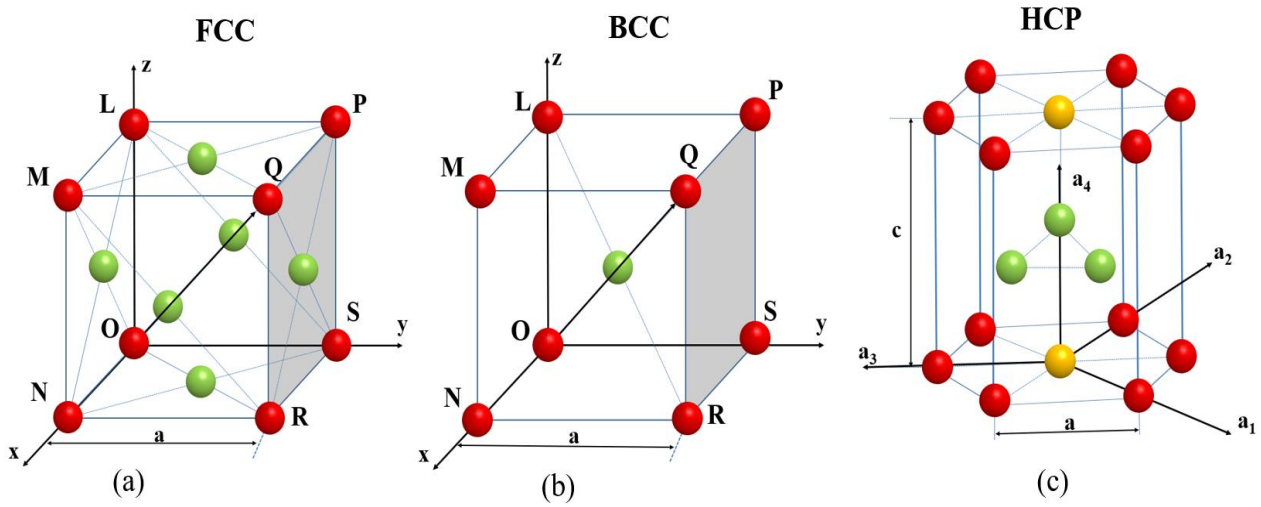

Figure 1.1: Schematic displaying unit cells for (a) face centered cubic (FCC), (b) body centered cubic (BCC) and (c) Hexagonal close packed (HCP) crystals.

1.3 Defects in a single crystal.

The arrangement of atoms in a lattice is not perfectly periodic and there is deviation in this periodicity which results in defect in the crystal. If the deviation is localized to few atoms, the defect is known as *point defect*, whereas if it spreads over a long range then it is called as *lattice imperfection*. Vacancy, interstitial and impurity atom are the point defects commonly observed in a crystal. A vacancy is created when an atom at a lattice point is missing, while interstitial defect is generated when an atom is trapped inside a crystal lattice (refer Figure 1.2). An impurity atom sits at a lattice position leading to the local deviation in the periodicity as shown in Figure 1.2. The defects such as line defects and surface defects are the lattice imperfection in crystals. The dislocations are known as line defects while stacking faults and twined regions are known as

surface defects in single crystals. Grain boundary in polycrystals also falls under the category of surface defects.

1.3.1 Dislocations

As mentioned previously that crystal lattices are not perfect, and they exhibit various types of defects such as point, line and surface defects. In 1934, Taylor and Orowan (Taylor, 1934; Orowan, 1934), independently proposed the idea of the "dislocation" to explain the difference between the theoretical and actual yield strength of metals. The dislocation can be understood as the boundary separating the already slipped and un-slipped region in a material. There are two types of dislocations namely *edge* and *screw* dislocations.

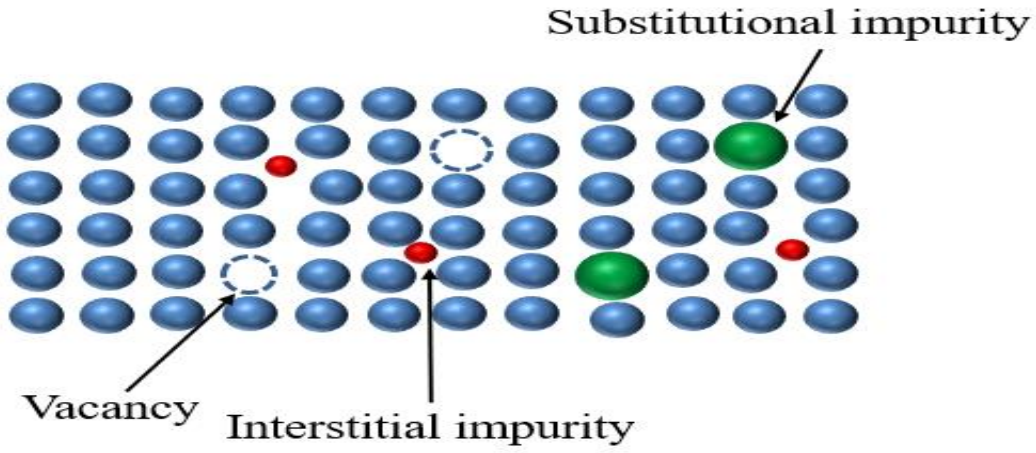

Figure 1.2: Schematic showing point defects in crystal lattice.

An edge dislocation can be visualized as an extra half-plane of atoms inserted in a crystal structure as depicted in Figure 1.3(a). The presence of this extra plane of atom causes distortion in neighboring atoms which reduces rapidly with increasing distance from this extra half plane. The plane on which the dislocation lies is known as *slip plane* and the line extending over the length of dislocation is called *dislocation line* (see Figure 1.3 (a)). An edge dislocation moves perpendicular to dislocation line on a slip plane under the action of shear stress acting perpendicular to its line. This type of motion is known as slip. When an edge dislocation reached to the free surface, it creates a step with length of $\boldsymbol{b}$ which is known as burgers vector (see Figure 1.3 (d)). Further, an edge dislocation can also move perpendicular to the slip plane due to addition

or subtraction of atoms along the dislocation line. This motion of edge dislocation is known as dislocation climb. Note that the dislocation climb is controlled by a diffusion of vacancies and generally found to be operative at elevated temperature.

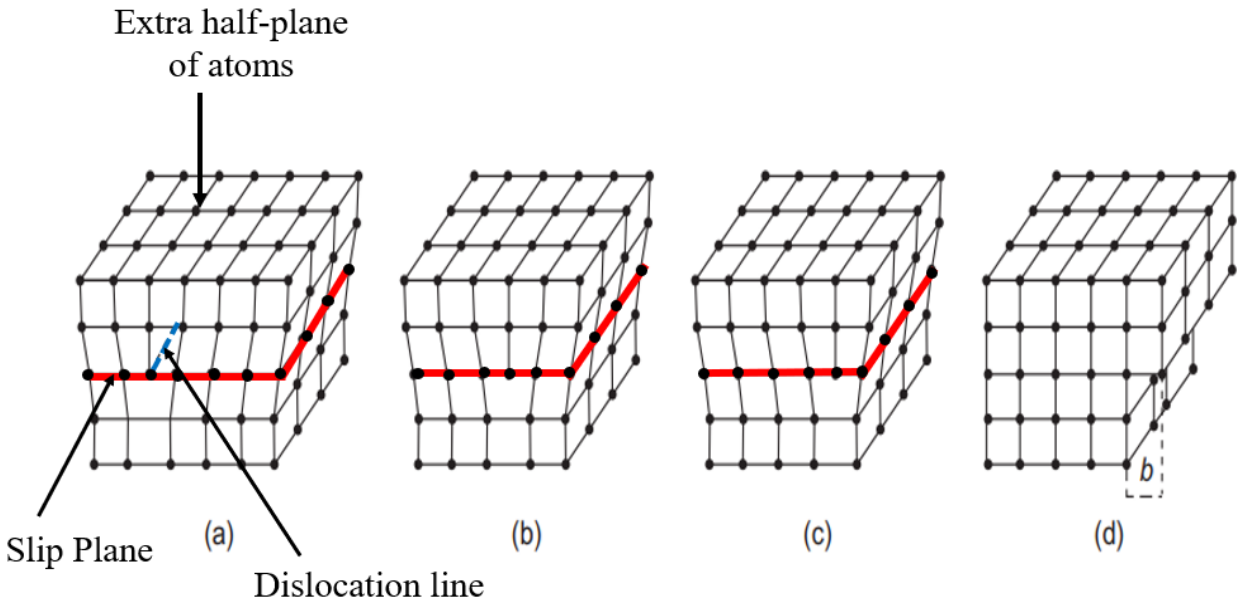

Figure 1.3: Schematic showing (a) an Edge dislocation, (b), (c) and (d) subsequent positions of dislocation as it moves towards the free surfaces (reproduced from Smallman and Ngan, 2014).

A screw dislocation can be imagined by cutting a crystal along a lattice plane and then sliding one half of the crystal over the other by a lattice vector as shown in Figure 1.4. Note that the slip direction of screw dislocation is parallel to the dislocation line. Also, the screw dislocation can cross-slip onto another plane and continue to glide under favorable stress conditions. Screw dislocations, on the other hand, cannot move by process of climb, whereas edge dislocations cannot cross-slip. After the dislocations has completely passed through the crystal, both types of dislocations produce the same final deformation.

In general, pure screw and pure edge dislocations are rarely observed in crystalline materials and the dislocations have been observed experimentally as dislocation loops containing edge and the screw component which is known as mixed dislocation as shown in Figure 1.5. The curved dislocation has both edge and screw character, which vary from point to point along the dislocation line. The region enclosed by the loop can be considered as the “slipped region”.

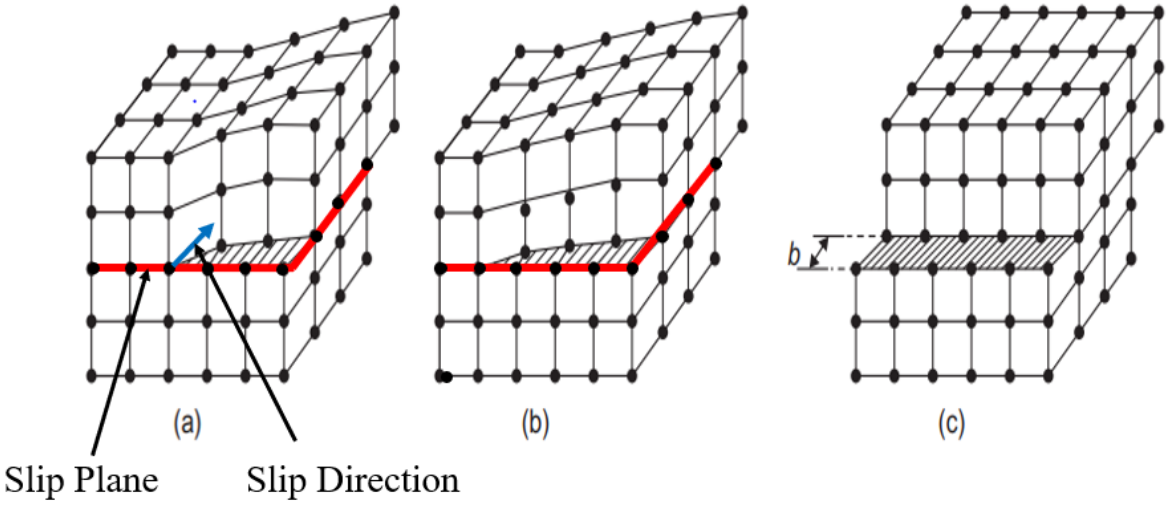

Figure 1.4: Schematic showing a screw dislocation and its motion on a slip plane (taken from Smallman and Ngan, 2014).

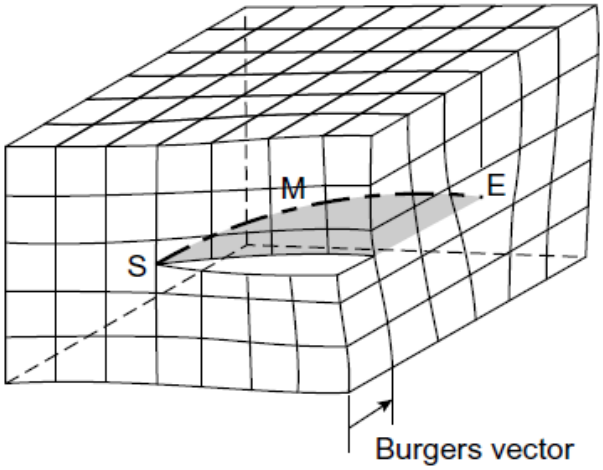

Figure 1.5: Mixed dislocations containing both the edge and the screw component (Hull and Bacon, 2011).

The Burgers vector ***b*** is an important parameter for a dislocation. It is defined by constructing a Burger circuit MNOPQ using a lattice vectors in a crystal containing a dislocation as shown in Figure 1.6 (a). The same sequence of vectors is then created in a defect free crystal as shown in Figure 1.6 (b) and it is observed that circuit does not close. Then the vector QM from finish to start defines the Burger vector for the dislocation. Burgers vector can be used to specify

the displacement of atoms that occurs during the motion of dislocation. For a perfect dislocation it is equal to the shortest lattice translation vector.

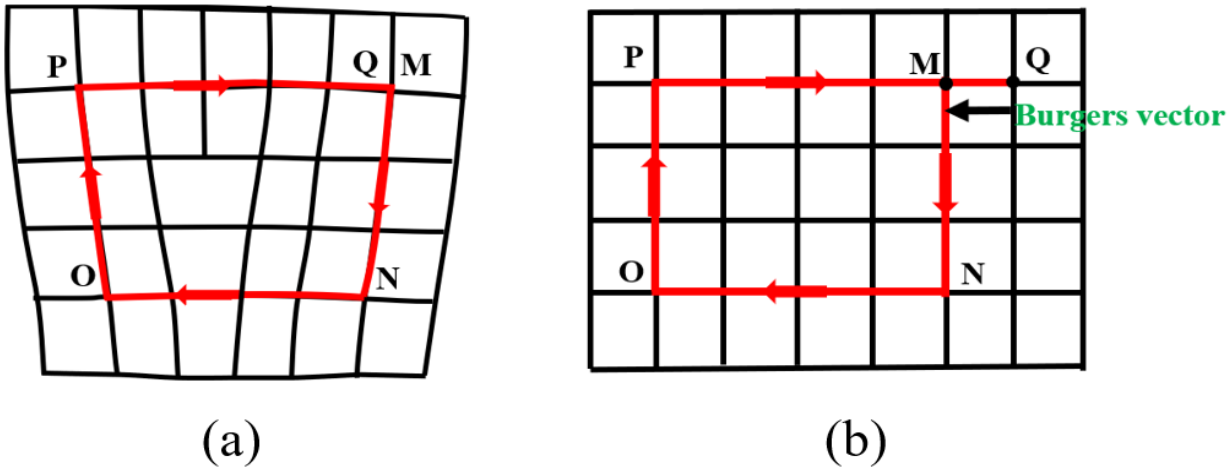

Figure 1.6: (a) Burger circuit created around an edge dislocation in a crystal with dislocation. (b) Failure of Burger circuit in a defect free crystal (reproduced from Hull and Bacon, 2011).

1.4 Fundamental aspects of Body Centered Cubic metals

1.4.1 Slip systems

Slip system are characterized by slip plane normal and slip directions. In BCC metals, there is no plane with predominant atomic density, hence the slip plane is not well defined as opposed to FCC and HCP (Dieter, 1998; Hull and Bacon, 2011). However, the <111> is the close-packed direction and hence slip always occurs along this direction only (Hull and Bacon, 2011). Further, slip in BCC is found to occur in the $\{110\}, \{112\}$ and $\{123\}$ family of planes (Hull and Bacon, 2011) along <111> direction. These slip systems are displayed in Figure 1.7. Furthermore, there are six slip planes of $\{110\}$ type, each having two $< 111 >$ slip directions resulting in 12 systems of $\{110\}$<111> type. In addition, there are twelve $\{112\}$ and twenty four $\{123\}$ types of planes and each having one $< 111 >$ direction leading to 36 slip system. Thus, in total, BCC metals exhibit 48 slip systems (Hull and Bacon, 2011). It is important to notice that three $\{110\}$, three $\{112\}$ and six $\{123\}$ planes intersect along identical <111> direction, therefore dislocations move in

haphazard manner due to enhanced cross slip which leads to the formation of wavy slip lines in BCC metals (Hull and Bacon, 2011). Seeger and Wasserbach (2002) and Seeger (2001; 2004) have reported that it is highly unlikely for slip to occur in {123} plane in pure BCC metal, therefore, the {110}<111> and {112}<111> are accepted to be most predominant in pure BCC metals. They have also demonstrated that the slip planes vary with the temperature. For instance, slip occurs readily on the {110} plane at temperature below 75K which may not be true for higher temperature. It is important to note that deformation twining occurs in {112}<111> system in BCC, hence slip on {112} plane may occur either in twining sense or anti-twining sense which is explained in the next section. In fact, slip is relatively easier when the external stresses are applied in such a way that dislocation moves in twining sense (Hull and Bacon, 2011). The slip plane and normal for slip systems {110}<111> and {112}<111> are listed in the Table. 1.1 and 1.2, respectively.

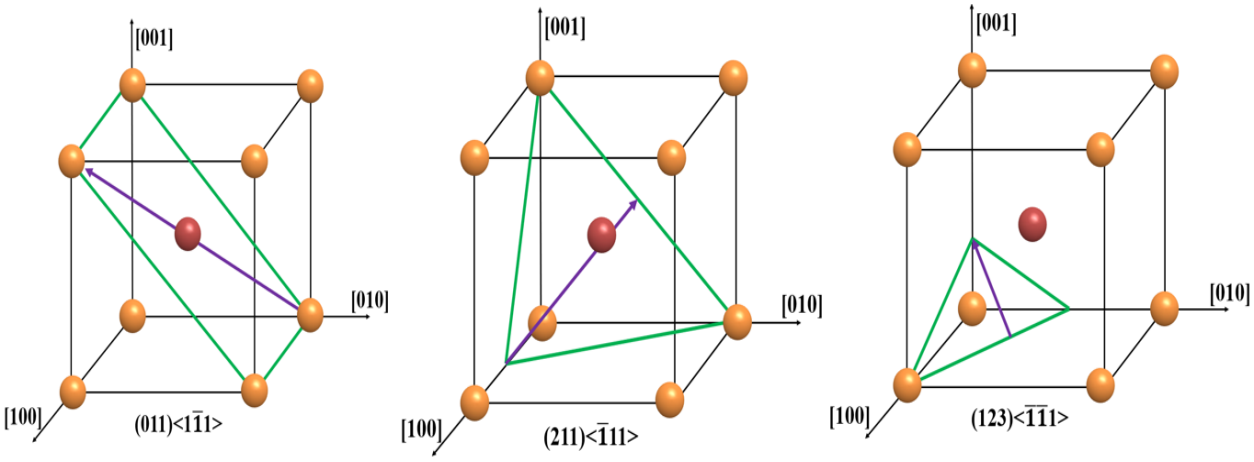

Figure 1.7: Schematic illustrations of different slip systems in BCC metals. The slip direction and slip planes are labelled as violet vectors and green planes, respectively.

1.4.2 Plastic deformation by twinning

Twinning is a mode of deformation in which a region of a crystal undergoes a homogeneous shear that produces the mirror image of an undeformed or un-twinned crystal about the shear plane. In BCC crystals, this type of shear can be produced by a displacement of 1/6<111> on each successive {112} plane. Twinning and anti-twining sense of slip on {112} plane can be understood by analysing the stacking sequence of this plane in BCC crystal, shown in Figure 1.8(a). In this figure, atoms lying in a particular {112} are denoted by identical name. For example, atoms represented

by letter C lie on the same {112} plane. Schematic in Figure 1.8 (b) displays the traces of the $(11\bar{2})$ planes on a (110) plane. Note, atom sites shown by circles lie on (110) plane (i.e., plane of the diagram), while those shown by squares lie a/√2 unit above and below. It can be seen from Figure 1.8 (b) that {112} planes follow the stacking sequence ABCDEFA.

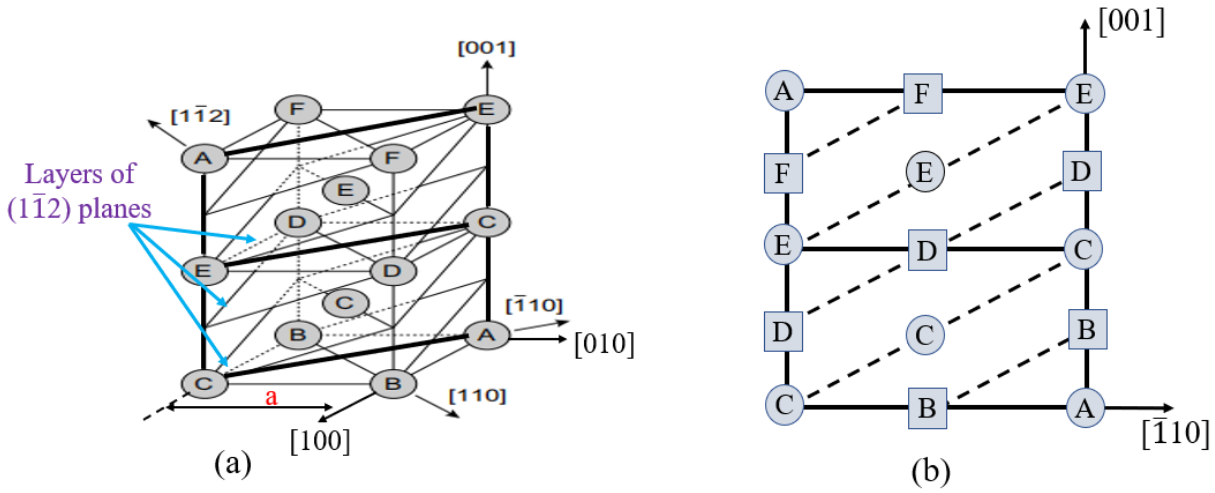

Figure 1.8: (a)The positions of atoms in $(11\bar{2})$ planes in BCC unit cell. (b) Traces of the $(11\bar{2})$ slip planes on a (110) plane.

Figure 1.9(a) shows a $[\bar{1}10]$ oriented BCC single crystal under compressive axial loading. Under $[\bar{1}10]$ compression, the resolved shear stress on the $(1\bar{1}2)$ plane (as marked on a green square stress element) will displace all the atoms in atomic layers E, F and A (lying above layer D) relative to the atomic layer D in the $[\bar{1}11]$ direction by $1/6[\bar{1}11]$ (marked by the black arrow). Consequently, atom 'E' will move to the new site indicated by a red color filled circle, resulting new site being the mirror reflection of the atom C. Similarly, new position of atom F and A will become a mirror image of atom D and E, respectively. The new position of atoms E, F and A are denoted by letters C, D and E, respectively, in Figure 1.9(b). Thus, the new stacking sequence would become as ABCDCDE....(refer Figure 1.9(b)). A second translation on the adjacent plane displaces D to B, E to C, etc., resulting in stacking sequence ABCDCBC..., as shown in Figure 1.9(c). Repeating this translation on successive planes yields stacking sequence ABCDCBA... (refer Figure 1.9(d)), which is the stacking of a twinned crystal about layer D when compared to the initial stacking of ABCDEFA in Figure 1.8(b).

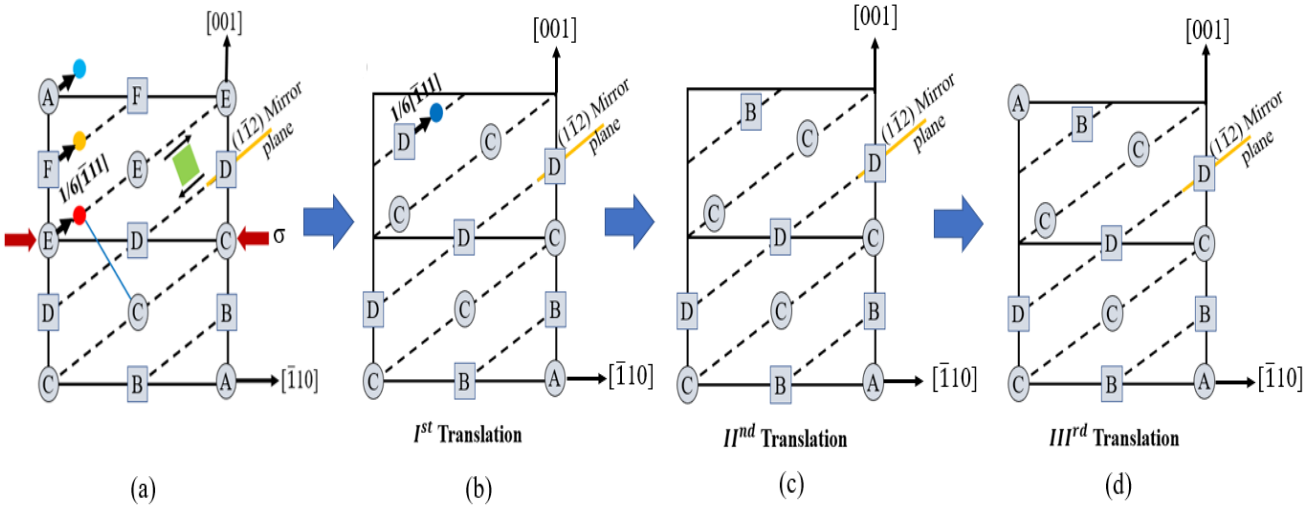

Figure 1.9: Schematic showing crystallographic origin slip in twinning sense in a [$\bar{1}$10] oriented BCC crystal under axial compressive loading.

By contrast, if a tensile load is applied along [$\bar{1}$10] direction, all the atoms in layers E, F and A will be displaced in the opposite direction, (i.e., along [1$\bar{1}\bar{1}$]) by 1/6[1$\bar{1}\bar{1}$] (marked by the black arrow). Thus, the atom E will move to the new site indicated by a blue color filled circle so that it becomes a mirror reflection of the atom D, as shown in Figure 1.10(b). As a result, atoms in layer E will not become the mirror of atoms in layer C, resulting in a stacking of high energy and it is different from the twinned stacking. This type of slip is referred to as slip in anti-twinned sense. Therefore, on {112} planes, there is an asymmetry with respect to 1/6<111> translations in the twinning and anti-twinning sense. Note that in case of anti-twinning, atom in layer E has to displace by 1/3[1$\bar{1}\bar{1}$] so as to become the mirror image of atom in fixed layer C as illustrated in Figure 1.10(c). It can be observed that different amount of shear displacement is required in anti-twinning and twinning to generate mirror symmetry between the displaced atom E and fixed atom C with respect to the mirror twin plane. As a result, shear stress required to move a dislocation in one direction in a slip plane is not the same as the shear stress required to move it in the opposite direction in the same plane.

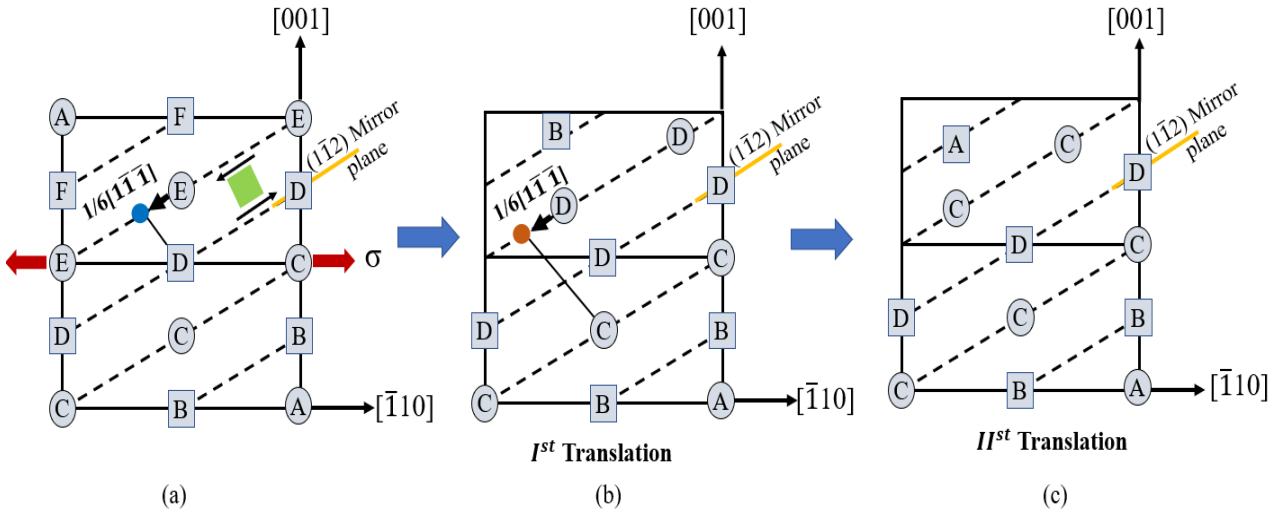

Figure 1.10: Schematic showing crystallographic origin of antitwinning sense in a [$\bar{1}$10] oriented BCC crystal under axial tensile loading.

1.4.3 Plastic deformation by slip

The plastic deformation in a metallic crystal occurs primarily due to the motion of dislocation on a slip plane along slip direction except at low temperature and high strain rate. The slip plane and slip direction together defines a slip system. The resolved shear stress τ^{α} in the slip plane along slip direction is defined as:

$$\tau^{\alpha} = \boldsymbol{\tau}: \left(\boldsymbol{s}^{(\alpha)} \otimes \boldsymbol{m}^{(\alpha)}\right) = \boldsymbol{\tau}: \boldsymbol{\mu}^{\boldsymbol{\alpha}}, \tag{1.1}$$

where, $\boldsymbol{s}^{\boldsymbol{\alpha}}$ and $\boldsymbol{m}^{\boldsymbol{\alpha}}$ are slip direction and slip plane normal, respectively, and $\boldsymbol{\mu}^{\boldsymbol{\alpha}}$ is Schmid tensor for α^{th} slip system. Further, $\boldsymbol{\tau}$ in Eq. (1.1) is the applied stress. For instance, in the case of cylindrical specimen of single crystal with one slip system subjected to an applied tensile force $\boldsymbol{F}$ along the axial direction (refer Figure 1.11), the resolved shear stress is given by:

$$\tau = \frac{F}{A} \cos\phi \,.\, \cos\lambda. \tag{1.2}$$

Where, ϕ and λ are the angles between the slip plane normal and loading axis, and slip direction and loading axis, respectively. In this case, the Schmid tensor degenerates to single component which is commonly referred to as Schmid factor, and it is given by:

$$\mu = \cos\phi \,.\, \cos\lambda. \tag{1.3}$$

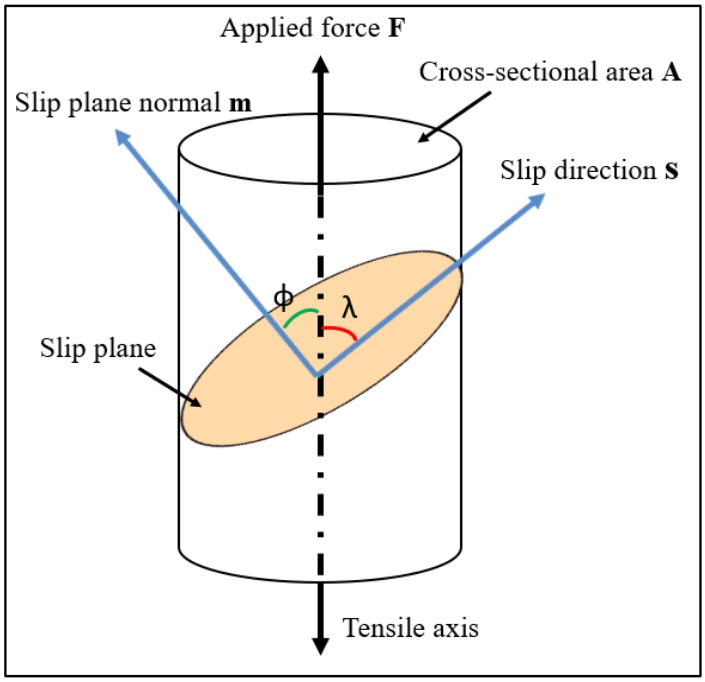

Figure 1.11: Calculation of resolved shear stress parallel to slip direction, from tensile force **F**.

It must be noted that for plastic deformation to occur in FCC and HCP metals, the resolved shear stress should increase beyond a threshold value which is known as critical resolved shear stress (Hosford, 2010). This statement is known as Schmid law. FCC and HCP metals follow the Schmid law, whereas yielding in BCC metals deviates due to twinning-anti-twinning asymmetry and non-planer core of screw dislocation (Vitek, 1976; Woodward and Rao, 2001; Hull and Bacon, 2011). In fact, the dislocation slip in a particular slip system of a BCC crystal is also influenced by stresses other than the resolved shear stresses which is referred to as the non-Schmid behavior. Plastic deformation of pure BCC metals is primarily controlled by the motion of screw dislocations which have high lattice friction stress because of their non-planar cores structure as shown in Figure 1.12. The screw dislocation spread into three {110} planes of the zone having identical slip direction (refer plane m^{α}, n_1^{α} and n_2^{α} in Figure 1.12). The screw dislocations move by the forming double kinks, therefore their motion is dependent on the shear stresses parallel and perpendicular to slip direction. Note that the kinks formed on screw dislocation have edge character. The generalized resolved shear stress used for BCC metals involves a linear combination of six stresses. The first

term (Schmid stress τ^{α}) is complemented by two more shear stresses parallel to the slip direction (s^{α}) but acting in a different planes (called as auxiliary plane) in the zone of the slip direction. If the normal of the auxiliary planes is denoted as n_1^{α} and n_2^{α}, then second and third stress term can be written as ${\tau_1}^{\alpha} = \boldsymbol{\tau}: (\boldsymbol{s^{\alpha}} \otimes \boldsymbol{{n_1}^{\alpha}})$ and ${\tau_2}^{\alpha} = \boldsymbol{\tau}: (\boldsymbol{s^{\alpha}} \otimes \boldsymbol{{n_2}^{\alpha}})$. The three remaining stresses correspond to shear stresses perpendicular to the slip direction. These are ${\tau_3}^{\alpha}$, ${\tau_3}^{\alpha}$and ${\tau_5}^{\alpha}$ which acts on the screw component of dislocation and leads to the movement of screw dislocation.

The generalized resolved shear stress which accounts for the non-Schmid stresses in a BCC metal can be written as (Bassani et al., 2001; Vitek et al., 2004; Gröger et al., 2008):

$$\tau^{e(\alpha)} = \tau^{\alpha} + a_1{\tau_1}^{\alpha} + a_2{\tau_2}^{\alpha} + a_3{\tau_3}^{\alpha} + a_4{\tau_4}^{\alpha} + a_5{\tau_5}^{\alpha}. \tag{1.4}$$

Here, a_{1-5} are material constants and τ_{1-5}^{α} represent the non-Schmid stresses affecting the slip on α^{th} slip system. The non-Schmid stresses, ${\tau_{1-5}}^{\alpha}$ are defined as follows:

$$\begin{aligned}
{\tau_1}^{\alpha} &= \boldsymbol{\tau}: (\boldsymbol{s^{\alpha}} \otimes \boldsymbol{{n_1}^{\alpha}}) = \boldsymbol{\tau}: \boldsymbol{\mu_1^{\alpha}}, \\
{\tau_2}^{\alpha} &= \boldsymbol{\tau}: (\boldsymbol{s^{\alpha}} \otimes \boldsymbol{{n_2}^{\alpha}}) = \boldsymbol{\tau}: \boldsymbol{\mu_2^{\alpha}}, \\
{\tau_3}^{\alpha} &= \boldsymbol{\tau}: ((\boldsymbol{s^{\alpha}} \times \boldsymbol{m^{\alpha}}) \otimes \boldsymbol{m^{\alpha}}) = \boldsymbol{\tau}: \boldsymbol{\mu_3^{\alpha}}, \\
{\tau_4}^{\alpha} &= \boldsymbol{\tau}: \left((\boldsymbol{{n_1}^{\alpha}} \times \boldsymbol{s^{\alpha}}) \otimes \boldsymbol{{n_1}^{\alpha}}\right) = \boldsymbol{\tau}: \boldsymbol{\mu_4^{\alpha}}, \\
{\tau_5}^{\alpha} &= \boldsymbol{\tau}: (\boldsymbol{{n_2}^{\alpha}} \times \boldsymbol{s^{\alpha}}) \otimes \boldsymbol{{n_2}^{\alpha}}) = \boldsymbol{\tau}: \boldsymbol{\mu_5^{\alpha}}.
\end{aligned} \tag{1.5}$$

Here, $\boldsymbol{n_1^{\alpha}}$ and $\boldsymbol{n_2^{\alpha}}$ are normal vectors to the non-glide planes for α^{th} slip system. The normal vectors, $\boldsymbol{{n_1}^{(\alpha)}}$ and $\boldsymbol{{n_2}^{(\alpha)}}$ are listed in Table 1.1 for systems involving slip on {110} planes. In a BCC metal, the plastic yielding is assumed to occur when the generalized resolved shear stress, $\tau^{*(\alpha)}$ increases beyond a threshold value. The slip on {112}<111> system can be understood as a result of dislocations motion by elementary steps on the two highly stressed {110} planes of the same $< 111 >$ zone. These pairs of $\{110\} < 111 >$ slip systems are denoted by α_1 and α_2 for each {112}<111> system and listed in Table 1.2. The above-mentioned mechanism can be understood from the schematic Figure 1.13. In this figure, planes (211), (110) and (101) are displayed. Note that a same amount of displacement in plane (211) can be achieved through vector sum of two elementary displacement in (110) and (101) planes. In this manner, the motion of screw dislocations (211) plane can be understood as the result of its elementary motion on (110) and (101) plane. When the slip trace reaches to the surface of the sample, it gives the impression that

it was produced by the motion of dislocation on (211) plane, but it was produced by the elementary steps (110) and (101) which are not observable experimentally. Thus, a {112} slip trace on the surface of a crystal is a result of slip on two {110} planes.

Table 1.1: The vectors $\boldsymbol{m^{\alpha}}$, $\boldsymbol{s^{\alpha}}$, $\boldsymbol{n_1}$ and $\boldsymbol{n_2}$ for {110}<111> slip systems in a BCC crystals (reproduced from Daphalapurkar et al. (2018)).

α	$\boldsymbol{s^{\alpha}}$	$\boldsymbol{m^{\alpha}}$	$\boldsymbol{n_1}$	$\boldsymbol{n_2}$
1	111	$01\bar{1}$	$\bar{1}10$	$10\bar{1}$
2	111	$\bar{1}01$	$0\bar{1}1$	$\bar{1}10$
3	111	$1\bar{1}0$	$10\bar{1}$	$0\bar{1}1$
4	$\bar{1}11$	$\bar{1}0\bar{1}$	$\bar{1}\bar{1}0$	$01\bar{1}$
5	$\bar{1}11$	$0\bar{1}1$	101	$\bar{1}\bar{1}0$
6	$\bar{1}11$	110	$01\bar{1}$	101
7	$\bar{1}\bar{1}1$	$0\bar{1}\bar{1}$	$1\bar{1}0$	$\bar{1}0\bar{1}$
8	$\bar{1}\bar{1}1$	101	011	$1\bar{1}0$
9	$\bar{1}\bar{1}1$	$\bar{1}10$	$\bar{1}0\bar{1}$	011
10	$1\bar{1}1$	$10\bar{1}$	110	$0\bar{1}\bar{1}$
11	$1\bar{1}1$	011	$\bar{1}01$	110
12	$1\bar{1}1$	$\bar{1}\bar{1}0$	$0\bar{1}\bar{1}$	$\bar{1}01$

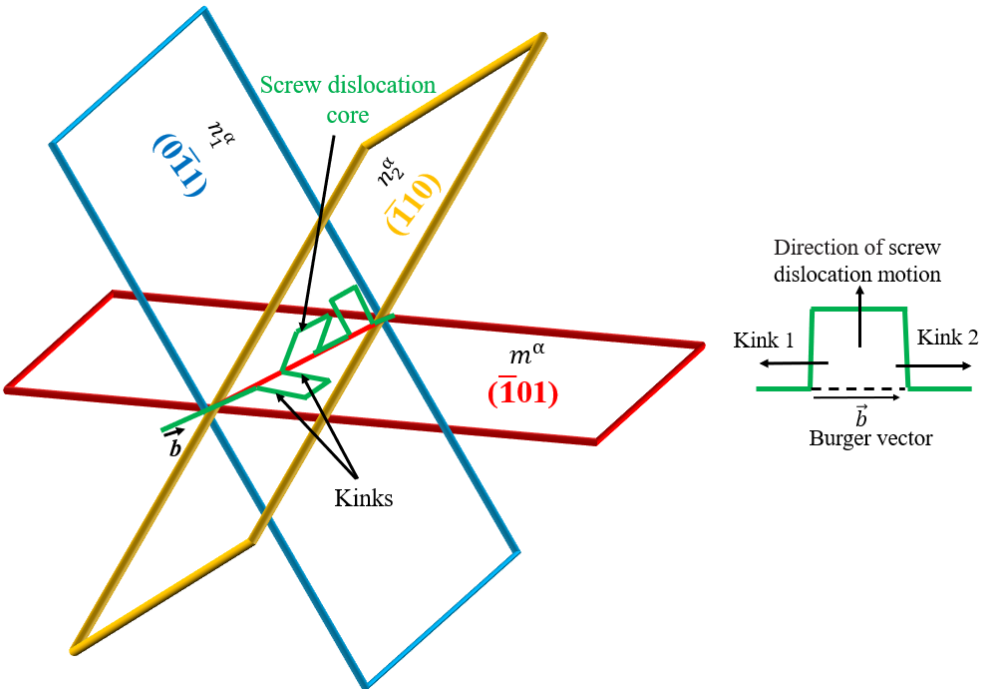

Figure 1.12: Schematic showing core of screw dislocation spread into three {110} planes having common slip direction <111>.

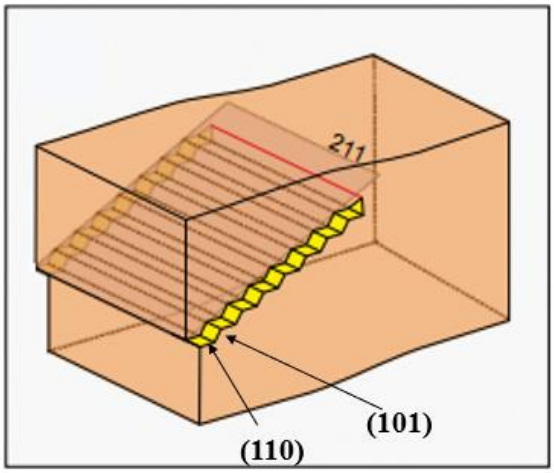

Figure 1.13: Schematic presentation of elementary slip steps on (110) and (101) in equal portions (taken from Marichal et al., 2013).

Table 1.2: The vectors $\boldsymbol{m^{\alpha}}$ and $\boldsymbol{s^{\alpha}}$ for {112}<111> slip systems and the conjugate pair α_1 and α_2 of {110}<111> systems (reproduced from Daphalapurkar et al. (2018)).

α	$s^{(\alpha)}$	$m^{(\alpha)}$	α_1	α_2
13	111	$11\bar{2}$	1	2
14	111	$\bar{2}11$	2	3
15	111	$1\bar{2}1$	3	1
16	$\bar{1}11$	$\bar{1}1\bar{2}$	4	5
17	$\bar{1}11$	$\bar{1}\bar{2}1$	5	6
18	$\bar{1}11$	211	6	4
19	$\bar{1}\bar{1}1$	$\bar{1}\bar{1}\bar{2}$	7	8
20	$\bar{1}\bar{1}1$	$2\bar{1}1$	8	9
21	$\bar{1}\bar{1}1$	$\bar{1}21$	9	7
22	$1\bar{1}1$	$1\bar{1}\bar{2}$	10	11
23	$1\bar{1}1$	121	11	12
24	$1\bar{1}1$	$\bar{2}\bar{1}1$	12	10

1.4.4 Crystal plasticity models for BCC metals

Several constitutive theories have been proposed to characterize the deformation behavior of BCC crystals, which are summarized in the following. Liao et al. (1998) developed a crystal plasticity model for BCC metals by adopting the general framework given by Asaro and Rice (1977) and Asaro and Needleman (1985), and using the power law relation between shear strain rate and resolved shear stress proposed by Pan and Rice (1983). They incorporated 24 slip system by considering the slip in {110}<111> and {112}<111> slip systems. By using this constitutive model, they studied the cold-rolling process of low-carbon steel sheets. Lee et al. (1999) also employed the power-law form of expression of shear strain rate given by Hutchinson, (1976) and

Peirce et al. (1983). The power law forms of the expression for shear strain used in models of Liao et al (1998) and Lee et al. (1999) can capture the viscoplastic response of BCC crystals only in a very narrow range of temperature and strain rate. Therefore, these models cannot capture the dependence of critical resolved shear stress on the strain rate and temperature under dynamic loading conditions at low homologues temperatures. Kothari and Anand (1998) used a flow rule based on thermally activated theory for plastic flow given by Kocks et al. (1975) and Frost and Ashby (1982), and successfully predicted the deformation response of Tantalum crystals at temperature -200 to 525^{o}C and for strain rates of 1×10^{-4} to $3 \times 10^{4}\ s^{-1}$. Xie et al. (2004) and Ganapathysubramanian and Zabaras (2005) also use similar flow rule and modelled the cyclic deformation behaviour of high strength low alloy steel. It must be mentioned that the models of Kothari and Anand (1998), Xie et al. (2004) and Ganapathysubramanian and Zabaras (2005) do not consider tension-compression asymmetry and the orientation dependence of critical resolved shear stress caused by non-Schmid behaviors of BCC. Daphalapurkar et al. (2018) proposed a crystal plasticity model by adopting the flow rule of Kothari and Anand (1998) and considering the effect of non-Schmid stresses as well. They successfully predicted the effect of strain rate, ambient temperature and crystal orientation on the stress-strain response of Mo single crystals.

1.5 Instrumented Indentation Experiments

Instrumented indentation test (IIT) is an advance indentation technique in which *in-situ* characterization of the mechanical properties of a small volume of material can be performed. Also, the indentation load, P and indentation depth, h, are continuously recorded throughout the experiments. Oliver and Pharr (1992) proposed a methodology to determine the elastic modulus, E and hardness, H of material using the $P-h$ curve which is commonly referred to as Oliver-Pharr (O-P) method. To this end, the contact stiffness, S, projected area of indenter, A_c and the reduced modulus E_r need to be determined. The key equations required for these calculations are taken from the work of Oliver and Pharr (1992) and are summaries below. The contact stiffness, S, defined as the initial slope of the unloading portion of $P-h$ curve, is determined by fitting the following power law to the unloading part of $P-h$ curve, refer Figure 1.14 (Oliver and Pharr, 1992):

$$P = C(h - h_f)^m \tag{1.6}$$

In above equation, h_f is residual depth after unloading, while C and m are the fitting constants. The value of m = 1 for flat punch/indenter, while $m = 1.2 - 02$ for Berkovich indenter (Oliver and Pharr, 1992). The contact stiffness is determined as (Oliver and Pharr, 1992):

$$S = \frac{dP}{dh} = Cm\big(h - h_f\big)^{m-1}\Big|_{h=h_{max}} \tag{1.7}$$

For Berkovich indenter with half tip angle θ ~ 65.3°, A_c is given by (Oliver and Pharr, 1992):

$$A_c = f(h_c) = 3\sqrt{3}\, h_c^2\, tan^2\,\theta \approx 24.5 h_c^2, \tag{1.8}$$

Where, h_c is the contact depth as shown in Figure 1.15. Also note that most of the strain-hardening materials exhibit pile-up of plastically deforming material around the indenter, while strain softening materials show sink-in effect during the indentation. The limitation of the O-P method is that it does not account the pile-up effects, but the depth, h_c can be estimated after eliminating the sink-in effect using the following equations (Oliver and Pharr, 1992):

$$h_c = h_{max} - \frac{\varepsilon P_{max}}{S} \tag{1.9}$$

Here, h_{max} is maximum indentation depth, ε is a constant that depends on the indenter geometry which is taken to be 0.75 for the pyramidal Berkovich indenter. Once A_c is determined, the hardness can be determined as (Oliver and Pharr, 1992):

$$H = \frac{P_{max}}{A_c}, \tag{1.10}$$

where, P_{max} is the maximum applied load. The reduced modulus can be determined by (Oliver and Pharr, 1992):

$$E_r = \frac{\sqrt{\pi} S}{2\beta\sqrt{A_c}}. \tag{1.11}$$

Here, the constant β depends upon the indenter geometry and for Berkovich indenter it is usually taken as 1.034. Having E_r known, the elastic modulus can be determined using the following expression (Oliver and Pharr, 1992):

$$\frac{1}{E_r} = \frac{(1 - v^2)}{E} + \frac{(1 - v_i^2)}{E_i}. \tag{1.12}$$

Here E and v are elasticity modulus and Poisson ratio of the specimen, respectively, while E_i and v_i are the corresponding elastic constants of indenter.

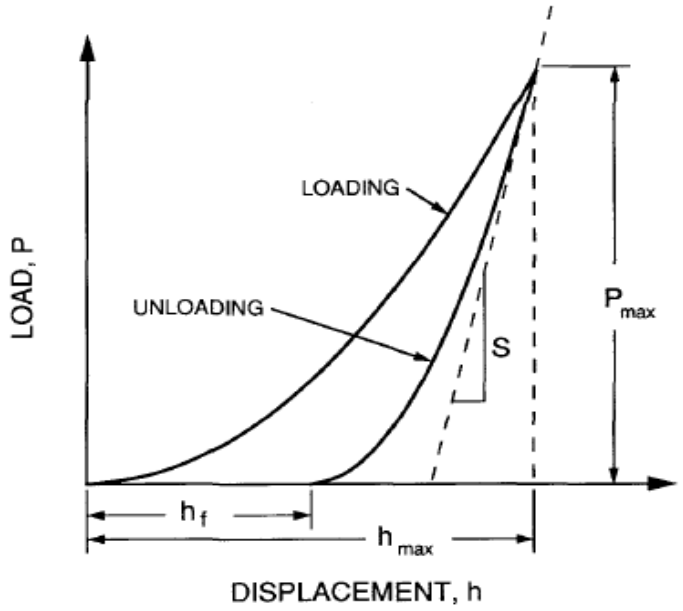

Figure 1.14: Schematic showing the typical indentation load, P versus indentation depth, h curve obtained from an instrumented indentation experiment (reproduced from Oliver and Pharr, 1992).

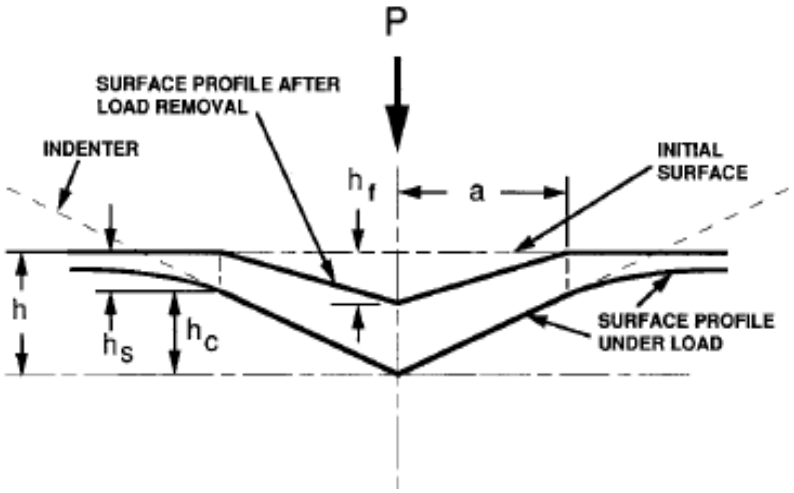

Figure 1.15: Schematic displaying of the surface profiles at maximum indentation load and after the complete unloading along with the important geometrical lengths used in the Oliver–Pharr analysis (reproduced from Oliver and Pharr, 1992).

By contrast to the conventional indentation experiments, the onset of plastic deformation during loading can be identified by noting the displacement burst or pop-in events. The pop-in are noticed when the instrumented-indentation test are performed under load-controlled mode as shown in Figure 1.16. Experiments have confirmed that the pop-in events are the consequence of nucleation of dislocations underneath the indenter (Alcalá et al., 2012; Zhang and Ohmura, 2014). These pop-in events occur when the resolved shear stress at a point below the indenter approaches to the theoretical shear strength of the material (Biener et al., 2007). The maximum resolved shear stress τ_{max} below the indenter given by the Hertzian contact theory for isotropic elastic solids gives is (Morris et al., 2011):

$$\tau_{max} = 0.31\left(\frac{6}{\pi^3}\frac{PE_r^2}{R^2}\right)^{\frac{1}{3}}, \qquad P = \frac{4}{3}E_r\sqrt{R}\,h^{\frac{3}{2}} \tag{1.13}$$

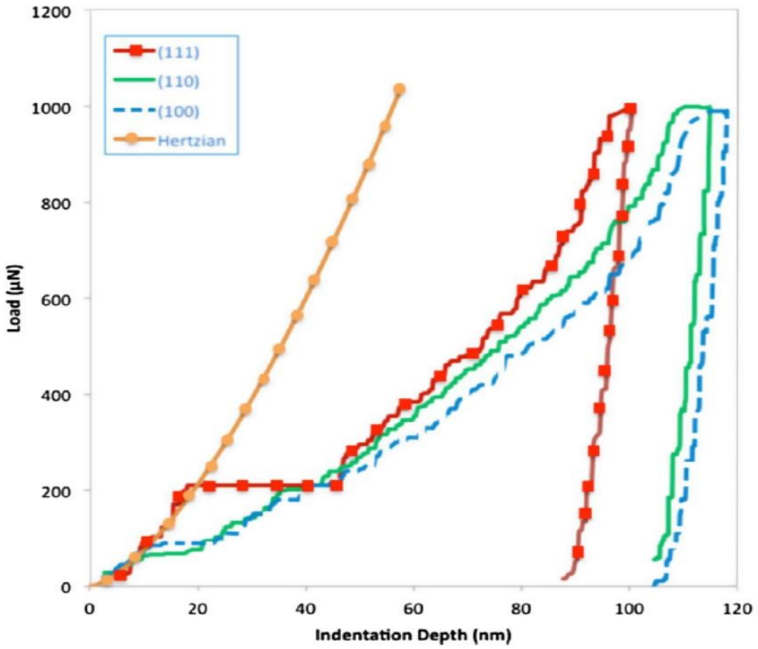

Figure 1.16: Indentation load versus indentation depth curves for (100), (110) and (111) oriented Tantalum single crystal obtained from nanoindentation experiments by Remington et al. (2014). The elastic Hertzian solution is also plotted. Note that elastic solutions deviate from the experimental data when pop-in occurs.

where, R is the indenter-tip radius. Note that Eq. (1.13) is valid for very small values of indentation depth up to which elastic solutions are application. The Eqs. (1.13) are used to predict the first pop-in event caused primarily by dislocation nucleation in ductile metals.

1.6 Indentation response of BCC metals:

Stelmashenko et al. (1993) performed microhardness experiments on Tungsten (W) single crystals oriented along (100), (110) and (111) using Vickers indenter. They observed significant indentation size effect from indentation along all three orientations (see Figure 1.17). Further, they reported maximum hardness along (100) direction and lowest along (111) direction. In addition, hardness values of (100) oriented crystal was strongly depend on the azimuthal orientation of indenter, while this was not the case for (111) oriented crystal. Yao et al. (2014) have also investigated the effect of the orientation on the indentation response of W single crystals through spherical micro-indentation and complementary finite element simulations employing Peirce–Asaro–Needleman crystal plasticity model (Peirce et al., 1983). They reported that the crystal orientation has marginal effect on indentation load-displacement curves, whereas it affects considerably the pile-up patterns on the indented surfaces. For instance, they reported pileup patterns to exhibit four-, two- and three-fold symmetry for indentation on the (100), (110) and (111) surfaces, respectively (see Figure 1.18).

The four-, two- and three-fold symmetry on pile-up patterns has also been reported on (001)-, (110)-, (111)-oriented Tantalum (Ta) single crystals from spherical nano-indentation performed by Biener et al. (2007). In addition, Biener et al. (2007) noticed a single pop-in event on load-displacement curve corresponding to (001)-oriented crystal which they correlated with rapid nucleation of dislocations. Yao and You (2017) have reported from Vickers indentation that the crystal orientation and azimuthal orientation of indenter have significant effect on the pile-up patterns on Ta single crystals. Remington et al. (2014) performed Berkovich nanoindentation experiments on (100), (110) and (111) oriented Ta single crystals. They noticed pop-in events occurring at lower load in the case of indentation on (100) and (110) surfaces than that for (111) case. Thus, they reported highest hardness for (111)-oriented crystal and almost equal hardness for (100)- and (110)-oriented crystals.

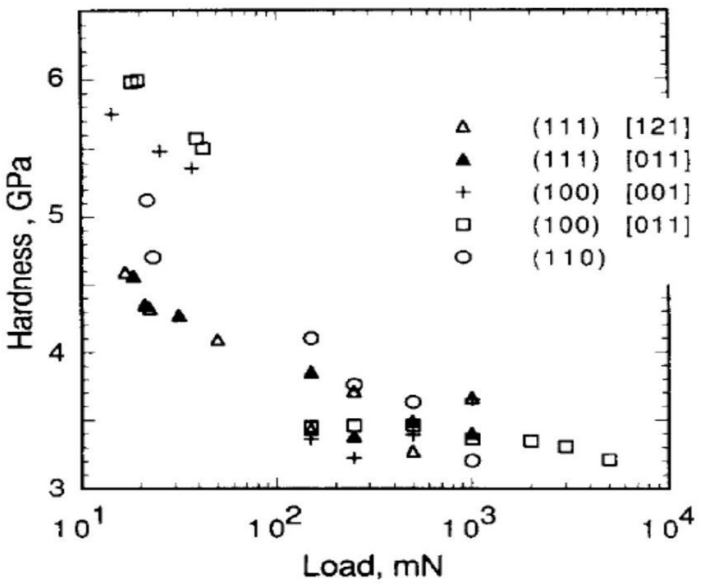

Figure 1.17: Variation of hardness with indentation load for Tungsten single crystals (reproduced from Stelmashenko et al., 1993). Note: When indentation is performed on (111) surface for two in-plane orientation, the first with one of the sides parallel to the [121] direction and the second with one side parallel to [011] direction. Similarly, when the indentation is performed on the (100) surface one of indenter's diagonal is along [001] direction and during second time diagonal is along [011] direction by changing the in-plane orientation of indenter.

Smith et al. (2003) performed nanoindentation experiments as well as complementary molecular dynamics simulations on Fe single crystals to understand the effect of the crystal orientation on their indentation behaviour. The (110) oriented Fe crystal showed two-fold symmetry in pileup pattern when indented with the sphero-conical indenter, while on the indentation with pyramidal indenter, the pileup patterns were asymmetric though exhibited three-fold rotational symmetry with respect to azimuthal orientation of the indenter. Further, pileup pattern on the (100)-oriented crystal showed four-fold symmetry, whereas (111)-oriented crystal were almost similar irrespective of azimuthal orientation of the indenter. Further, Smith et al. (2003) found (100) surface is harder than (110) and reported significant ISE in (100)- and (110)-oriented Fe crystals, though it was more pronounced in the case of latter. Čech et al. (2018) investigated the indentation response of Fe_3Si single crystals by performing the spherical nanoindentation experiments along two orientations (110) and (100). Their results showed that the hardness and indentation modulus for (110) oriented crystal are higher than that for (100) oriented

crystal. Also, they reported four-fold symmetry in the pileup patterns produced on (100) surface, but two-fold symmetry on (110) surface. Further, they noticed rounded-square shaped indent in the former, and almost circular indent in the case of latter. Furthermore, they showed from FE simulations, that the resolved shear stress was maximum for {112}<111> slip system, lowest for {110}<111> slip system and intermediate for {123}<111> slip system, irrespective of orientation of the crystal. The number of slip systems with maximum resolved shear stress for (100) orientation was twice of that for (110) orientation.

Demiral et al. (2013) investigated the deformation behavior of BCC β-titanium alloy Ti-15-3-3-3 single crystals for two orientations, (0.641 0.078 0.764) and (0.114 0.107 0.988) by performing nanoindentation experimentation and finite element simulation using strain-gradient crystal plasticity model. The crystallographic orientation had marginal effect on the indentation load-depth curve but significant effect on the pile-up patterns on the indented surfaces. The pileup

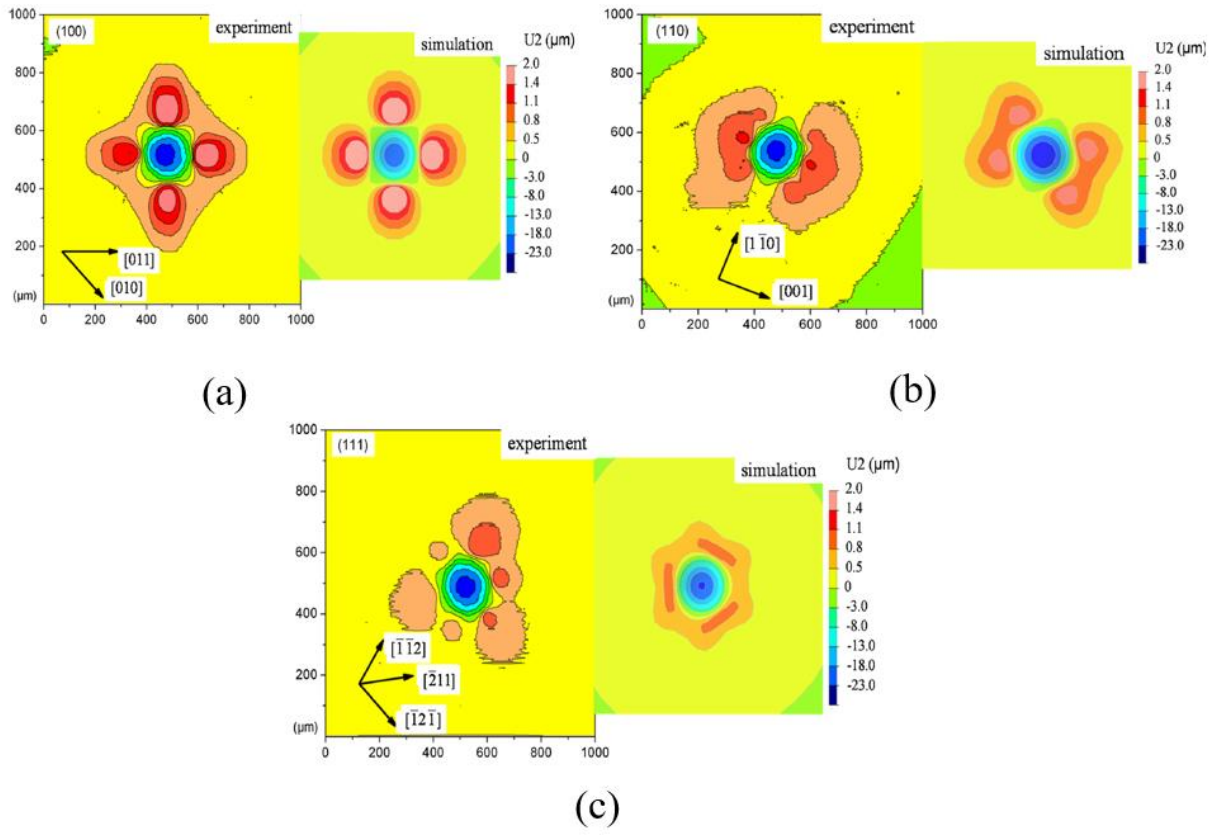

Figure 1.18: The pile-up patterns on (a) (100)-oriented, (b) (110)-oriented and (c) (111)-oriented Tungsten single crystal (reproduced from Yao et al., 2014).

patterns on the (0.641 0.078 0.764) and (0.114 0.107 0.988) surfaces exhibited two- and four-fold symmetry respectively.

Wang et al. (2005) performed Berkovich nanoindentation experiments on nanocrystalline Tantalum. They reported that deformation mechanism is governed by deformation twinning and not by slip as reported in the single crystals. Zhao et al. (2014) investigated the effects of strain rate on the hardness of nanocrystalline Mo thin film through nanoindentation experiments. They reported inverse ISE and significant sensitivity of hardness to the depth dependent strain rate. The highest value of strain rate sensitivity parameter was 0.22 for lowest indentation depth which drops rapidly with increase in indentation depth. Similarly, Hu et al. (2017) also investigated the effect of strain rate on deformation behavior of coarse grain as well as nano-crystalline Tantalum through nanoindentation experimentation. They reported that nanocrystalline Tantalum is harder than the coarse grain Ta. Also, the effect of strain rate was more pronounced on the nanograin Ta in comparison to the coarse grain Ta.

1.7 Issues for investigation

The experimental and numerical studies discussed in the previous section show that the hardness of Ta, W, BCC Fe and Ti alloys depends on the crystallographic orientation of these crystals. Further, the pile-up patterns are also influenced by the both the crystal orientation as well as the azimuthal orientation of the indenter. It must be noticed that most of the indentation studies are performed on Ta, W, BCC Fe and Ti alloys, and very little work has been devoted to the Mo crystals, hence the understanding of the indentation behaviour of Mo crystals is far from the complete. In the view of the indentation behaviours of the Ta, W, BCC Fe and Ti alloys, the following questions pertaining to Mo single crystals arises:

1) Does the hardness and Elastic modulus of Mo single crystals change with the orientation of molybdenum single crystal?
2) Do the Mo single crystal exhibit indentation size effect as observed in the case of W single crystal reported by Stelmashenko et al. (1993). Is the indentation size effect in Mo crystal orientation dependent?
3) How does the orientation of Mo single crystal affect the pile-up pattern?

4) How does the plastic zone size below the indenter change with change in the crystal orientation?

1.8 Objectives:

The following objectives are defined based on the issues for investigation listed in the previous section:

1) To perform micro- as well as nano-indentation experiments at different loads on (100), (110) and (111) oriented Molybdenum single crystals.
2) To compute the hardness at different loads and investigate if Mo crystal exhibit indentation size effect.
3) To determine the predominant slip system beneath the indenter for indentation along different orientation.
4) To implement a crystal plasticity model for BCC single crystal by writing user-defined element subroutine (UEL) in commercially available software ABAQUS (Dassault Systèmes, 2017).
5) To benchmark the developed UEL against the experimental results available in the literature.

1.9 Organization of the Thesis

The remaining chapters of this thesis are organized as follows:

In Chapter 2, the sample preparation, and the methodologies for micro- and nano-indentation experiments on (100)-, (110)- and (111)-oriented Mo single crystals are described. The important results from the experiments are also discussed.

In Chapter 3, the Crystal Plasticity constitutive model (Daphalapurkar et al., 2018) and its numerical implementation in commercially available software Abaqus 6.17 (Dassault Systèmes, 2017) are discussed. In addition, the methodology to optimize the material parameters appearing in the model is also discussed.

In Chapter 4, the important conclusions drawn from the chapters 2 and 3 are summarized and the possible further works are also discussed.

Chapter 2

Experimental investigation of the indentation response of molybdenum single crystals

2.1 Introduction

Molybdenum (Mo), a body-centered cubic (BCC) metal, has been found to be a potential candidate for various applications including semiconductor, defense, and medical industries, owing to their high yield and compressive strength, superior fracture strength, very high melting point, good thermal conductivity, and exceptional corrosion resistance (MaTecK Germany; Lunk and Hartl, 2017). Experimental and numerical studies performed on other BCC single crystals show that the hardness and pile-up patterns depend on their crystallographic orientation. It must be mentioned that most of the studies are performed on Ta, W, BCC Fe and Ti alloys, and little attention has been given to the Mo crystals. Therefore, nano- and micro-indentation experiments on Mo single crystals oriented along (100), (110) and (111) are performed to understand their indentation response, in this Chapter. The outline of this chapter is as follows: In Section 2.2, the experimental methodology of nano- and micro-indentation are discussed, while the important results and discussion are presented in Section 2.3. Finally, work done in this chapter is summarized in Section 2.4.

2.2 Experimental methodology of nano- and micro-indentation

Single crystalline (100), (110), and (111) oriented Mo crystals (having 4N purity) with a diameter of 10 mm and thickness of around 1 mm, are procured from MaTecK, Germany. The single crystals are manufactured using floating zone melting technique (Wenzl and Schlich, 2006) and their orientations are verified using X-ray diffraction method. The sample surfaces are then mechanically polished using a series of increasing grit emery papers followed by polishing with a diamond paste to a surface finish of ~ 0.25 μm. Enough care was exercised to prevent the mechanical damage to the sample surface due to mechanical polishing. The quasi-static nanoindentation experiments were performed at room temperature using a (Hystrion Bruker Ti

Premier) nanoindenter fitted with a Berkovich diamond indenter (a three-sided pyramid) to obtain the nanomechanical properties. As the nanoindentation results are sensitive to indenter tip geometry and the machine compliance, the indenter tip area function is calibrated using standard quartz sample. All the nanoindentation experiments are performed in the load-controlled mode in the load range of 2 to 9 mN. A trapezoidal shape loading profile is used with a 10 s time for loading and unloading and a 5 s dwell time at the peak load. A minimum of 15 indentations are performed for each indentation load and the average hardness values are reported. The spacing between the successive indents was taken at least 10-15 times the maximum penetration depth to prevent the strain field interaction. The Oliver-Pharr method was employed to determine the nanoindentation hardness, H_n, and elastic modulus, E of the material (Oliver and Pharr, 1992; Pharr and Bolshakov, 2002).

$$Hardness,\ H = \frac{P_{max}}{A_c} \tag{2.1}$$

$$Elastic\ modulus\ of\ the\ specimen,\ E_s = (1 - \nu_s^2)/\left[\left(\frac{2\beta\sqrt{A_c}}{S\sqrt{\pi}}\right) - \left(\frac{(1-\nu_i^2)}{E_i}\right)\right] \tag{2.2}$$

Here, P_{max} denotes the maximum indentation load, β is a constant (for Berkovich indenter β = 1.034), A_c is the contact surface area, and S is the slope obtained from the initial portion of the unloading curve. Likewise, E_s, ν_s, E_i, and ν_i are elastic moduli and Poisson's ratio with subscript *s* and *i* indicating the specimen and indenter, respectively. The Poisson's ratio ν_s for Mo was taken as 0.3 while the E_i, and ν_i of the indenter are taken as 1141 GPa and 0.07, respectively (Simmons and Wang, 1971).

To further understand the variation of hardness on the indentation load (or indentation size) micro-Vickers indentation experiments are performed in the load range of 50 to 5000 mN. Microhardness, H_m, values are determined as the ratio of indentation load to the projected area of the impression. As the representative strain values of Berkovich and Vickers indenters are nearly the same, the indentation hardness, H obtained from the experiments are plotted together to understand the effect of P on the H. The indentation depth, h was calculated from the indentation size, d using equation (2.3),

$$h = d/2\sqrt{2}\tan\left(\frac{\psi}{2}\right) \tag{2.3}$$

where ψ is the angle between opposite faces of the indenter (for Vickers indenter ψ = 136°).

2.3 Results and discussion

2.3.1 Nanoindentation study

2.3.1.1 Indentation load, *P* vs. penetration depth, *h* curves

The *P* vs. *h* curves (100), (110) and (111) Mo single crystals are shown in Figure 2.1(a)–(c) respectively. According to the Oliver-Pharr analysis, the loading and unloading curves are approximated by the power-law function of the form:

$$P = \alpha h^m \tag{2.4}$$

$$P = \beta(h - h_f)^n \tag{2.5}$$

where *P* is the indentation load for a corresponding penetration depth *h* and h_f is the final penetration depth after complete unloading; α, β, *m*, and *n* are empirically determined fitting constants. The loading and unloading parts of all *P* vs. *h* curves are in good agreement with equations (2.4) and (2.5). The unloading power-law exponent, *n*, is in the range of 1.45-1.75 (with a regression coefficient, R ~ 0.999) (Oliver and Pharr, 1992, 2004; Pharr and Bolshakov, 2002; Voyiadjis et al., 2010). The variation of maximum penetration depth, h_{max}, is plotted against the maximum indentation load, P_{max} in Figure 2.2 and it indicates the following trend: $h_{max}^{(110)} < h_{max}^{(111)} < h_{max}^{(100)}$ suggesting that (110) orientation offers the highest resistance to plastic deformation.

The ratio of penetration depth recovered during unloading to maximum penetration depth is the simplest quantitative measure of elastic deformation (Stelmashenko et al., 1993). The h_{max} and h_f are determined from the *P* vs. *h* curves and the ratio $(h_{max} - h_f)/h_{max}$ in percentage is presented in Figure 2.2. From these values it can be inferred that the amount of elastic recovery is least for (110) and maximum for (100) oriented crystals while intermittent on the (111) oriented crystal, indicating that the (100) orientation has the least elastic modulus and (110) has the highest modulus. The values of the elastic modulus obtained from nanoindentation experiments for (100), (110), and (111) Mo single crystals are 235 ± 12, 275 ± 15 and 210 ± 10 GPa, respectively.

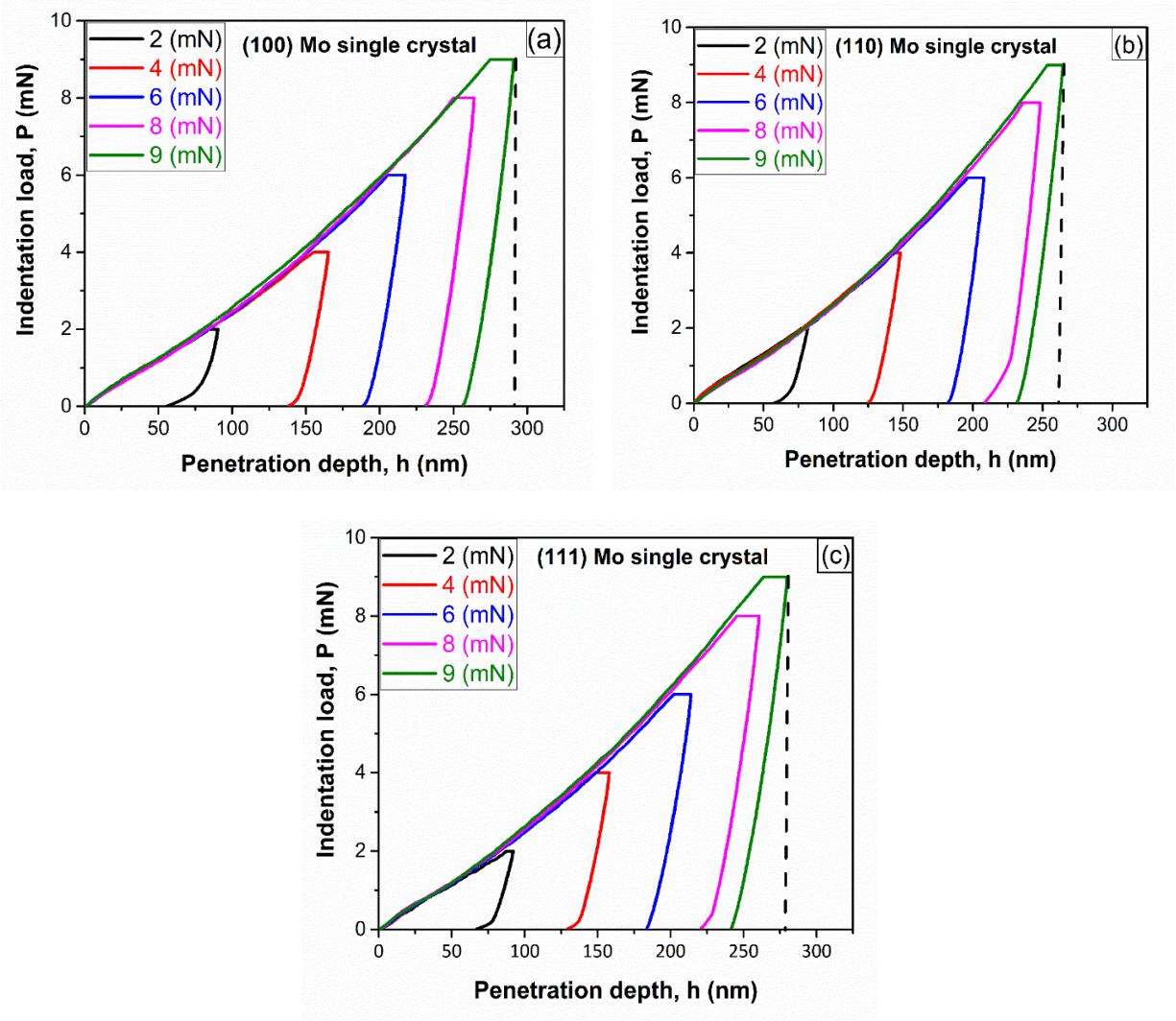

Figure 2.1(a-c): Indentation load, *P* versus penetration depth, *h* curves for (a) (100), (b) (110), and (c) (111) Mo single crystals.

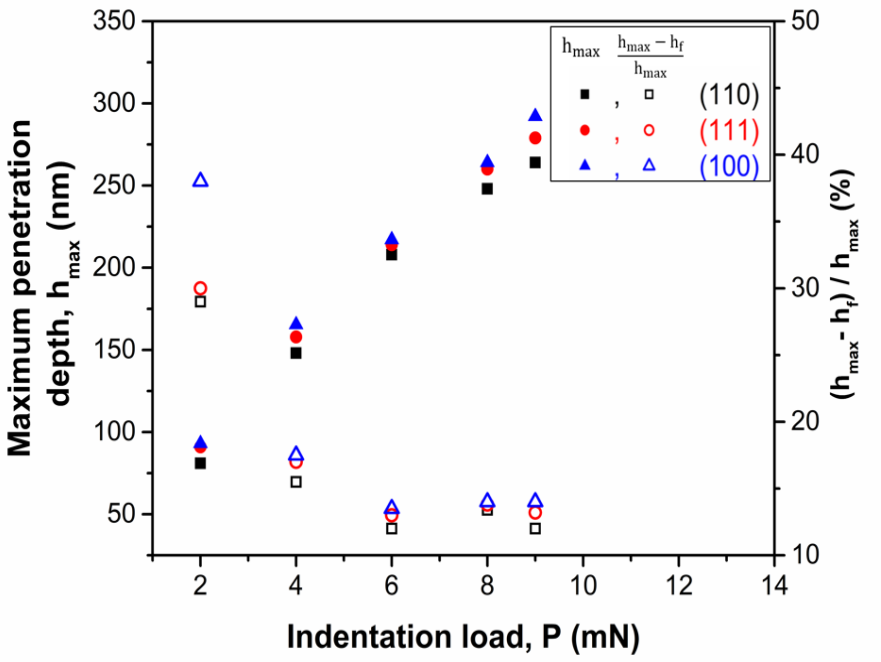

Figure 2.2: Maximum penetration depth, h_{max} (left y-axis and shown with filled symbol) and the ratio of penetration depth recovered during unloading to maximum penetration depth (right y-axis and shown with hollow symbol) plotted against indentation load, *P* for (100), (110), and (111) Mo single crystals.

2.3.1.2 Effect of indentation load on nanohardness

The variation of nanohardness, H_n for (100), (110), and (111) oriented Mo single crystals are plotted against the P_{max}, in Figure 2.3(a). The following observations can be drawn from the Figure 2.3(a): (i) For all the orientation, the H_n decreases with increasing P_{max} showing indentation size effect (ii) At any given P_{max}, hardness of (110) orientation is the highest while (100)is the lowest (iii) The difference in hardness (ΔH) between (110) and (100) orientations at 2 mN is significant (around 14%) which decreases with increasing P_{max} and is found to be only 2.5% at 2 N (for a three orders of increase in P_{max}) as illustrated in Figure 2.3(b). The observed anisotropy in *H* at low indentation loads, among the different orientations, is a direct consequence of the differences in deformation events taking place in the plastic deformation zone under the indentation. The anisotropy in *H* can be explained by considering the Schmid factor for active slip systems

underneath the indentation and the resolved shear stress acting on them. Owing to the pyramidal geometry of the indenter, calculation of Schmid factor under a Berkovich is not straight forward unlike uniaxial compression. In order to compute the Schmid factor under Berkovich indentation, it is assumed that the load is being transmitted to the material along the apex of the tip (the apex of the tip is almost spherical) (Schuh, 2006) and normal to the slanting faces of the indenter following the model proposed by Raineesh et al. (2021). The compressive forces acting normal to the slanting faces of the Berkovich indenter are 120° apart (refer Figure A-1 in APPENDIX-A). We have considered the deformation on {110}<111> and {112}<111> slip systems as these are the most commonly observed deformation systems in BCC metals at room temperature (Seeger, 2001; Seeger, 2004). At lower penetrations depths, the region directly beneath the indenter contributes more to hardness. When the compressive load is transferred to the specimen by the spherical tip present directly beneath the indenter, the maximum numbers of {110}<111> and {112}<111> slip systems along with the maximum Schmid factor for the (100), (110), and (111) orientations are presented in Table 2.1. It should be noted that at least five independent slip systems have to be active for plastic deformation to occur. But it can be seen that only four slip systems from the {110}<111> family can be activated when indentation is performed on the (110) plane (refer Table 2.1). Therefore, {112}<111> slip system must be activated to fulfil the requirement of minimum five active slip systems. However, in the case of other two orientations, the number of {110}<111> variants with non-zero Schmid factor is greater than five, hence {112}<111> slip system need not to get activated. Since the critical resolved shear stress (CRSS) for {110}<111> slip is lesser than that for {112}<111>, (110) is the hardest plane at lower depths. Further, as the indentation depth increases, the compressive forces along the slant faces of the indenter also start contributing to hardness and the procedure for calculation of Schmid factor due to this load is given in APPENDIX-A. The variation of Schmid factor for the two possible slip systems, for (100), (110) and (111) orientations, is plotted against the in-plane rotation angle, θ as shown in Figures 2.4-2.6. From these figures it can be observed that for any θ, both {110}<111> and {112}<111> slip systems have a non-zero Schmid factor along the slant face of indenter for at least one among the three loading directions perpendicular to the faces of Berkovich indenter for all three orientations. Based on this, it can be suggested that the slip occurs on both {110}<111> as well as {112}<111> slip systems in all three orientations under Berkovich indentation. Since, the in-plane orientation, θ is unknown, the exact Schmid factors corresponding to compressive

stresses along the normals to slanting faces cannot be clearly ascertained. For better clarification, an advanced computational technique, such as dislocation dynamics simulation, would be necessary.

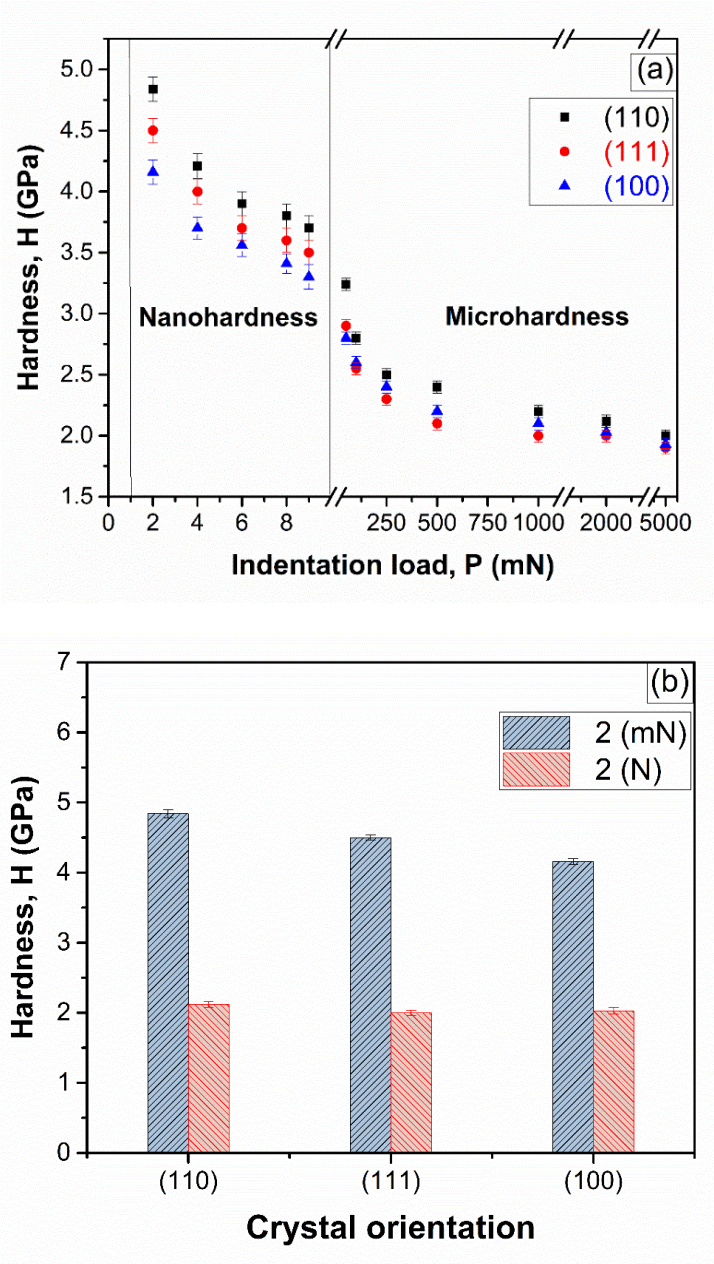

Figure 2.3: (a) Variation of indentation hardness, *H*, plotted as a function of indentation load, *P;* b) summary of nanohardness plotted at two different loads (2mN and 2N) for (100), (110), and (111) Mo single crystals.

A size effect in indentation hardness as seen in Figure 2.3(a) could be caused by strong plastic strain gradients occurring below the indenter in the micro- or nano-meter scale indentations, which can occur when intense plastic deformation is forced to occur over a very small volume of an initially defect-free crystalline material (Haghshenas et al., 2017).

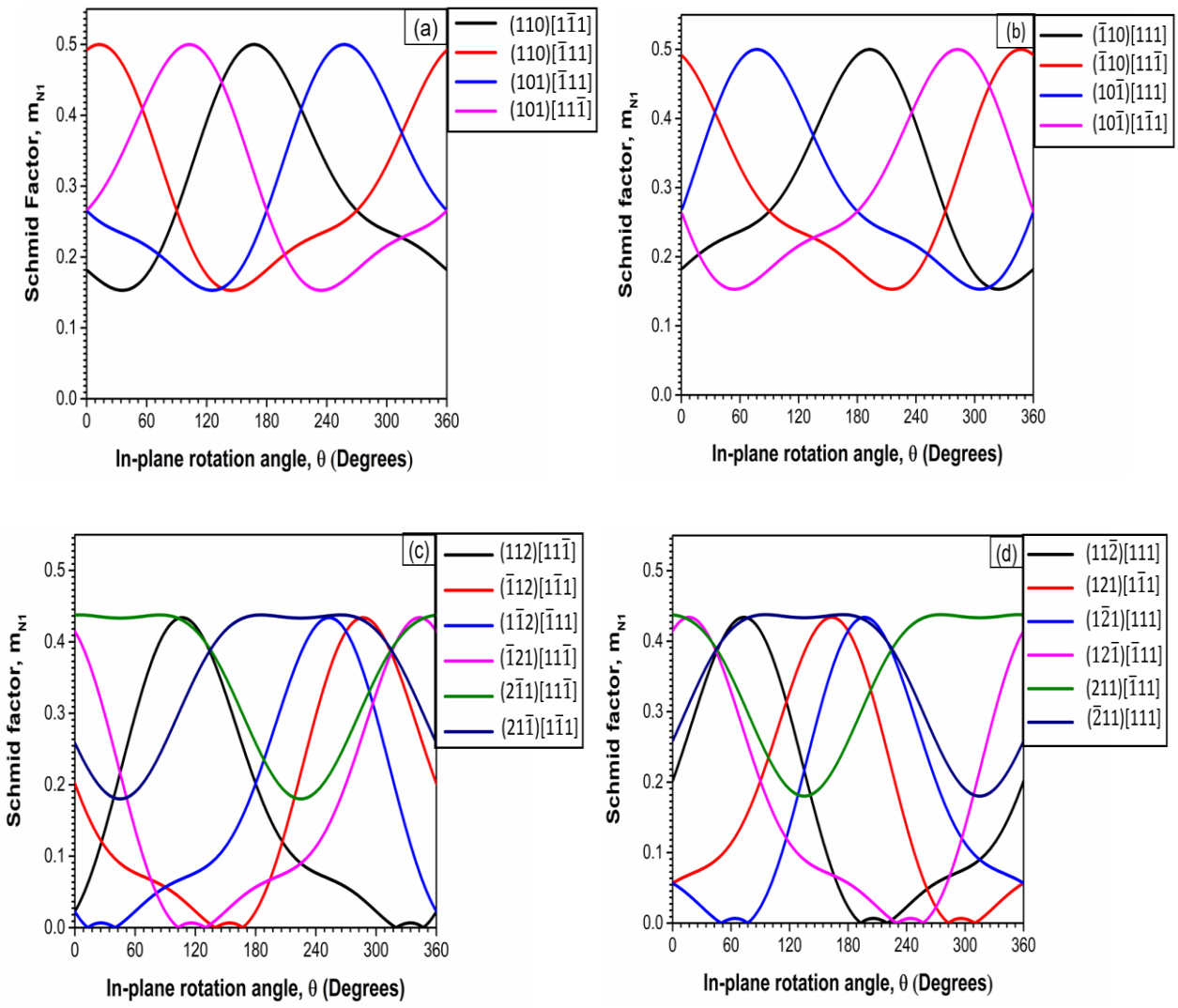

Figure 2.4(a)-(d): Schmid factor variation with in-plane rotation angle, θ when a load is transmitted to the material along N1 loading direction (refer Figure A-1) for {110}<111> and {112}<111> slip systems having higher Schmid factor when the indentation is performed on (100) oriented crystal.

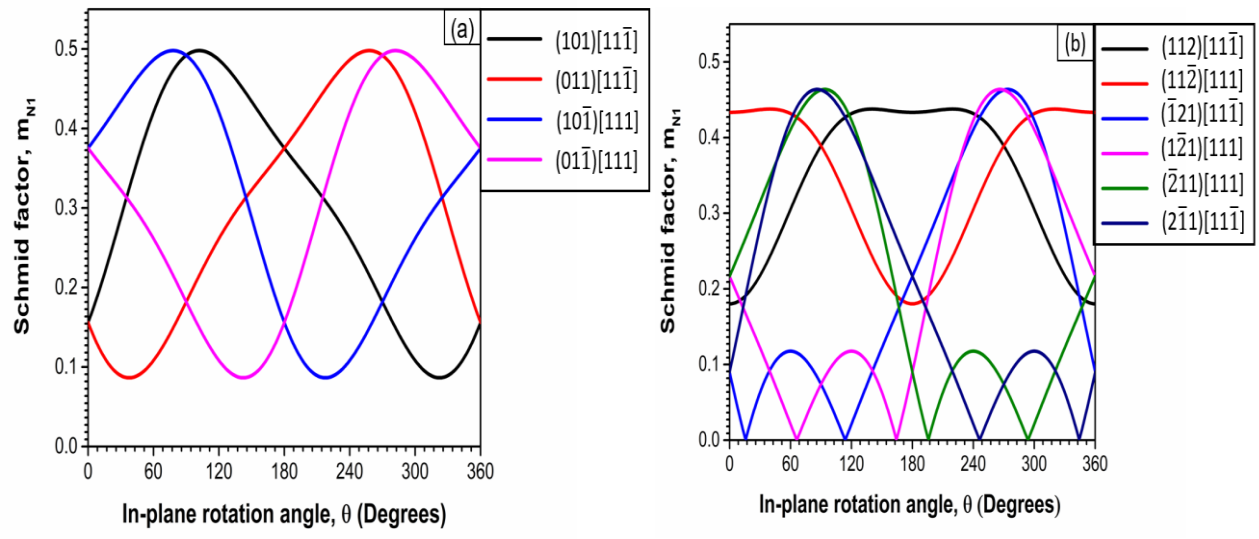

Figure 2.5(a)-(b): Schmid factor variation with in-plane rotation angle, θ when a load is transmitted to the material along N1 loading direction (refer Figure -1A) for {110}<111> and {112}<111> slip systems having higher Schmid factor when the indentation is performed on (110) oriented crystal.

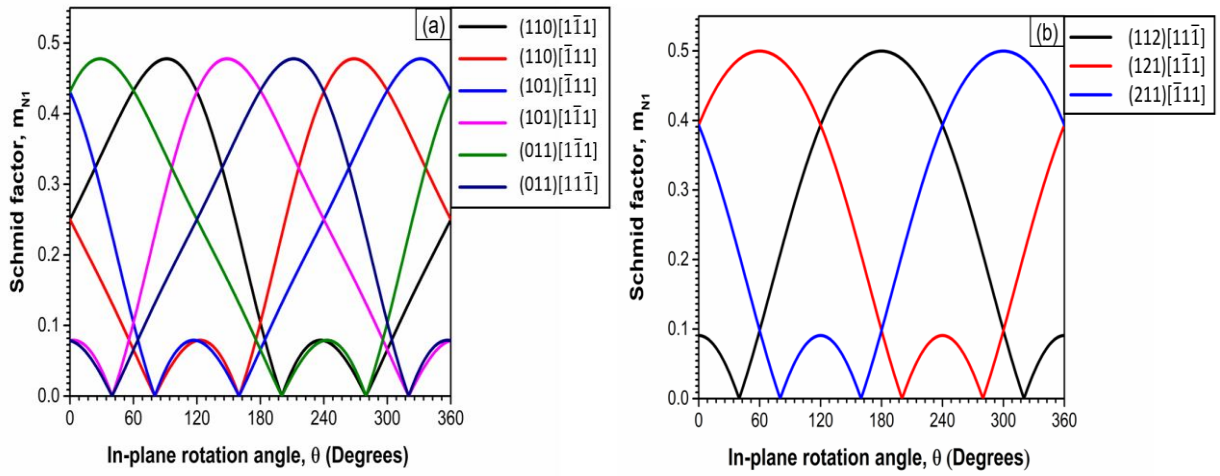

Figure 2.6(a)-(b): Schmid factor variation with in-plane rotation angle, θ when a load is transmitted to the material along N1 loading direction ((refer Figure A-1) for {110}<111> and {112}<111> slip systems having higher Schmid factor when the indentation is performed on (111) oriented crystal.

Table 2.1: The number of slip systems having maximum Schmid factor directly beneath the indenter for the three given orientations.

Indentation Surface	Maximum possible Schmid factor, number of {110} slip systems directly beneath the indenter	Maximum possible Schmid factor, number of {112} slip systems directly beneath the indenter
(100)	0.41, 8	0.47, 4
(110)	0.41, 4	0.47, 2
(111)	0.27, 6	0.31, 3

2.3.2 Microindentation study

2.3.2.1 Effect of indentation load on microhardness

Figure 2.3(a) shows the variation of microhardness (H_m) with indentation load (P). Interestingly, the same trend of decrease in hardness with increasing indentation load is observed below 1000 mN. In the case of microindentation also, the highest hardness is observed on (110) surface. As the applied indentation load during microindentation increases, the difference in hardness between the three samples decreases and saturation in hardness is observed.

In addition, from Figure 2.3(a) it was also observed that the H_m is lower than the nanohardness (H_n) which is attributed the larger strain gradients during nanoindentation in contrast to the microindentation. The large plastic strain gradient (at low penetrations depth) leads to an increase in geometrically necessary dislocations (GNDs) and following Nix-Gao model, it infers why the H_n is higher than the H_m. With increase in indentation depth (vis-à-vis load) the strain gradient decreases and plastic deformation is accommodated by the statistically stored dislocations.

2.3.3 Atomic force microscopy (AFM) images of nano- and micro-indentation

Figure 2.7(a)–(c) show AFM images of the surface topography of Mo single crystals after nanoindentation upto a load of 8mN. A triangular residual impression of the Berkovich indenter can be seen on the indented surface. Pile-up around the indent impression was observed on (100), and (110) oriented crystals but for (111) oriented crystal no significant pile-up was observed. The impression size for (100) orientation is larger, (110) orientation is smaller while for (111) orientation is in intermediate. Therefore, the hardness anisotropy can also be correlated with impression size.

Figure 2.7(d)-(f) show AFM surface topography images of residual Vickers indent impression on the (100), (110), and (111) oriented Mo crystals after the completion of microindentation upto a load of 1000mN. AFM scan images of the indents clearly revealed that the three materials exhibited different plastic deformation phenomena. The patterns of the pile-ups and their maximum height are seemed to depend significantly on the relationship of orientation between the specimens and the indenter. Pile-ups patterns on the surfaces of (100), (110), and (111) oriented Mo single crystals have four-, two-, and three-fold symmetry, respectively. Stelmashenko et al. (1993) observed that in the case of Mo single crystals, the position of Vickers impression pile-ups correlates with the orientation of {110}<111> dislocation slip systems. The pile-up morphology can be attributed to the number of slip systems activated during indentation on a particular surface. A pile-up pattern would result if slip occurs in one of these directions without any kinematic constraint. For (100) and (110) orientations, deformation spread preferentially in <111> out of plane directions. For indentation on (100) plane, slip can occur along the family of <111> slip directions, which lie along <110> directions when projected onto the (100) surface (refer Figure 2.8). Slip in <111> directions combined with the crystallographic symmetry of the (100) plane can cause the four-fold symmetry of <110> pile-ups to form. It is interesting to note that in the case of the (110) orientation, where both in-plane and out-of-plane slip directions are available, the pileup is predominantly found along the out-of-plane <111> slip directions resulting in two fold symmetry (see Figure 2.9). Similarly, Biner et al. (2007) and Yao et al. (2014) also noticed the crystal symmetry in pile-up patterns by conducting nano- and micro-indentation experiments using the spherical indenter on (100), (110), and (111) oriented surfaces of tantalum and tungsten single

crystals. Experimentally, it is not easy to specify the explanation of the relation between the slip system and the pile-up shape.

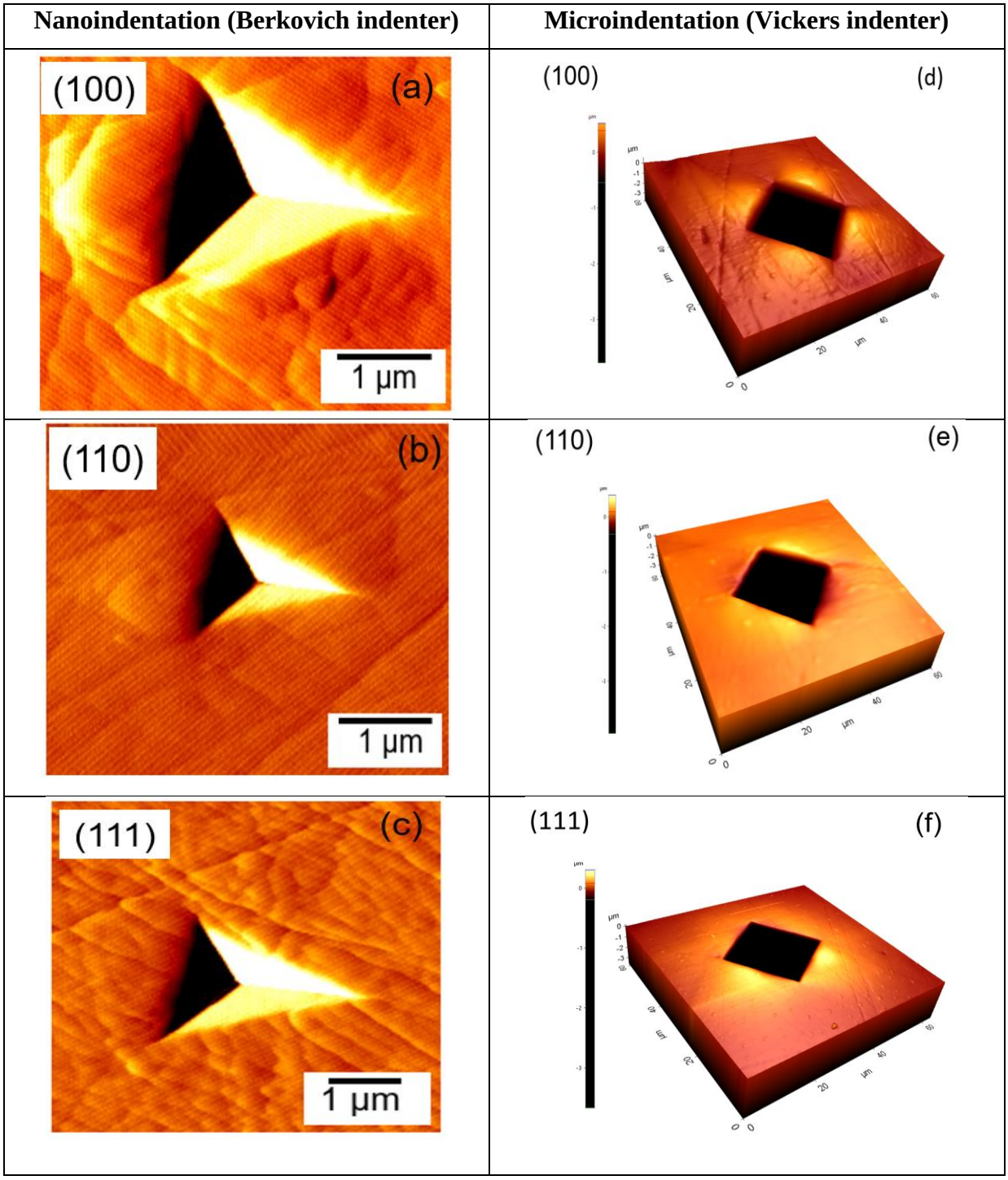

Figure 2.7: AFM surface displacement morphology for (100), (110), and (111) Mo single crystals at 8mN load for Berkovich indenter (left side a-c) and at 1000mN load for Vickers indenter (right side d-f).

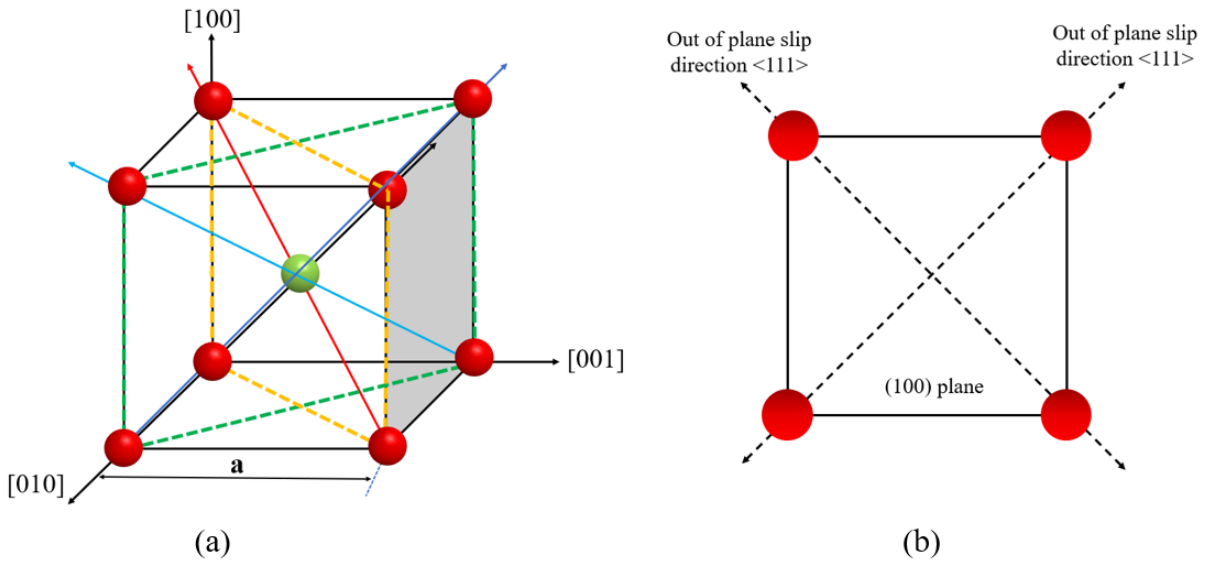

Figure 2.8: Schematic depicting the arrangement of atoms in (a) unit cell along with {110} plane intersecting (100) plane (b) surface layer for crystal orientation (100).

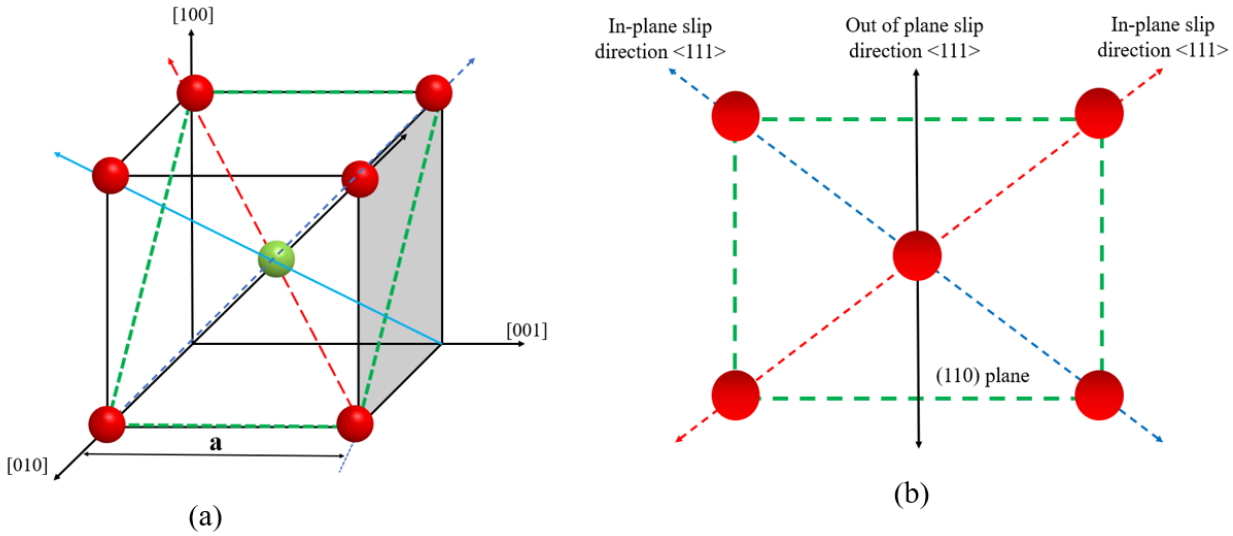

Figure 2.9: Schematic depicting the arrangement of atoms (a) in unit cell along with (110) slip plane and slip directions lying within and out of the (110) slip plane (b) surface layer for crystal orientation (110).

2.3.4 Analysis of indentation size effect

The classical continuum plasticity models do not incorporate any intrinsic microstructural length scale hence they cannot predict and characterize the scale-dependent phenomena observed in nano- or micro-indentation experiments on crystalline materials. The *strain gradient plasticity* (SGP) theory which incorporates the materials length scale can explain the length scale dependent phenomenon in materials. Nix and Gao (1998) extended the concepts of SGP to explain the ISE in hardness. SGP theory assumed that deformation zone underneath the indenter comprises of both SSDs and GNDs and their relative contribution (densities) governs the materials hardness. The density of SSDs, ρ_S arises due to the homogenous strain while the GNDs ρ_G stems from the plastic strain gradients. According to the Nix and Gao model, the mathematical relationship between the indentation hardness, H and the residual indentation depth, h can be defined as:

$$\frac{H^2}{H_0^2} = 1 + \frac{h^*}{h}. \tag{2.6}$$

Here H_0 is the macro-hardness or size-independent hardness and h^* is the characteristic length scale which is not a constant for a given material and indenter geometry. The characteristic length h^* depends on dislocation density, ρ_S through H_0.

Equation (2.6) implies that the plot of H^2 versus 1/h yields a linear fit with H_0 and h^* as the fitting constants. From the estimated numerical values of H_0 and h^*, the micro and nano characteristic length-scale can be approximated using two different approaches. The characteristic length-scale based on the microindentation test is given by (Chicot, 2009)

$$h^*_{micro} = \frac{81}{2} b\alpha^2 \tan^2\theta' \left(\frac{\mu}{H_{0(micro)}}\right)^2. \tag{2.7}$$

Durst et al. (2005) proposed a corrected model which takes into account the effect of GNDs by considering plastically deformed volume instead of volume given by contact radius beneath the indenter. The radius of the assumed hemispherical plastic zone was given as $a_{pz} = f.a_{cr}$ (as shown in Figure 2.10(a)-(b)) where a_{cr} is the contact radius, f is a correction factor ranging from 0 to 3.5, estimated from finite element simulations which, attempts to provide a more precise approximation of the hemispherical volume containing the GNDs into equation (2.7) as follows:

$$h^*_{nano} = \frac{81}{2}\frac{1}{f^3} b\alpha^2 \tan^2\theta' \left(\frac{\mu}{H_{0(nano)}}\right)^2. \quad (2.8)$$

Here b is the Burgers vector, α is a constant, μ is the shear modulus of elasticity and θ' ($tan\ \theta' = 0.358$ (Swadener et al., 2002)) is the angle between the surface of the indenter and the plane of the surface. In the present work $f = 1.9$ by following the work of Durst et al., (2005), $b = 0.278$nm (Wang et al., 2011), $\alpha = 0.5$ (Nix and Gao, 1993), and $\mu = 126$ GPa (Simmons and Wang, 1971). The equation (2.8) leads to equation (2.7) for $f = 1$ in as proposed by Nix and Gao (1993). According to the Taylor relation equivalent flow stress, σ is related to the total dislocation density, ρ_T through equation (2.9):

$$\sigma = \sqrt{3}\alpha\mu b\sqrt{\rho_T}\ . \quad (2.9)$$

Following Tabor relation, hardness, H and equivalent flow stress, σ are related as $H = 3\sigma$. In addition, the total dislocation density, ρ_T is believed to be the arithmetic sum of the density of GNDs and SSDs. i.e., $\rho_T = \rho_G + \rho_S$. Then we may write:

$$H = 3\sigma = 3\sqrt{3}\alpha\mu b\sqrt{\rho_G + \rho_S} \quad (2.10)$$

To relate load-dependent hardness to the strain gradient, Nix and Gao (1993) also determined material intrinsic length scale, $\hat{l}$ from the SGP theory. Using Tabor's relationship (Tabor, 1951) again, equation (2.6) can be rewritten in terms of strain gradient for microindentation:

$$\left(\frac{\sigma}{\sigma_{0(micro)}}\right)^2 = 1 + b\left(\frac{\mu}{\sigma_{0(micro)}}\right)^2 \chi = 1 + \hat{l}_{micro}\chi\ . \quad (2.11)$$

To get the material intrinsic length for nanoindentation by considering the correction factor, f given by Durst et al.(2005), equation (2.6) rewritten in terms of strain gradient for nanoindentation as follow:

$$\left(\frac{\sigma}{\sigma_{0(nano)}}\right)^2 = 1 + \frac{b}{f^3}\left(\frac{\mu}{\sigma_{0(nano)}}\right)^2 \chi = 1 + \hat{l}_{nano}\chi \quad (2.12)$$

In this equation σ_0 is the equivalent flow stress in the absence of a strain gradient χ, and μ is the shear modulus. Equation (2.11) and (2.12) clearly shows the physical meaning of this material intrinsic length scale, $\hat{l}$, i.e., it provides a measure of the contribution of strain gradient to the flow stress.

To cross-validate, the material intrinsic length scale calculated from equation (2.11), another approach proposed in the literature (Nix and Gao, 1998) is based on calculating the yield stress, σ_0 from:

$$\sigma_0 = \sqrt{3}\alpha\mu b\sqrt{\rho_s}\ . \tag{2.13}$$

Here density of SSDs, ρ_s can be approximately as given as

$$\rho_s \approx \frac{1}{L_s^2}\ . \tag{2.14}$$

In equation (2.14) L_s is the average spacing between SSDs. Then intrinsic material length scale for microindentation is given as by (Nix and Gao, 1998)

$$\hat{l}_{micro} = \frac{4}{3}\frac{L_s^2}{b}\ . \tag{2.15}$$

Similarly for nanoindentation by taking into account the correction factor, *f* equation (2.15) can be rewritten as follow:

$$\hat{l}_{nano} = \frac{4}{3}\frac{1}{f^3}\frac{L_s^2}{b} \tag{2.16}$$

To confirm the material intrinsic length scale obtained from equations (2.11) and (2.12) we can use equations (2.15) and (2.16). Equations (2.11) and (2.12) were used to estimate the micro-and nano intrinsic material length-scale based on experimental data provided by the nano-and microindentation experiments.

In Figure 2.11 the H^2 is plotted against 1/*h* from the experimentally obtained data at each indentation load. It can be noticed that the Nix-Gao model cannot fit both the nano and microindentation data simultaneously. Therefore, it can be observed that the slopes of linear function are different in the micro- and nano-indentation regime. The observed bilinear behaviour may be due to a difference in the underlying dislocation mechanisms that gives rise to the ISE in the two different regimes. The values of H_0 and h^* for the nano- and micro-scale indentation regimes are presented in Table 2.2. The parameter h^* is not a constant for a given material it varies in nano and micron scale. The analytically predicted values of h^* from equations (2.7) and (2.8) agree well with the experimentally observed values. The material intrinsic length scales obtained from equations (2.11) and (2.12) for the Mo single crystals are presented in Table 2.3. The difference in length scales observed for nano- and micro-indentation can be attributed to the

uniformity in dislocation spacing underneath the indenter (Chicot, 2009). In case of nanoindentation where the indent size is small and corresponding to the onset of plastic deformation, dislocations are formed in a non-uniform deformation zone formed around the indenter, resulting in non-uniformity in dislocation spacing. However, as the indentation load increases the deformation zone around the indent also increases, and so does the uniformity between the dislocations spacing, resulting in homogeneous arrangement of dislocation around the indent. This results in a difference in dislocation spacing at nano and micron scales, which aids in understanding the difference between length scales resulting from the analysis of nano- and micro-indentation hardness data.

Table 2.2: Comparison of experimentally measured and analytically predicted [Eqs. (2.7) and (2.8)] values of the characteristic length, h^* in nano and micro-indentation.

Orientation	H_0 (GPa) nano	h^* (μm) nano	H_0 (GPa) micro	h^* (μm) micro	h (predicted μm) nano	h (predicted μm) micro
(100)	2.96	0.075	1.88	1.14	0.094	1.59
(110)	3.21	0.087	1.91	1.44	0.081	1.56
(111)	3.08	0.082	1.77	1.41	0.088	1.83

Table 2.3: Calculated material intrinsic length scale for (100), (110), and (111) Mo single crystals.

Orientation	Nano material intrinsic length scale $\hat{l}_{nano}$ (μm)	Micro material intrinsic length scale $\hat{l}_{micro}$ (μm)
(100)	0.65	11.24
(110)	0.55	10.89
(111)	0.6	12.45

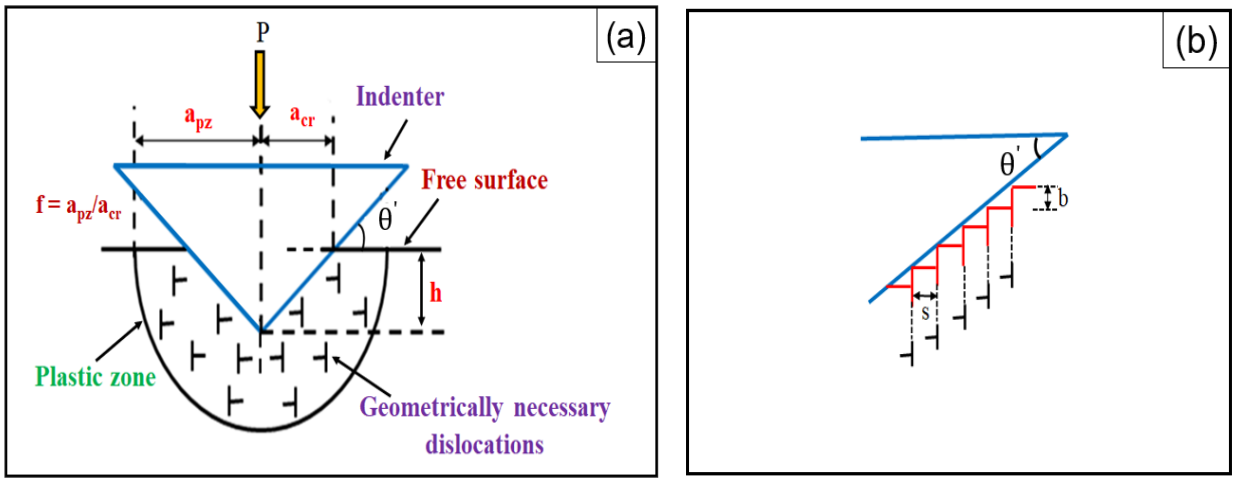

Figure 2.10: (a) Schematic showing the geometrically necessary dislocations formation under the indenter in hemispherical volume; (b) traces due to dislocation slip.

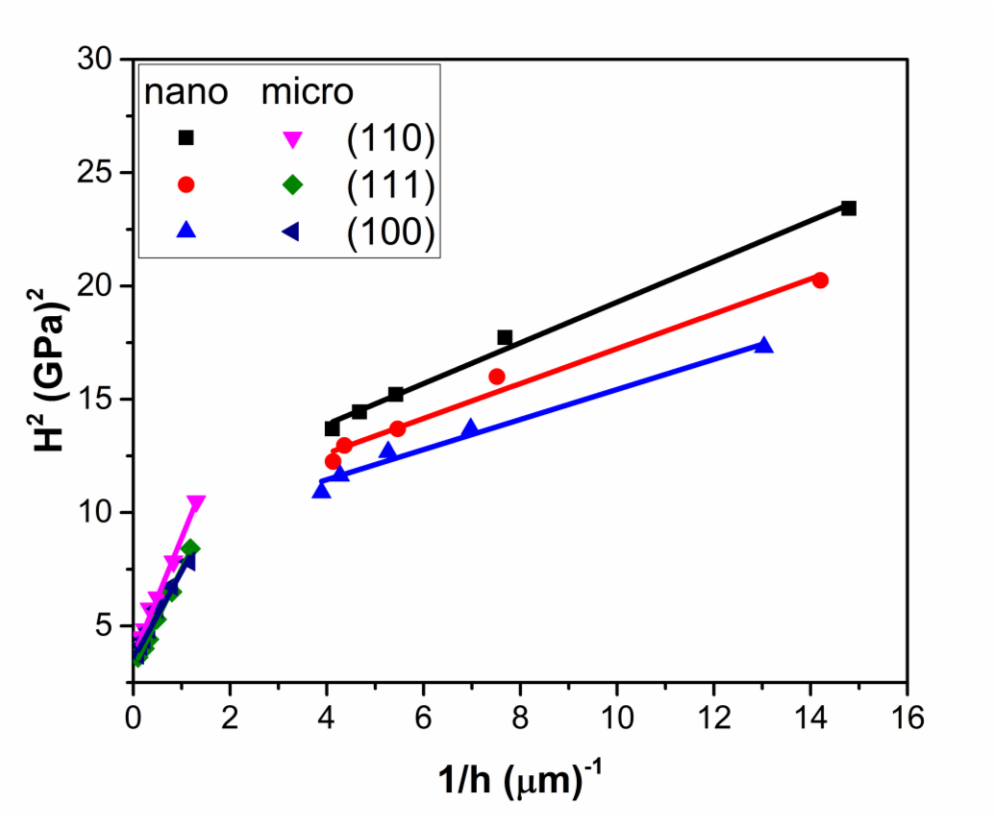

Figure 2.11: Square of nano- and micro-hardness, H^2 plotted as a function of inverse penetration depth, *1/h* for Mo single crystals.

2.4 Summary

In summary, nano- and micro-indentation experiments are performed on (100), (110), (111) oriented Mo single crystals using Vickers and Berkovich indenter, respectively. The effect of load on the nano- as well as micro-hardness is investigated. In addition, the pile-up patterns on the indented surfaces are analyzed by atomic force microscopy (AFM). The active slip systems below the nano-indenter are also investigated by using the model proposed by Raineesh et al. (2021). Finally, the indentation size effect (ISE) was modelled using strain gradient plasticity theory developed by Nix and Gao.

Chapter 3

Crystal plasticity constitutive model and numerical implementation

3.1 Introduction

In chapter 2, it has been shown that that the indentation response as well as the indentation size effect in Molybdenum single Crystals is orientation dependent. However, the mechanistic reasons for this dependence are not well understood. The finite element simulations employing crystal plasticity based constitutive theory would help understanding the indentation response of Mo crystals better. Therefore, in this chapter, the crystal plasticity based constitutive theory for Body Centered Cubic (BCC) single crystals proposed by Daphalpurkar et al. (2018) is briefly discussed. In addition, the finite element procedure to implement this model in commercially available software package Abaqus (Dassault Systèmes, 2017) by writing user element (UEL) subroutine is discussed in detail. This model is chosen because it has been shown to capture rate-, temperature- and orientation-dependent deformation behavior of Mo single crystal.

The outline of this chapter is as follows: the brief discussion on the constitutive model is presented in Section 3.2. The numerical implementation of the model and finite element formulation is discussed in Section 3.3 and 3.4, respectively. In Section 3.5, The material parameters for Mo single crystals are determined by calibrating the model against experimental data from the literature. Finally, the summary of the chapter is presented in Section 3.6.

3.2 Crystal plasticity theory

3.2.1 Kinematics

The general framework for crystal plasticity proposed by Asaro and Needleman (1985) is employed in the model of Daphalpurkar et al. (2018) too. Thus, in the model of Daphalpurkar et al. (2018), the lattice of crystalline material is assumed to first undergoes plastic shearing due to dislocation gliding followed by elastic distortion due to stretching and rotation as displayed in

Figure 3.1. In this figure, the reference configuration represents the crystal lattice in its undeformed state, while the current configuration refers to the crystal lattice in its deformed state. However, the intermediate configuration is obtained by relaxing the elastic stretching and rotation of lattice in the current configuration. Therefore, the deformation gradient tensor, $\boldsymbol{F}$, is decomposed multiplicatively into elastic and plastic components $\boldsymbol{F^e}$ and $\boldsymbol{F^p}$, respectively, as given by:

$$\boldsymbol{F} = \frac{\partial \mathbf{x}}{\partial \mathbf{X}} = \boldsymbol{F^e F^p}. \tag{3.1}$$

Here, **X** and **x** represent the position vector of a material particle in reference and current configurations, respectively, with respect to a fixed Cartesian frame with base vectors $\boldsymbol{e_1}$, $\boldsymbol{e_2}$ and $\boldsymbol{e_3}$. A slip system in a lattice is represented by the unit vectors along the slip direction and slip-plane normal. For instance, α^{th} slip system of a lattice in the reference configuration is specified by the unit vectors $\boldsymbol{s^\alpha}$ and $\boldsymbol{m^\alpha}$, along the slip direction and slip plane normal, respectively. Since the lattice does not rotate through deformation $\boldsymbol{F^p}$, the vectors $\boldsymbol{s^\alpha}$ and $\boldsymbol{m^\alpha}$ for intermediate configuration are identical to that for reference configuration, while they rotate to $\boldsymbol{s^{e(\alpha)}}$ and $\boldsymbol{m^{e(\alpha)}}$ in the current configuration through following relations:

$$\begin{aligned} \boldsymbol{s^{e(\alpha)}} &= \boldsymbol{F^e s^\alpha}, \\ \boldsymbol{m^{e(\alpha)}} &= \boldsymbol{F^{e-T} m^\alpha}. \end{aligned} \tag{3.2}$$

Note that the lattice vectors are orthogonal, and hence satisfy the following relation:

$$\boldsymbol{m^{e(\alpha)}}.\boldsymbol{s^{e(\alpha)}} = \boldsymbol{m^{(\alpha)}}.\boldsymbol{s^{(\alpha)}} = 0. \tag{3.3}$$

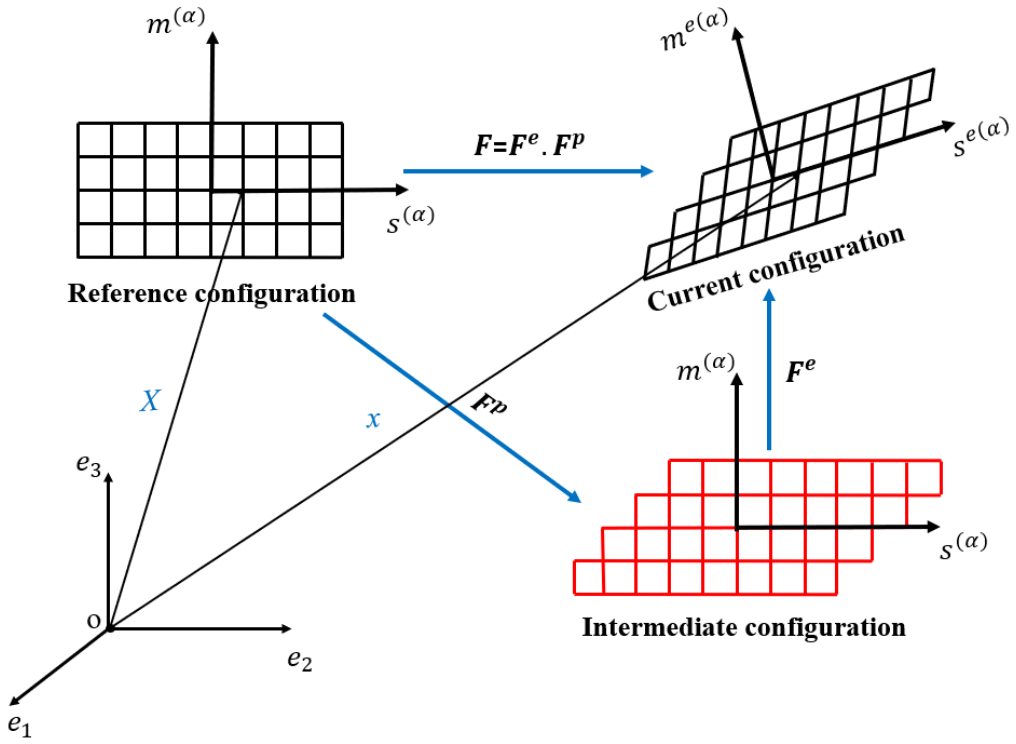

Figure 3.1: Schematic showing the reference, intermediate and current configuration, as well as the decomposition of deformation gradient $\boldsymbol{F}$ into elastic and plastic components $\boldsymbol{F^e}$ and $\boldsymbol{F^p}$.

The spatial velocity gradient, $\boldsymbol{l}$ is given by:

$$\boldsymbol{l} = \frac{\partial \mathbf{v}}{\partial \mathbf{x}} = \frac{\partial \mathbf{v}}{\partial \mathbf{X}}\frac{\partial \mathbf{X}}{\partial \mathbf{x}} = \dot{\boldsymbol{F}}.\boldsymbol{F^{-1}} = \dot{\boldsymbol{F}}^{\boldsymbol{e}}.\boldsymbol{F^{e-1}} + \boldsymbol{F^e}.\dot{\boldsymbol{F}}^{\boldsymbol{p}}.\boldsymbol{F}^{\boldsymbol{p-1}}.\boldsymbol{F^{e^{-1}}} = \boldsymbol{l^e} + \boldsymbol{F^e L^P F^{e^{-1}}} = \boldsymbol{l^e} + \boldsymbol{l^p}. \tag{3.4}$$

Here, $\mathbf{v}$ is the material point velocity in the current configuration, while $\boldsymbol{l^e}$ and $\boldsymbol{l^p}$ are the elastic and plastic components of the spatial velocity gradient, respectively. Further, the evolution equations for $\boldsymbol{F^p}$ (i.e., flow rule) is written in terms of the plastic slip rate, $\dot{\gamma}^{\alpha}$ as:

$$\boldsymbol{L^p} = \dot{\boldsymbol{F}}^{\boldsymbol{p}}\boldsymbol{F^{p-1}} = \sum_{\boldsymbol{\alpha=1}}^{\boldsymbol{n}} \dot{\gamma}^{\alpha}(\boldsymbol{s^{\alpha}} \otimes \boldsymbol{m^{\alpha}}) \tag{3.5}$$

where n is total number slip systems in the crystal. It can be seen from Eq. (3.4) and (3.5) that:

$$\begin{aligned} trace(\boldsymbol{l^p}) \quad &= trace(\boldsymbol{F^e L^P F^{e^{-1}}}) \\ &= \sum_{\alpha=1}^{n} \dot{\gamma}^{\alpha} trace\left(\boldsymbol{F^e}.\left(\boldsymbol{s^{(\alpha)}} \otimes \boldsymbol{m^{(\alpha)}}\right).\boldsymbol{F}^{\boldsymbol{e-1}}\right) = \sum_{\boldsymbol{\alpha=1}}^{\boldsymbol{n}} \dot{\gamma}^{\alpha}\left(\boldsymbol{s^{e(\alpha)}}.\boldsymbol{m^{e(\alpha)}}\right) = 0 \end{aligned} \tag{3.6}$$

This implies that the plastic part of the deformation preserves volume. Further, $\boldsymbol{l}$ can also be written as additive decomposition of stretching rate tensor, $\boldsymbol{D}$ and spin tensor, $\boldsymbol{\Omega}$:

$$\boldsymbol{l} = \boldsymbol{D} + \boldsymbol{\Omega} = \frac{\boldsymbol{1}}{\boldsymbol{2}}(\boldsymbol{l} + \boldsymbol{l^T}) + \frac{\boldsymbol{1}}{\boldsymbol{2}}(\boldsymbol{l} - \boldsymbol{l^T}) \tag{3.7}$$

The tensors $\boldsymbol{D}$ and $\boldsymbol{\Omega}$ can also be expressed as:

$$\begin{aligned} \boldsymbol{D} &= \boldsymbol{D^e} + \boldsymbol{D^p} \\ \boldsymbol{\Omega} &= \boldsymbol{\Omega^e} + \boldsymbol{\Omega^p} \end{aligned} \tag{3.8}$$

Here, $\boldsymbol{D^e}$ and $\boldsymbol{D^p}$ are elastic and plastic parts of stretching tensor, while $\boldsymbol{\Omega^e}$ and $\boldsymbol{\Omega^p}$ are the elastic and plastic parts of spin tensor. $\boldsymbol{l^p}$ in Eq. (3.4) can be written as follows:

$$\boldsymbol{l^p} \;=\; \boldsymbol{D^p} + \boldsymbol{\Omega^p} = \; \boldsymbol{F^e}.\dot{\boldsymbol{F}}^{\boldsymbol{p}}.\boldsymbol{F}^{\boldsymbol{p-1}}.\boldsymbol{F}^{\boldsymbol{e-1}} = \sum_{\alpha=1}^{n} \dot{\gamma}^{\alpha}\left(\boldsymbol{s^{e(\alpha)}} \otimes \boldsymbol{m^{e(\alpha)}}\right), \tag{3.9}$$

where,

$$\begin{aligned} \boldsymbol{D^p} &= \frac{\boldsymbol{1}}{\boldsymbol{2}}\left(\boldsymbol{l^p} + \boldsymbol{l^{p^T}}\right) = \sum_{\alpha=1}^{n} \dot{\gamma}^{\alpha} \frac{1}{2}\left(\boldsymbol{s^{e(\alpha)}} \otimes \boldsymbol{m^{e(\alpha)}} + \boldsymbol{m^{e(\alpha)}} \otimes \boldsymbol{s^{e(\alpha)}}\right) = \sum_{\alpha=1}^{n} \dot{\gamma}^{\alpha} \boldsymbol{\mu^{\alpha}}\,, \\ \boldsymbol{\Omega^p} &= \frac{\boldsymbol{1}}{\boldsymbol{2}}\left(\boldsymbol{l^p} - \boldsymbol{l^{p^T}}\right) = \sum_{\alpha=1}^{n} \dot{\gamma}^{\alpha} \frac{1}{2}\left(\boldsymbol{s^{e(\alpha)}} \otimes \boldsymbol{m^{e(\alpha)}} - \boldsymbol{m^{e(\alpha)}} \otimes \boldsymbol{s^{e(\alpha)}}\right) = \sum_{\alpha=1}^{n} \dot{\gamma}^{\alpha} \boldsymbol{\omega^{\alpha}}. \end{aligned} \tag{3.10}$$

In Eq. (3.10) the tensors $\boldsymbol{\mu^{\alpha}}$ and $\boldsymbol{\omega^{\alpha}}$ are given by:

$$\begin{aligned} \boldsymbol{\mu^{\alpha}} &= \frac{1}{2}\left(\boldsymbol{s^{e(\alpha)}} \otimes \boldsymbol{m^{e(\alpha)}} + \boldsymbol{m^{e(\alpha)}} \otimes \boldsymbol{s^{e(\alpha)}}\right), \\ \boldsymbol{\omega^{\alpha}} &= \frac{1}{2}\left(\boldsymbol{s^{e(\alpha)}} \otimes \boldsymbol{m^{e(\alpha)}} - \boldsymbol{m^{e(\alpha)}} \otimes \boldsymbol{s^{e(\alpha)}}\right), \end{aligned} \tag{3.11}$$

3.2.2 Constitutive law

The following form of constitutive relation is considered assuming the elastic properties being independent of plastic slip in the lattice (Daphalpurkar et al., 2018):

$$\boldsymbol{\tau}^{\boldsymbol{\nabla e}} = \boldsymbol{L}\colon \boldsymbol{D}^{\boldsymbol{e}}. \tag{3.12}$$

Here, $\boldsymbol{L}$ is elastic moduli and $\boldsymbol{\tau}^{\boldsymbol{\nabla e}}$ is the Jaumann rate of Kirchhoff stress determined using lattice spin. $\boldsymbol{\tau}^{\boldsymbol{\nabla e}}$ is given as:

$$\boldsymbol{\tau}^{\boldsymbol{\nabla e}} = \dot{\boldsymbol{\tau}} - \boldsymbol{\Omega}^{\boldsymbol{e}}\boldsymbol{\tau} + \boldsymbol{\tau}\boldsymbol{\Omega}^{\boldsymbol{e}}. \tag{3.13}$$

In the above equation, $\boldsymbol{\tau}$ and $\dot{\boldsymbol{\tau}}$ are Kirchhoff stress and its material time derivative, respectively. Note that $\boldsymbol{\tau}^{\boldsymbol{\nabla e}}$ is a corotational rate of Kirchoff stress on axes that rotates with the crystal lattice from intermediate to current configuration. It is assumed that the elasticity of crystal is unaffected by slip, therefore $\boldsymbol{\tau}^{\boldsymbol{\nabla e}}$ can be related to the elastic rate of stretching through the tensor of elastic moduli $\boldsymbol{L}$. The Jaumann rate of Kirchhoff stress, $\boldsymbol{\tau}^{\boldsymbol{\nabla}}$ based on the material spin $\boldsymbol{\Omega}$ is given as follows:

$$\boldsymbol{\tau}^{\boldsymbol{\nabla}} = \dot{\boldsymbol{\tau}} - \boldsymbol{\Omega}\boldsymbol{\tau} + \boldsymbol{\tau}\boldsymbol{\Omega} \tag{3.14}$$

Note that $\boldsymbol{\tau}^{\boldsymbol{\nabla}}$ is the corotational stress rate of Kirchoff stress on axes that rotates with the material from reference to current configuration. Eq. (3.13)-Eq. (3.14) results in:

$$\boldsymbol{\tau}^{\boldsymbol{\nabla e}} - \boldsymbol{\tau}^{\boldsymbol{\nabla}} = \sum_{\alpha=1}^{n} \dot{\gamma}^{\alpha}\, \boldsymbol{\beta}^{\boldsymbol{\alpha}} \tag{3.15}$$

where $\boldsymbol{\beta}^{\boldsymbol{\alpha}}$ is defined by:

$$\boldsymbol{\beta}^{\boldsymbol{\alpha}} = \boldsymbol{\omega}^{\boldsymbol{\alpha}}\boldsymbol{\tau} - \boldsymbol{\tau}\boldsymbol{\omega}^{\boldsymbol{\alpha}} \tag{3.16}$$

In the absence of relative motion between material and lattice, the right-hand side of above equation would vanish. From Eqs. (3.10a), (3.12) and (3.15), the constitutive law can be written as:

$$\boldsymbol{\tau}^{\boldsymbol{\nabla}} = \boldsymbol{L}\colon \boldsymbol{D} - \sum_{\alpha=1}^{n} \dot{\gamma}^{\alpha}\, (\boldsymbol{L}\colon \boldsymbol{\mu}^{\boldsymbol{\alpha}} + \boldsymbol{\beta}^{\boldsymbol{\alpha}}) \triangleq \boldsymbol{L}\colon \boldsymbol{D} - \sum_{\alpha=1}^{n} \dot{\gamma}^{\alpha}\, \boldsymbol{R}^{\boldsymbol{\alpha}}, \tag{3.17}$$

where,

$$\boldsymbol{R^{\alpha}} = \boldsymbol{L}: \boldsymbol{\mu^{\alpha}} + \boldsymbol{\beta^{\alpha}} \tag{3.18}$$

3.2.3 Plastic slip rate:

The resolved shear stress or Schmid stress, τ^{α} is given by:

$$\tau^{\alpha} = \boldsymbol{\tau}: \left(\boldsymbol{s^{e(\alpha)}} \otimes \boldsymbol{m^{e(\alpha)}}\right) = \boldsymbol{\tau}: \boldsymbol{\mu^{\alpha}} . \tag{3.19}$$

The plastic slip in α^{th} slip system is assumed to evolve as:

$$\dot{\gamma}^{\alpha} = \begin{cases} 0 & if\ \tau^{\alpha}{}_{eff} \leq 0 \\ \dot{\gamma}_0 exp\left(-\frac{\Delta G_k}{\kappa T}\right) & if\ \tau^{\alpha}{}_{eff} > 0 \end{cases} . \tag{3.20}$$

Here, $\dot{\gamma}_0$ is the reference shear strain rate, κ denote Boltzmann's constant, and T is the temperature. Further, ΔG_k is the activation energy and it is given by (Kocks et al., 1975):

$$\Delta G_k = \Delta G_{k_0}\left[1 - \left(\frac{\tau^{\alpha}{}_{eff}}{\tau_0}\right)^{p}\right]^{q}, \tag{3.21}$$

where, ΔG_{k_0} denotes the total activation enthalpy required to overcome the obstacles to slip in the absence of applied stresses, while τ_0 represents the resolved yield strength at 0 K. Further, the parameters $0 < p < 1$ and $1 < q < 2$ are fitting constants. Moreover, τ^{α}_{eff} is the "effective resolved shear stress" which is defined as:

$$\tau^{\alpha}{}_{eff} = \left|\tau^{e(\alpha)}\right| - g^{\alpha}. \tag{3.22}$$

Here, $\tau^{e(\alpha)}$ is a "generalized resolved shear stress" and g^{α} is the athermal component of slip resistance. Note that the motion of dislocation in a particular slip system of a BCC crystal is also influenced by stresses other than the one resolved on that slip plane along the slip direction. In BCC crystals, this behavior is referred to as the non-Schmid behavior. To account the effect of non-Schmid stresses, the following yield criterion proposed by Bassani et al. (2001); Vitek et al. (2004) as well as Gröger et al. (2008) for BCC metals is incorporated in this study. This criterion is given by Eq. 1.4.

The non-Schmid stresses, ${\tau_{1-5}}^{\alpha}$ are defined as follows:

$$\begin{aligned}
{\tau_1}^{\alpha} &= \boldsymbol{\tau}:\left(\boldsymbol{s}^{\mathbf{e}(\alpha)} \otimes {\boldsymbol{n_1}}^{\mathbf{e}(\alpha)}\right) = \boldsymbol{\tau}:\boldsymbol{\mu_1^{\alpha}},\\
{\tau_2}^{\alpha} &= \boldsymbol{\tau}:\left(\boldsymbol{s}^{\mathbf{e}(\alpha)} \otimes {\boldsymbol{n_2}}^{\mathbf{e}(\alpha)}\right) = \boldsymbol{\tau}:\boldsymbol{\mu_2^{\alpha}},\\
{\tau_3}^{\alpha} &= \boldsymbol{\tau}:\left(\left(\boldsymbol{s}^{\mathbf{e}(\alpha)} \times \boldsymbol{m}^{\mathbf{e}(\alpha)}\right) \otimes \boldsymbol{m}^{\mathbf{e}(\alpha)}\right) = \boldsymbol{\tau}:\boldsymbol{\mu_3^{\alpha}},\\
{\tau_4}^{\alpha} &= \boldsymbol{\tau}:\left(\left({\boldsymbol{n_1}}^{\mathbf{e}(\alpha)} \times \boldsymbol{s}^{\mathbf{e}(\alpha)}\right) \otimes {\boldsymbol{n_1}}^{\mathbf{e}(\alpha)}\right) = \boldsymbol{\tau}:\boldsymbol{\mu_4^{\alpha}},\\
{\tau_5}^{\alpha} &= \boldsymbol{\tau}:\left({\boldsymbol{n_2}}^{\mathbf{e}(\alpha)} \times \boldsymbol{s}^{\mathbf{e}(\alpha)}\right) \otimes {\boldsymbol{n_2}}^{\mathbf{e}(\alpha)}\right) = \boldsymbol{\tau}:\boldsymbol{\mu_5^{\alpha}}
\end{aligned} \tag{3.23}$$

Here, $\boldsymbol{n_1^{e(\alpha)}}$ and $\boldsymbol{n_2^{e(\alpha)}}$ are normal vectors to the non-glide planes for α^{th} slip system in the current configuration, which are defined as ${\boldsymbol{n_1}}^{\mathbf{e}(\alpha)} = \boldsymbol{F^{e^{-T}}}{\boldsymbol{n_1}}^{(\alpha)}$ and ${\boldsymbol{n_2}}^{\mathbf{e}(\alpha)} = \boldsymbol{F^{e^{-T}}}{\boldsymbol{n_2}}^{(\alpha)}$, respectively. The vectors, ${\boldsymbol{n_1}}^{(\alpha)}$ and ${\boldsymbol{n_2}}^{(\alpha)}$ in the reference configuration for systems involving slips on {110} planes are listed in Table 1.1. Further, tensors $\boldsymbol{\mu_{1-5}^{\alpha}}$ in Eq. (3.23) are given by:

$$\begin{aligned}
\boldsymbol{\mu_1^{\alpha}} &= \frac{\mathbf{1}}{\mathbf{2}}\left[\left(\boldsymbol{s}^{\mathbf{e}(\alpha)} \otimes {\boldsymbol{n_1}}^{\mathbf{e}(\alpha)}\right) + \left(\boldsymbol{s}^{\mathbf{e}(\alpha)} \otimes {\boldsymbol{n_1}}^{\mathbf{e}(\alpha)}\right)^{\boldsymbol{T}}\right],\\
\boldsymbol{\mu_2^{\alpha}} &= \frac{\mathbf{1}}{\mathbf{2}}\left[\left(\boldsymbol{s}^{\mathbf{e}(\alpha)} \otimes {\boldsymbol{n_2}}^{\mathbf{e}(\alpha)}\right) + \left(\boldsymbol{s}^{\mathbf{e}(\alpha)} \otimes {\boldsymbol{n_2}}^{\mathbf{e}(\alpha)}\right)^{\boldsymbol{T}}\right],\\
\boldsymbol{\mu_3^{\alpha}} &= \frac{\mathbf{1}}{\mathbf{2}}\left[\left(\left(\boldsymbol{s}^{\mathbf{e}(\alpha)} \times \boldsymbol{m}^{\mathbf{e}(\alpha)}\right) \otimes \boldsymbol{m}^{\mathbf{e}(\alpha)}\right) + \left(\left(\boldsymbol{s}^{\mathbf{e}(\alpha)} \times \boldsymbol{m}^{\mathbf{e}(\alpha)}\right) \otimes \boldsymbol{m}^{\mathbf{e}(\alpha)}\right)^{\boldsymbol{T}}\right],\\
\boldsymbol{\mu_4^{\alpha}} &= \frac{\mathbf{1}}{\mathbf{2}}\left[\left(\left({\boldsymbol{n_1}}^{\mathbf{e}(\alpha)} \times \boldsymbol{s}^{\mathbf{e}(\alpha)}\right) \otimes {\boldsymbol{n_1}}^{\mathbf{e}(\alpha)}\right) + \left(\left({\boldsymbol{n_1}}^{\mathbf{e}(\alpha)} \times \boldsymbol{s}^{\mathbf{e}(\alpha)}\right) \otimes {\boldsymbol{n_1}}^{\mathbf{e}(\alpha)}\right)^{\boldsymbol{T}}\right],\\
\boldsymbol{\mu_5^{\alpha}} &= \frac{\mathbf{1}}{\mathbf{2}}\left[\left({\boldsymbol{n_2}}^{\mathbf{e}(\alpha)} \times \boldsymbol{s}^{\mathbf{e}(\alpha)}\right) \otimes {\boldsymbol{n_2}}^{\mathbf{e}(\alpha)}\right) + \left({\boldsymbol{n_2}}^{\mathbf{e}(\alpha)} \times \boldsymbol{s}^{\mathbf{e}(\alpha)}\right) \otimes {\boldsymbol{n_2}}^{\mathbf{e}(\alpha)}\right)^{\boldsymbol{T}}\right]
\end{aligned} \tag{3.24}$$

It should be noted that non-glide shear stresses, ${\tau_1}^{\alpha}$ and ${\tau_2}^{\alpha}$ are parallel to the Burgers vector, while ${\tau_3}^{\alpha}$, ${\tau_4}^{\alpha}$ and ${\tau_5}^{\alpha}$ are normal to the Burgers vector (refer Sec. 1.4.3 and Figure 1.12). The non-glide shear stresses (${\tau^{\alpha}}_{1-5}$) that affect the slip on $\{112\} < 111 >$ slip systems pertain to those non-glide shear stresses which affect the slip on their conjugate pair of {110}<111> slip systems. Consider the case where slip on $(1\bar{1}\bar{2})[1\bar{1}1]$ (α = 22 in Table 1.2 in chapter 1) corresponds to equal slip on systems $(10\bar{1})[\,1\bar{1}1]$ and $(011)[\,1\bar{1}1]$ (α = 10 and 11 in Table 1.1 in chapter 1), and therefore, the set of non-glide shear stresses for this slip system could be derived as ${\tau^{22}}_{1-5} = ({\tau^{10}}_{1-5} - {\tau^{11}}_{1-5})/\sqrt{3}$.

3.2.4 Slip resistance and hardening model

The strain hardening in a crystal is governed by the evolution of slip resistance g^{α}. Following Peirce et al. (1983), g^{α} is assumed to evolve as:

$$\dot{g}^{\alpha} = \sum_{\beta=1}^{n} h_{\alpha\beta} \left| \dot{\gamma}^{\beta} \right|, \tag{3.25}$$

where, $\dot{\gamma}^{\beta}$ is the plastic slip rate on the β^{th} slip system. Further in the above equation, $h_{\alpha\beta}$ is latent hardening moduli which represent the rate of strain hardening on α^{th} slip system due to the action on the β^{th} slip system. The $h_{\alpha\beta}$ is given by (Bassani and Wu, 1991):

$$h_{\alpha\beta} = h^{\alpha} q_{\alpha\beta}, \tag{3.26}$$

where, the parameter h^{α} represents the self-hardening rate of α^{th} slip system, while $q_{\alpha\beta}$ is an amplification factors in the hardening. Following Bassani and Wu (1991), h_{α} is determined as:

$$h_{\alpha} = {h_s}^{\alpha} + ({h_0}^{\alpha} - {h_s}^{\alpha}) \operatorname{sech}^2 \left(\frac{{h_0}^{\alpha} - {h_s}^{\alpha}}{{g_s}^{\alpha} - {g_0}^{\alpha}} \gamma^{\alpha} \right). \tag{3.27}$$

Total plastic slip is the summation of the plastic slip in all the slip systems is given by γ_t as follows:

$$\gamma_t = \sum_{\alpha} \gamma^{\alpha}. \tag{3.28}$$

In Eq. (3.27), h_0^{α} and h_s^{α} represent initial and saturation hardening rate for α^{th} slip system, respectively. Further, g_0^{α} is the initial slip resistance value (or initial critical resolved shear stress) and is kept constant throughout the deformation, while and g_s^{α} is the saturation slip resistance. The values of amplitude factors $q_{\alpha\beta}$ in Eq. (3.26) depend on the nature of dislocation junction formed between α^{th} and β^{th} slip systems governing the latent hardening behavior of crystal. Lee et al. (1999) discussed the various possible dislocation junctions for the 24 slip systems in a BCC crystal and provided the corresponding values of $q_{\alpha\beta}$ in the form of a matrix which is reproduced in Table 3.1. The letters N, C, G, S and W in this table represent no junction, coplanar junction, glissile, strong sessile and weak sessile junctions, respectively, while the diagonal represents self-hardening. Further, the numerical values of these letters are listed in Table 3.2.

Table 3.1: The amplitude factor (latent hardening) matrix $q_{\alpha\beta}$ reproduced from Lee et al. (1999).

#	1	2	3	4	5	6	7	8	9	10	11	12	13	14	15	16	17	18	19	20	21	22	23	24
1	1	N	N	N	N	N	C	G	G	G	G	G	S	S	G	S	W	S	S	S	G	S	W	S
2	N	1	N	N	N	N	G	W	S	S	S	S	S	S	G	W	S	S	S	S	G	S	S	W
3	N	N	1	N	N	N	G	S	W	S	S	S	G	G	C	G	G	G	W	S	G	S	S	S
4	N	N	N	1	N	N	G	S	S	W	S	S	S	W	G	S	S	S	S	W	G	S	S	S
5	N	N	N	N	1	N	G	S	S	S	W	S	W	S	G	S	S	S	G	G	C	G	G	G
6	N	N	N	N	N	1	G	S	S	S	S	W	S	S	G	S	S	W	S	S	G	W	S	S
7	C	G	G	G	G	G	1	N	N	N	N	N	S	S	W	S	G	S	S	S	W	S	G	S
8	G	W	S	S	S	S	N	1	N	N	N	N	S	S	S	W	G	S	S	W	S	S	G	S
9	G	S	W	S	S	S	N	N	1	N	N	N	G	G	G	G	C	G	W	S	S	S	G	S
10	G	S	S	W	S	S	N	N	N	1	N	N	S	S	S	S	G	W	S	S	S	S	G	W
11	G	S	S	S	W	S	N	N	N	N	1	N	W	S	S	S	G	S	G	G	G	G	C	G
12	G	S	S	S	S	W	N	N	N	N	N	1	S	W	S	S	G	S	S	S	S	W	G	S
13	S	S	G	S	W	S	S	S	G	S	W	S	1	N	N	N	N	N	C	G	G	G	G	G
14	S	S	G	W	S	S	S	S	G	S	S	W	N	1	N	N	N	N	G	W	S	S	S	S
15	G	G	C	G	G	G	W	S	G	S	S	S	N	N	1	N	N	N	G	S	W	S	S	S
16	S	W	G	S	S	S	S	W	G	S	S	S	N	N	N	1	N	N	G	S	S	W	S	S
17	W	S	G	S	S	S	G	G	C	G	G	G	N	N	N	N	1	N	G	S	S	S	W	S
18	S	S	G	S	S	W	S	S	G	W	S	S	N	N	N	N	N	1	G	S	S	S	S	W
19	S	S	W	S	G	S	S	S	W	S	G	S	C	G	G	G	G	G	1	N	N	N	N	N
20	S	S	S	W	G	S	S	W	S	S	G	S	G	W	S	S	S	S	N	1	N	N	N	N
21	G	G	G	G	C	G	W	S	S	S	G	S	G	S	W	S	S	S	N	N	1	N	N	N
22	S	S	S	S	G	W	S	S	S	S	G	W	G	S	S	W	S	S	N	N	N	1	N	N
23	W	S	S	S	G	S	G	G	G	G	C	G	G	S	S	S	W	S	N	N	N	N	1	N
24	S	W	S	S	G	S	S	S	S	W	G	S	G	S	S	S	S	W	N	N	N	N	N	1

Table 3.2: The values of letters appearing in Table 3.1 taken from the work of Lee et al. (1999).

N	C	G	S	W
1.0	1.0	1.0	1.4	1.4

3.3 Implementation of constitutive model

3.3.1 Rate tangent formulation

In this work, the rate tangent modulus method proposed by Peirce et al. (1983) is employed to implement the constitutive model discussed in Sec. 3.2 in a commercially available software package Abaqus (Dassault Systèmes, 2017). In this scheme, first an estimation of the change in shear strain during the current time increment is made, and then the elastic-plastic forward gradient modulus relating the increments of stress to that strain is derived. The increment in plastic slip on α^{th} slip system is defined as:

$$\Delta\gamma^{\alpha} = \gamma^{\alpha}(t + \Delta t) - \gamma^{\alpha}(t). \tag{3.29}$$

By employing linear interpolation within the time increment Δt, the above equation can be written as:

$$\Delta\gamma^{\alpha} = [(1-\theta)\dot{\gamma}^{\alpha}(t) + \theta\dot{\gamma}^{\alpha}(t + \Delta t)]\Delta \mathrm{t}, \tag{3.30}$$

where parameter θ lies in the range of 0 to 1. Note that $\theta = 0$ indicates a simple forward-Euler time integration method, while $\theta = 1$ indicates backward-Euler integration method. In the current work, θ = 0.5 is considered. It can be observed from Eq. (3.20) and (3.21) that the rate of plastic slip is a function of τ^{α}_{eff} and T. Therefore, by applying Taylor series expansion (only first order term), $\dot{\gamma}^{\alpha}\ (t + \Delta t)$ in Eq. (3.30) can be approximated as:

$$\dot{\gamma}^{\alpha}(t + \Delta t) = \dot{\gamma}^{\alpha}(t) + \left.\frac{\partial\dot{\gamma}^{\alpha}}{\partial{\tau^{\alpha}}_{eff}}\right|_t \Delta{\tau^{\alpha}}_{eff} + \left.\frac{\partial\dot{\gamma}^{\alpha}}{\partial T}\right|_t \Delta T. \tag{3.31}$$

The partial differentiation Eq. (3.20) with respect to τ^{α}_{eff} and T and invoking of Eq. (3.21) results in:

$$\left.\frac{\partial\dot{\gamma}^{\alpha}}{\partial{\tau^{\alpha}}_{eff}}\right|_t = \mathcal{A}^{\alpha}\left(\frac{\dot{\gamma}^{\alpha}(t)}{\tau_0}\right) \tag{3.32}$$

where,

$$\mathcal{A}^{\alpha} = \left(\frac{\Delta \mathrm{G_{k0}}}{\kappa T}\right)(pq)\left[1 - \left(\frac{{\tau^{\alpha}}_{eff}}{\tau_0}\right)^{p}\right]^{q-1}\left(\frac{{\tau^{\alpha}}_{eff}}{\tau_0}\right)^{p-1}, \tag{3.33}$$

and,

$$\left.\frac{\partial\dot{\gamma}^{\alpha}}{\partial T}\right|_t = \left(\frac{\Delta \mathrm{G_{k0}}}{\kappa T}\right)\left(\frac{\dot{\gamma}^{\alpha}(t)}{T}\right) \tag{3.34}$$

Further, $\Delta{\tau^{\alpha}}_{eff}$ can be determined from Eq. (3.22) and (1.4) as:

$$\Delta{\tau^{\alpha}}_{eff} = |\Delta\tau^{\alpha} + a_1\Delta{\tau_1}^{\alpha} + a_2\Delta{\tau_2}^{\alpha} + a_3\Delta{\tau_3}^{\alpha} + a_4\Delta{\tau_4}^{\alpha} + a_5\Delta{\tau_5}^{\alpha}| - \Delta g^{\alpha} \tag{3.35}$$

The time derivative of τ^{α} can be determined from Eq. (3.19) and using Eq. (3.2) as:

$$\dot{\tau}^{\alpha} = \boldsymbol{s}^{\boldsymbol{e}(\boldsymbol{\alpha})}.(\boldsymbol{\tau}^{\boldsymbol{\nabla e}} + \boldsymbol{D}^{\boldsymbol{e}}\boldsymbol{\tau} - \boldsymbol{\tau}\boldsymbol{D}^{\boldsymbol{e}})\boldsymbol{m}^{\boldsymbol{e}(\boldsymbol{\alpha})}. \tag{3.36}$$

Thus, the increment in τ^{α} can be derived by using Eqs. (3.10 - 3.12) as:

$$\Delta\tau^{\alpha} = (\boldsymbol{L}:\boldsymbol{\mu}^{\boldsymbol{\alpha}} + \boldsymbol{\beta}^{\boldsymbol{\alpha}}):\boldsymbol{D}^{\boldsymbol{e}}\Delta t. \tag{3.37}$$

Similarly, the increment in non-Schmid stresses can also derived from Eq. (3.23) as:

$$\begin{aligned}
\Delta\tau_1^{\alpha} &= (\boldsymbol{L}:\boldsymbol{\mu}_{\boldsymbol{1}}^{\boldsymbol{\alpha}} + \boldsymbol{\beta}^{\boldsymbol{\alpha}}):\boldsymbol{D}^{\boldsymbol{e}}\Delta t,\\
\Delta\tau_2^{\alpha} &= (\boldsymbol{L}:\boldsymbol{\mu}_{\boldsymbol{2}}^{\boldsymbol{\alpha}} + \boldsymbol{\beta}^{\boldsymbol{\alpha}}):\boldsymbol{D}^{\boldsymbol{e}}\Delta t,\\
\Delta\tau_3^{\alpha} &= (\boldsymbol{L}:\boldsymbol{\mu}_{\boldsymbol{3}}^{\boldsymbol{\alpha}} + \boldsymbol{\beta}^{\boldsymbol{\alpha}}):\boldsymbol{D}^{\boldsymbol{e}}\Delta t,\\
\Delta\tau_4^{\alpha} &= (\boldsymbol{L}:\boldsymbol{\mu}_{\boldsymbol{4}}^{\boldsymbol{\alpha}} + \boldsymbol{\beta}^{\boldsymbol{\alpha}}):\boldsymbol{D}^{\boldsymbol{e}}\Delta t,\\
\Delta\tau_5^{\alpha} &= (\boldsymbol{L}:\boldsymbol{\mu}_{\boldsymbol{5}}^{\boldsymbol{\alpha}} + \boldsymbol{\beta}^{\boldsymbol{\alpha}}):\boldsymbol{D}^{\boldsymbol{e}}\Delta t.
\end{aligned} \tag{3.38}$$

Further, from Eq. (3.25) increment in g^{α} can be written as:

$$\Delta g^{\alpha} = \sum_{\beta=1}^{n} h_{\alpha\beta}|\Delta\gamma^{\beta}| \tag{3.39}$$

Substitution of Eqs. (3.37 - 3.39) into Eq. (3.35) leads to:

$$\begin{aligned}
\Delta\tau^{\alpha}{}_{eff} &= \left|\boldsymbol{R_{eff}}^{\boldsymbol{\alpha}}:\boldsymbol{D}^{\boldsymbol{e}}\Delta t\right| - \sum_{\beta=1}^{n} h_{\alpha\beta}\left|\Delta\gamma^{\beta}\right|\\
&= \left|\boldsymbol{R_{eff}}^{\boldsymbol{\alpha}}:\left(\boldsymbol{D}\Delta t - \sum_{\beta=1}^{n}\Delta\gamma^{\beta}\boldsymbol{\mu}^{\boldsymbol{\beta}}\right)\right| - \sum_{\beta=1}^{n} h_{\alpha\beta}\left|\Delta\gamma^{\beta}\right|,
\end{aligned} \tag{3.40}$$

where,

$$\begin{aligned}
\boldsymbol{R_{eff}}^{\boldsymbol{\alpha}} = \big[\boldsymbol{L}:\big(&\boldsymbol{\mu}^{\boldsymbol{\alpha}} + a_1\boldsymbol{\mu}^{\boldsymbol{\alpha}}{}_{\boldsymbol{1}} + a_2\boldsymbol{\mu}^{\boldsymbol{\alpha}}{}_{\boldsymbol{2}} + a_3\boldsymbol{\mu}^{\boldsymbol{\alpha}}{}_{\boldsymbol{3}} + a_4\boldsymbol{\mu}^{\boldsymbol{\alpha}}{}_{\boldsymbol{4}} + a_5\boldsymbol{\mu}^{\boldsymbol{\alpha}}{}_{\boldsymbol{5}}\big)\\
&+ (1 + a_1 + a_2 + a_3 + a_4 + a_5)\boldsymbol{\beta}^{\boldsymbol{\alpha}}\big].
\end{aligned} \tag{3.41}$$

From Eqs. (3.30)-(3.34) and Eq. (3.40), the increment in plastic slip can be determined as:

$$\Delta\gamma^{\alpha} = \dot{f}^{\alpha}\Delta t + \boldsymbol{K}^{\boldsymbol{\alpha}}:\boldsymbol{\Delta\varepsilon} + \dot{\zeta}^{\alpha}\Delta t, \tag{3.42}$$

where,

$$
\begin{aligned}
\dot{f}^{\alpha} &= \sum_{\beta=1}^{n} M_{\alpha\beta}\dot{\gamma}^{\beta}(t), \\
\boldsymbol{K^{\alpha}} &= \sum_{\beta=1}^{n} M_{\alpha\beta}\boldsymbol{Q^{\beta}}, \\
\boldsymbol{\Delta\epsilon} &= \boldsymbol{D}\Delta t, \\
M_{\alpha\beta} &= \left[N_{\alpha\beta}\right]^{-1}, \\
N_{\alpha\beta} &= \delta_{\alpha\beta} + \frac{\theta\mathcal{A}^{\alpha}\dot{\gamma}^{\alpha}(t)\Delta t}{\tau_0}\left[\boldsymbol{R_{eff}^{\alpha}}\colon \mu^{\boldsymbol{\beta}} + h_{\alpha\beta}\right], \\
\boldsymbol{Q^{\alpha}} &= \frac{\theta\mathcal{A}^{\alpha}\dot{\gamma}^{\alpha}(t)\Delta t}{\tau_0}\boldsymbol{R_{eff}}^{\boldsymbol{\alpha}}
\end{aligned}
\tag{3.43}
$$

$$
\dot{\zeta}^{\alpha} = \sum_{\beta=1}^{n} M_{\alpha\beta}\dot{\zeta}^{\beta}
$$

and,

$$
\dot{\zeta}^{\beta} = \theta\left(\frac{\Delta \mathrm{G_{k0}}}{\kappa \mathrm{T}}\right)\left(\frac{\Delta T}{T}\right)\dot{\gamma}^{\alpha}\,(t) \tag{3.44}
$$

Finally, with the help of Eq. (3.42), the constitutive law Eq. (3.17) can be derived as follows:

$$
\boldsymbol{\tau^{\nabla}} = \boldsymbol{C}\colon \boldsymbol{D} - \dot{\boldsymbol{\chi}} \tag{3.45}
$$

In the above equation, $\boldsymbol{C}$ denotes the elasto-plastic rate tangent modulus which is given by:

$$
\boldsymbol{C} = \boldsymbol{L} - \sum_{\alpha=1}^{n} \boldsymbol{R^{\alpha}} \otimes \boldsymbol{K^{\alpha}} \tag{3.46}
$$

and

$$
\dot{\boldsymbol{\chi}} \triangleq \sum_{\alpha=1}^{n} \boldsymbol{R^{\alpha}}\left(\dot{f}^{\alpha} + \dot{\zeta}^{\alpha}\right) \tag{3.47}
$$

3.3.2 Stress update algorithm

In this section, the stress update algorithm is summarized. At an integration point in an element, the following variables are known at time $t = t_n$: $\boldsymbol{F_n}^{e}, \boldsymbol{F_n}^{p}, \boldsymbol{\Delta\epsilon} = \boldsymbol{D}\Delta t$, $\boldsymbol{\tau_n}$, ${g_n}^{\alpha}$, $\boldsymbol{F_{n+1}}$, and time increment $\Delta t = t_{n+1} - t_n$. The following steps are performed to determine $\boldsymbol{F_{n+1}}^{e}, \boldsymbol{F_{n+1}}^{p}$, ${g^{\alpha}}_{n+1}$ and $\boldsymbol{\tau_{n+1}}$ at $t = t_{n+1}$.

1. Determine lattice vectors $\boldsymbol{s}^{\mathbf{e}(\alpha)}, \boldsymbol{m}^{\mathbf{e}(\alpha)}, \boldsymbol{n_1}^{\mathbf{e}(\alpha)}$, and $\boldsymbol{n_2}^{\mathbf{e}(\alpha)}$ by transforming vectors $\boldsymbol{s}^{(\alpha)}, \boldsymbol{m}^{(\alpha)}$, $\boldsymbol{n_1}^{(\alpha)}$ and $\boldsymbol{n_2}^{(\alpha)}$ from the reference configuration to the current configuration.
2. Compute the second order tensors, $\boldsymbol{\mu}^{\alpha}$ and $\boldsymbol{\omega}^{\alpha}, \boldsymbol{\beta}^{\alpha}$ and $\boldsymbol{R}^{\alpha}$.
3. Compute Schmid stress $\tau^{\alpha} = \boldsymbol{\tau_n} : \boldsymbol{\mu}^{(\alpha)}$ on each slip system.
4. Compute non-Schmid stresses for each slip system:

   ${\tau_1}^{\alpha} = \boldsymbol{\tau} : (\boldsymbol{s}^{\mathbf{e}(\alpha)} \otimes \boldsymbol{n1}^{\mathbf{e}(\alpha)})$

   ${\tau_2}^{\alpha} = \boldsymbol{\tau} : \left(\boldsymbol{s}^{\mathbf{e}(\alpha)} \otimes \boldsymbol{n2}^{\mathbf{e}(\alpha)}\right)$

   ${\tau_3}^{\alpha} = \boldsymbol{\tau} : \left((\boldsymbol{s}^{\mathbf{e}(\alpha)} \times \boldsymbol{m}^{\mathbf{e}(\alpha)}) \otimes \boldsymbol{m}^{\mathbf{e}(\alpha)}\right)$

   ${\tau_4}^{\alpha} = \boldsymbol{\tau} : \left((\boldsymbol{n1}^{\mathbf{e}(\alpha)} \times \boldsymbol{s}^{\mathbf{e}(\alpha)}) \otimes \boldsymbol{n1}^{\mathbf{e}(\alpha)}\right)$

   ${\tau_5}^{\alpha} = \boldsymbol{\tau} : \left((\boldsymbol{n_2}^{\mathbf{e}(\alpha)} \times \boldsymbol{s}^{\mathbf{e}(\alpha)}) \otimes \boldsymbol{n_2}^{\mathbf{e}(\alpha)}\right)$

5. Compute effective resolved shear stress

   ${\tau^{\alpha}}_{eff} = |\tau^{\alpha} + a_1{\tau_1}^{\alpha} + a_2{\tau_2}^{\alpha} + a_3{\tau_3}^{\alpha} + a_4{\tau_4}^{\alpha} + a_5{\tau_5}^{\alpha}| - g^{\alpha}$

6. Check for the yielding taking place in the slip system:

   If (${\tau^{\alpha}}_{eff} \leq 0$) then perform the elastic step, exit.

   Else Go to step: 7

   End If

7. Compute $\Delta {G_k}^{\alpha}$ from Eq. (3.21) and then $\dot{\gamma}^{\alpha}$ from Eq. (3.20). Also, compute $\dot{f}^{\alpha}, \boldsymbol{K}^{\boldsymbol{\alpha}}, Q^{\alpha}, \dot{\zeta}^{\alpha}$, and $N_{\alpha\beta}$ from Eqs. (3.43). Invert $N_{\alpha\beta}$. Hence compute $\Delta\gamma^{\alpha}_{n+1}$ from Eq. (3.42).
8. Update $\boldsymbol{F^{e}_{n+1}}, \boldsymbol{F^{p}_{n+1}}, \boldsymbol{\tau_{n+1}}$ and g^{α}_{n+1}

9. Calculate the elastic-plastic rate tangent modulus:

$$\boldsymbol{C} = \boldsymbol{L} - \sum_{\alpha=1}^{n} (\boldsymbol{R}^{\boldsymbol{\alpha}} \otimes \boldsymbol{K}^{\boldsymbol{\alpha}})$$

and

$$\dot{\boldsymbol{\chi}} = \sum_{\alpha=1}^{n} \boldsymbol{R}^{\boldsymbol{\alpha}} (\dot{f}^{\alpha} + \dot{\zeta}^{\alpha})$$

3.4 Finite element formulation for incremental static equilibrium

In the current work, an updated Lagrangian formulation is employed to implement the constitutive model in commercially available software Abaqus (Dassault Systèmes, 2017). To this end, a reference state is assumed to coincide instantaneously with the current configuration. Following McMeeking and Rice (1975), the variational principle is written in the current configuration in terms of the Kirchhoff stress and its Jaumann rate as:

$$\begin{aligned} \int_{\boldsymbol{V_t}} \left[\tau_{ij}^{\nabla} - (\tau_{ik} D_{kj} + D_{ik} \tau_{kj})\right] \delta D_{ij} dV + \int_{\boldsymbol{V_t}} \tau_{ij} v_{k,j} \delta v_{k,i} dV \\ = \int_{V_t} \dot{b}_j \delta v_j dV + \int_{S_T} \dot{T}_j \delta v_j dA, \end{aligned} \tag{3.48}$$

where V_t represents the volume of the body in the current configuration, while S_T denotes the part of the surface where traction is prescribed. Also, note that V_t and S_T are associated with the equilibrium configuration corresponding to time t. Further, the components of D_{ij} are given by:

$$D_{ij} = \frac{1}{2}\left(\frac{\partial v_i}{\partial \mathrm{x}_j} + \frac{\partial v_j}{\partial \mathrm{x}_\mathrm{i}}\right), \tag{3.49}$$

where, v is material point velocity. The spatial gradient of particle velocity vector is given as:

$$v_{k,i} = l_{k,i} = \frac{\partial v_k}{\partial x_i} \tag{3.50}$$

Further, $\dot{b}_j$ represent the rate of nominal body force based on the current volume and $\dot{T}_j$ denotes rate of surface traction based on the current surface area of the body. Here, it is assumed that $\dot{b}_j$ as

well as $\dot{T}_j$ are fully prescribed. Now, that the term $(\tau_{ik}D_{kj} + D_{ik}\tau_{kj})$ in Eq. (3.48) can be written as:

$$\tau_{ik}D_{kj} + D_{ik}\tau_{kj} = \hat{L}_{ijkl}D_{kl}, \tag{3.51}$$

where,

$$\hat{L}_{ijkl} = \frac{1}{2}\left(\tau_{ik}\delta_{lj} + \tau_{il}\delta_{kj} + \tau_{kj}\delta_{il} + \tau_{lj}\delta_{ik}\right). \tag{3.52}$$

It must be noted that $\hat{L}_{ijkl}$ satisfies all the major as well as minor symmetries. By using Eqs. (3.45) and (3.51), the Eq. (3.48) can be written as:

$$\begin{aligned}\int_{\boldsymbol{V_t}} \delta D_{ij}C_{ijkl}D_{kl}dV - \int_{\boldsymbol{V_t}} \delta D_{ij}\hat{L}_{ijkl}D_{kl}dV + \int_{\boldsymbol{V_t}} \tau_{ij}v_{k,j}\delta v_{k,i}dV \\ = \int_{V_t} \dot{\chi}_{ij}\delta D_{ij}\mathrm{dV} + \int_{V_t} \dot{b}_j\delta v_j dV + \int_{S_T} \dot{T}_j\delta v_j dA,\end{aligned} \tag{3.53}$$

The discretization of velocity and spatial gradient of velocity are respectively given as:

$$\begin{aligned}\{v^e\} &= [N]\{\dot{U}\}, \\ \{D^e\} &= [B]\{\dot{U}\}.\end{aligned} \tag{3.54}$$

Here, $\{\dot{U}\}$ is the vector of nodal velocity, while $[N]$ and $[B]$ are matrices of shape functions and their spatial gradients, respectively. By substituting the Eq. (3.54) into Eq. (3.53), the finite element equilibrium equations in rate form could be derived as (Bathe, 1996; Patil, 2009) as:

$$[K]^e\{\dot{U}\} = \{\dot{F}_\chi\} + \{\dot{F}_b\} + \{\dot{F}_t\}. \tag{3.55}$$

Here, $[K]^e$ is the element stiffness matrix and it is given by:

$$[K]^e = \left[K^{(1)}\right]^e - \left[K^{(2)}\right]^e + \left[K^{(3)}\right]^e. \tag{3.56}$$

Here,

$$\begin{aligned}\left[K^{(1)}\right]^e &= \int_{V_t^e} [B]^T[C][B]dV^e \\ \left[K^{(2)}\right]^e &= \int_{V_t^e} [B]^T\left[\hat{L}\right][B]\, dV^e \\ \left[K^{(3)}_{iajb}\right]^e &= \int_{V_t^e} B_l^a\tau_{lk}B_k^b\delta_{ij}\, dV^e\,,\end{aligned} \tag{3.57}$$

where $(i,j) \in [1,3]$ and $(a,b) \in [1,n_e]$ where n_e represents the number of nodes per element. Note that in the above equation, $\left[K^{(1)}\right]^e$ represents the tangent stiffness matrix resulting due to material nonlinearity, while $\left[K^{(2)}\right]^e$ and $\left[K^{(3)}\right]^e$ comprise the initial stress stiffness. Also, the matric $[C]$ in Eq. (3.57a) contains the fourth order tensor C_{ijkl} which satisfies the major symmetry (see, Eq. (3.46), consequently the matric $[C]$ and hence $\left[K^{(1)}\right]^e$ are symmetric. Further, the matrix $\left[\hat{L}\right]$ appearing in the definition of $\left[K^{(2)}\right]^e$ contains the tensor $\hat{L}_{ijkl}$. The element force vectors, $\left\{\dot{F}_\chi\right\}^e$, $\left\{\dot{F}_b\right\}^e$ and $\left\{\dot{F}_t\right\}^e$ in Eq. (3.55) are respectively given by:

$$\left\{\dot{F}_\chi\right\}^e = \int_{V_t^e} [B]^T \{\dot{\chi}\} dV^e, \tag{3.58}$$

$$\left\{\dot{F}_b\right\}^e = \int_{V_t^e} [N]^T \{\dot{b}\} dV^e, \tag{3.59}$$

$$\left\{\dot{F}_t\right\}^e = \int_{S_t^e} [N]^T \{\dot{T}\} dA, \tag{3.60}$$

Here, $\left\{\dot{F}_\chi\right\}^e$ indicates the rate of nodal vector force due to the term $\boldsymbol{\chi}^{\cdot}$ in Eq. (3.53), while $\left\{\dot{F}_t\right\}^e$, $\left\{\dot{F}_b\right\}^e$ are rate of nodal force vectors due to surface tractions and body force, respectively.

The finite element formulation presented in this section has been implemented in the commercially available software package ABAQUS/Standard (6.17) by writing a user element subroutine (UEL) for eight-noded isoparametric hexahedral elements. The $\bar{B}$ –formulation (Moran et al., 1990) has been used to alleviate mesh locking due to nearly incompressible plastic deformation.

3.5 Determination of Material parameters for molybdenum single crystal

In this section, material parameters appearing in the crystal plasticity model discussed in the previous section are determined for a Mo single crystal. The elastic constants C_{11}, C_{12} and C_{44} are assumed to be independent of temperature and taken as 469.0×10^3, 167.6×10^3 and 106.8×10^3 MPa, respectively, from the work of Bolef and Klerk (1998). Note that g_o^α and τ_o can be considered as the material resistance for plastic yielding at high temperature and at 0 K, respectively. Therefore, the values of g_o^α and τ_o are taken as 6 and 665 MPa corresponding to the

resolved shear stresses at 450 and 0 K, respectively (Kaufmann et al. (1984)). Note that g_o^α are taken identical for all slip systems. Further, considering $\Delta G_k/\kappa T \approx 25$ (Hollang et al. (1997)), Eqs. (3.21) and (3.22) gives the resolved shear stress as:

$$\tau^{e(\alpha)} = g_o^\alpha + \tau_0 \left[1 - \left(\frac{25\kappa T}{\Delta G_{k0}}\right)^{\frac{1}{q}}\right]^{\frac{1}{p}}. \tag{3.61}$$

By fitting the above expression to the experimental data reported by Kaufmann et al. (1984), the values of parameters ΔG_{k0}, p and q are determined as 0.16568×10^{-18} J, 0.5 and 1.25, respectively.

The parameters $a_1 - a_5$, ${h_0}^\alpha$, ${h_s}^\alpha$, and ${g_s}^\alpha$ are determined by simultaneously fitting stress-strain curves obtained from FE simulations of tensile loading along [100], [110] and [111] directions to the corresponding experimental data. For this purpose, genetic algorithm (GA) implemented in MATLAB (2020) is utilized. The following objective function, χ^2 is employed to minimize the error between simulated and experimental data:

$$\Psi^2 = \frac{1}{3}\left(\Psi^2_{[100]} + \Psi^2_{[110]} + \Psi^2_{[111]}\right) = \frac{1}{3}\sum_{orientation}\left(\sum_1^m \frac{\left(\sigma_{(exp,\ \epsilon)} - \sigma_{(sim,\ \epsilon)}\right)^2}{m}\right). \tag{3.62}$$

Here, $\sigma_{(exp,\ \epsilon)}$ and $\sigma_{(sim,\ \epsilon)}$ represent stress values at strain ϵ for a given orientation obtained from experiments and simulations, respectively. The parameter m denote the number of data points on the stress-strain curves. The experimental data for orientation [111] are taken from the work of Irwin et al. (1974) is used, and for the orientation [100] and [110], the data reported by Kopetskii and Pashkovskii (1974) are used. In order to compute simulated data (i.e., $\sigma_{(sim,\ \epsilon)}$), ABAQUS is launched from MATLAB to run FE simulations. It must be mentioned that these simulations are performed using single element so that the time required in optimization can be reduced. The eight-node brick element along with the prescribed boundary conditions employed in these simulations is displayed in Figure 3.2. Simulations for all three orientation are conducted at room temperature. Further, following the Irwin et al. (1974), the simulations on (111) oriented crystal are performed with strain rate of $6.0 \times 10^{-5}\ s^{-1}$. However, the strain rate of $1.0^{-4}\ s^{-1}$ is used in the simulations of loading along [100], [101] directions, which is identical to that used in experiments of Kopetskii and Pashkovskii (1974). The values of parameters optimized by GA are

listed in Table 3.3. Figure 3.3 shows the comparison between simulated and experimental stress versus strain curves for loading along different orientation. It can be seen from this figures that simulated curves matches reasonably well with the experimental data for all three orientations. It should be mentioned that the values of some of the parameters ($a_1 - a_5$, g_s^α, h_o^α and h_s^α) obtained

Table 3.3: The values of non-Schmid coefficients and parameters appearing in the hardening model for single crystal Mo.

a_1	0.21		
a_2	0.20		
a_3	0.44		
a_4	0.24		
a_5	0.23		
	$< 111 > \{110\}$	$< 111 > \{112\}$ Antitwinning sense	$< 111 > \{112\}$ Twinning sense
${g_0}^\alpha$	6.0	6.0	6.0
${g_s}^\alpha$	22.6	22.0	136.5
${h_0}^\alpha$	1919.4	3299.0	1820.0
${h_s}^\alpha$	25.0	40.0	31.0

from the optimization in the present study differ from that reported by Daphalapurkar et al. (2018). This could be due the fact that g_o^α = 2 MPa was considered to determine the parameters by Daphalapurkar et al. (2018), whereas, g_o^α = 6 MPa is used in the present optimization.

3.5.1 Validation of material Parameters for Mo Crystal

To validate the material parameters obtained in the previous section, finite element simulations of tension test at different temperature and compression test at room temperature are performed and the simulated curves are compared with the corresponding experimental data. The tension simulations are performed on [101] oriented crystal by considering the various values of T = 223, 293, 353 and 423 K. Figure 3.4 shows the comparaison of the simulated stress versus strain curves along with the experimental data reported by Kopetskii and Pashkovskii (1974). Note from this

figure that the present simulations predict temperature dependent yield strength of [101] oriented Mo crystal reasonably well, except for the case of very low temperature of 223K. However, the hardening response is well captured from FE simulations for all values of T. Figure 3.5 contrasts the compressive response of a [111] oriented Mo crystal predicted by FE simulations and the experimental data of Irwin et al. (1974). This figure also show good agreement between simulations and experiments.

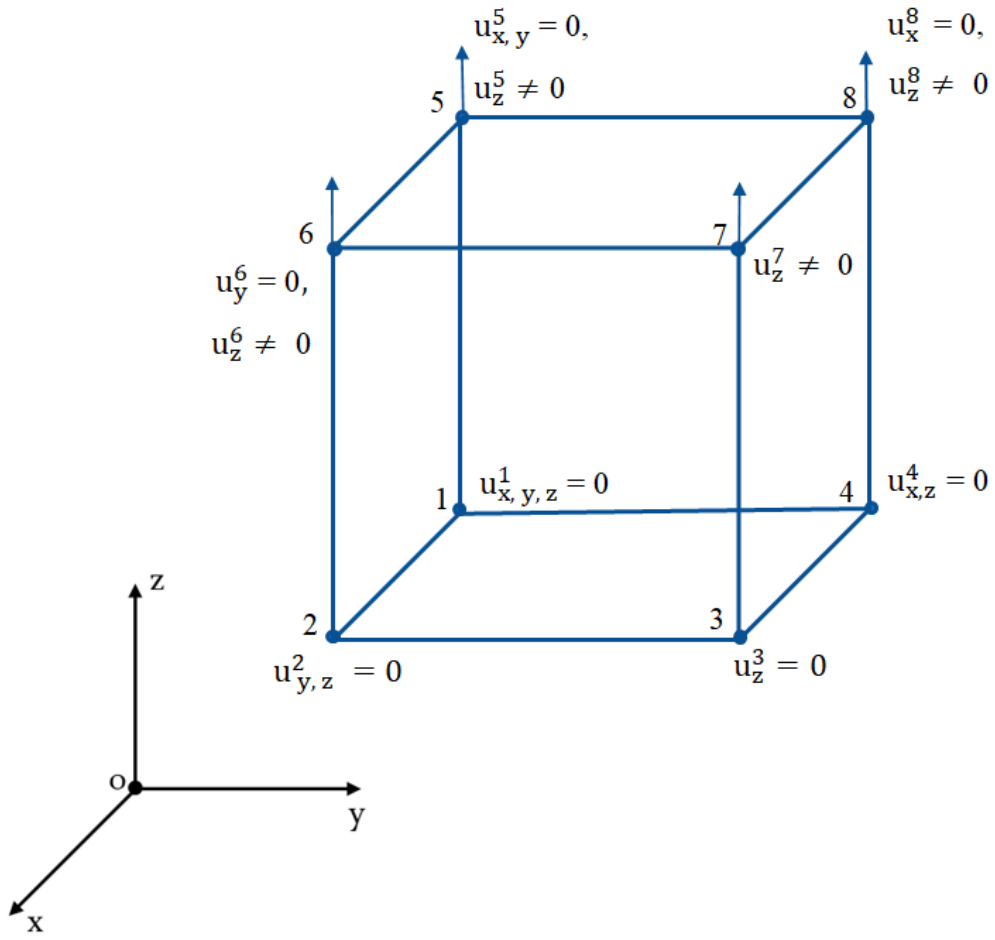

Figure 3.2: A single 8-node brick element and the applied boundary conditions employed in the finite element simulations.

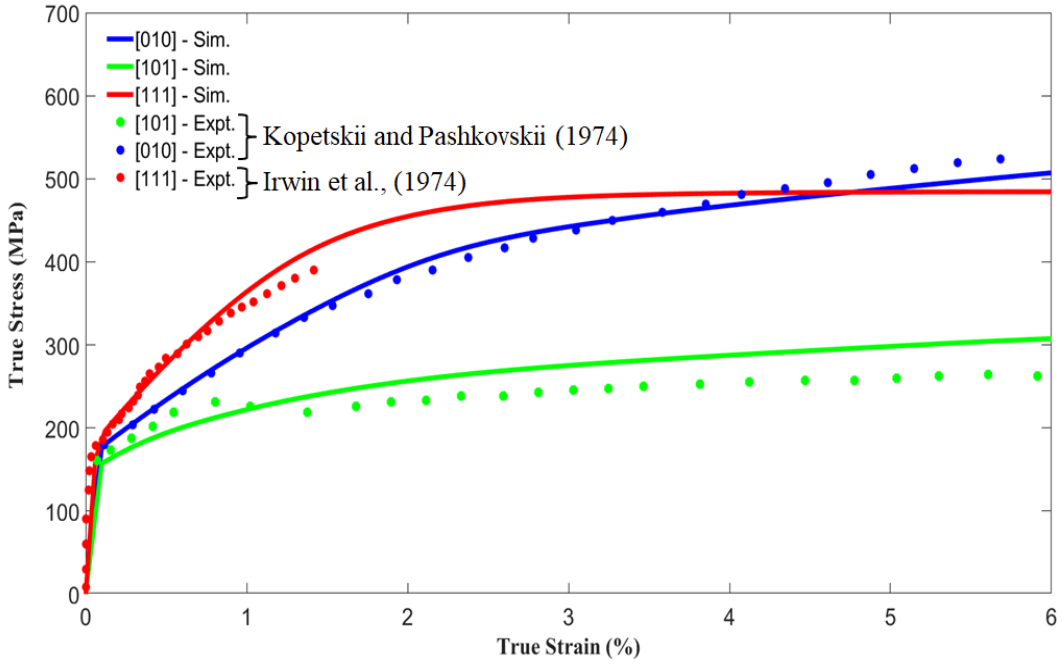

Figure 3.3: True stress versus true strain curves for tensile loading along [010], [101], and [111] direction in a Mo single crystals obtained from present finite element simulations and the experiments of Irwin et al. (1974) and Kopetskii and Pashkovskii (1974).

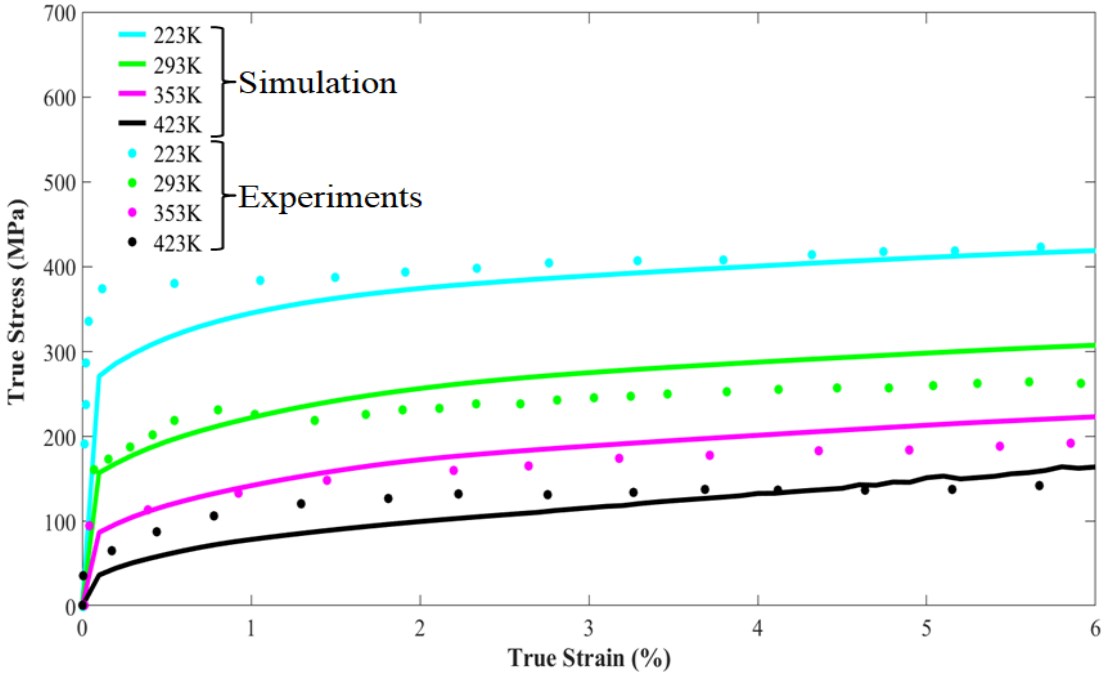

Figure 3.4: True stress versus true strain curves for tensile loading along [101] direction in Mo single crystals obtained from present finite element simulations and the experiments performed at different temperature by Kopetskii and Pashkovskii (1974).

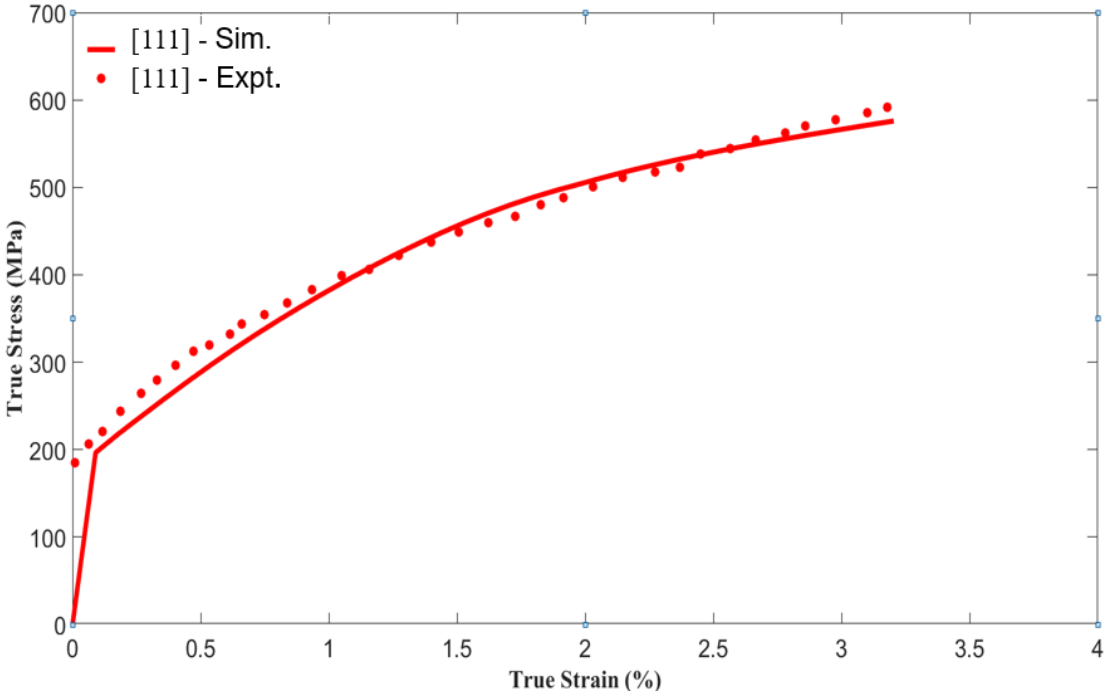

Figure 3.5: True stress versus true strain curves for compressive loading along [111] direction on a Mo crystal obtained from the present simulations and experiments of Irwin et al. (1974).

3.6 Summary

In this chapter, the crystal plasticity model proposed by Daphalapurkar et al. (2018) has been presented briefly. In addition, a numerical algorithm employing the rate tangent formulation is derived to update the stress and the history variables in the model. Further, the finite element procedure to implement the crystal plasticity model into a commercial finite element code ABAQUS/Standard (6.17) by writing user-element subroutine (UEL) is described. Finally, the values of material parameters are obtained for Mo single crystal.

Chapter 4

Conclusion and Future work

4.1 Conclusions

The important conclusions from the work reported in Chapter 2 and 3 are summarized in this Chapter. In Chapter 2, the nano- and micro-indentation experiments are performed on (100)-, (110)- and (111)-oriented Mo single crystal. The piling-up patterns are analyzed by using AFM. In Chapter 3, crystal plasticity model proposed by Daphalpurkar et al. (2018) and its numerical implementation in Abaqus (6.17) is presented. The important conclusions from this thesis are as follows:

1) The nano-indentation experiments showed that the indentation depth at peak load, P_{max} was maximum for (100), least for (110) while intermittent for (111) orientation suggesting (110) orientation offers the highest resistance to plastic deformation. The amount of elastic recovery has also shown similar trend with respect to crystallographic orientation. Thus, the (100) orientation has the least elastic modulus and (110) has the highest modulus.
2) The values of the elastic modulus obtained from nanoindentation experiments for (100), (110), and (111) Mo single crystals are 235 ± 12, 275 ± 15 and 210 ± 10 GPa, respectively.
3) For all the orientation, the nano-hardness, H_n decreases with increasing P_{max} showing indentation size effect. Further, at any given P_{max}, hardness of (110) orientation is the highest while (100) is the lowest. Moreover, the difference in hardness (ΔH) between (110) and (100) orientations is significant at lower load which decreases with increasing P_{max}.
4) AFM scan of indent impression created through nano-indentation showed significant pile-up on (100), and (110) surfaces, but for (111) oriented crystal no significant pile-up was observed. The impression size for (100) orientation is larger, (110) orientation is smaller while for (111) orientation is in intermediate. Therefore, it is concluded that the hardness anisotropy can also be correlated with impression size.

5) The calculations of Schmid factor using the model of Raineesh et al. (2021) suggest that the slip occurs on both {110}<111> and {112}<111> slip systems in all three orientations under Berkovich indentation. Further, {112}<111> slip system must be activated for (110) orientation, while it need not get activated for other two orientations. Since the critical resolved shear stress (CRSS) is more for {112}<111> than that for {110}<111> slip systems, therefore (110) is the hardest plane at lower depths.
6) The micro-hardness H_m is found to be lower than H_n which is attributed to the larger strain gradients during nanoindentation in contrast to the micro-indentation. Further, H_m also decreases with increasing indentation load up to 1000 mN. In the case of micro-indentation also, the highest hardness is observed on (110) surface. As the applied indentation load during micro-indentation increases, the difference in hardness between the three samples decreases and saturation in hardness is observed.
7) Pile-ups patterns produced through micro-indentation on the surfaces of (100), (110), and (111) oriented Mo single crystals have shown four-, two-, and three-fold symmetry, respectively.
8) The parameter h^* appearing in the model of Nix and Gao (1998) is found to vary in nano and micron scale. The analytically predicted values of h^* agree well with the experimentally determined values. The nanoscale and microscale intrinsic material length, $\hat{l}_{nano}$ and $\hat{l}_{micro}$ marginally depend on crystal orientation and are found to be around 0.55-0.65 and 10.89-12.45, respectively.
9) The crystal plasticity model proposed by Daphalpurkar et al. (2018) is implemented in commercially available software package Abaqus (6.17) by writing user element (UEL) subroutine. The performance of the developed element is benchmarked by comparing the simulated stress-strain curves for tensile and compressive loadings with the corresponding experimental data reported by Irwin et al. (1974) and Kopetskii and Pashkovskii (1974).

4.2 Future Work

The following studies can be undertaken based on the insights gained from the present work.

1) The finite element simulations of indentation on Mo single crystals oriented along (100), (110) and (111) directions can be performed to understand the various active slip systems during indentation and their influence on the plastic deformation below the indenter.
2) Indentation experiments can be carried out by changing the azimuthal orientations of the pyramidal indenter to understand the effect of indenter-orientation on the pile-up patterns.
3) The crystal plasticity model can be modified by introducing intrinsic material length scale parameter to understand the indentation size effect better.

APPENDIX-A

Schmid factor calculation procedure

To compute the Schmid factor under Berkovich indentation, it is assumed the load is being transmitted to the material along the apex of the tip (the apex of the tip is almost spherical) (Schuh, 2006) and normal to the slanting faces of the indenter following the model proposed by Raineesh et al. (2021). The compressive forces acting normal to the slanting faces of the Berkovich indenter are 120° apart. The schematic of Berkovich indenter is shown in Figure A-1 with the direction of indentation ID. Consider N1, N2, N3 to be loading directions perpendicular to the three faces of Berkovich indenter, with N1, N2 visible perpendicular to faces OPQ and OPR in Figure A-1. The indenter can be oriented in variety of ways with respect to sample as depicted in Figure A-2(a)-(b). Initially, the indenter is placed such that the edge PQ of indenter lies parallel to y-axis and line OS on indenter face OPQ lies on xz-plane as shown in Figure 2(b) which is taken as reference and corresponds to zero degree rotation of indenter about the x-axis as shown in Figure A-2(c). For calculation of Schmid factor for BCC {110}<111> and {112}<111> families of slip system were considered. To begin the calculation of Schmid factor along the slant face of indenter for (100) oriented Mo single crystal the orientation of crystal is assumed such that [100]-, [010]-, [001]-directions are along x-, y-, z-axes as shown in Figure A-3. Thus the unit normal vector, n_1 which is parallel to the loading direction N1 of the indenter face OPQ (refer Figure 3) is given as follows:

$$n_1 = [-\cos(24.7^0)\ \ 0\ \ \cos(65.3^0)]. \tag{1}$$

For different orientation of intender the unit normal vector along the loading direction N1 (i.e. normal to the indenter face OPQ), is given by:

$$n_1' = R_x(\theta) \times n_1 \tag{2}$$

where the unit normal vector n_1' along the loading direction N1 is a function of rotation angle, θ and $R_x(\theta)$ is the rotation matrix about x-axis which is given as:

$$R_x(\theta) = \begin{bmatrix} 1 & 0 & 0 \\ 0 & \cos(\theta) & -\sin(\theta) \\ 0 & \sin(\theta) & \cos(\theta) \end{bmatrix} \tag{3}$$

Now, the direction cosines of slip plane normal (n_p) and slip direction (n_d) in sample coordinate system are given as follows:

$$n_p = [\cos(\alpha_p)\ \ \cos(\beta_p)\ \ \cos(\gamma_p)],$$
$$n_d = [\cos(\alpha_d)\ \cos(\beta_d)\ \ \cos(\gamma_d)] \quad (4)$$

where α_p, β_p, γ_p are the angles between slip plane normal and the x-, y- and z-axes lying along [100]-, [010]-, and [001]-directions and $\alpha_d, \beta_d, \gamma_d$ are the angles between slip direction and x-, y-, and z-axes along [100]-, [010]-, and [001]-directions, respectively. Crystallographic calculations can be used to calculate the direction cosines.

Consider the case for (100) oriented crystal; direction cosines for (110)[$1\bar{1}1$] slip system in sample coordinate system can be obtained as follows:

$$\cos(\alpha_p) = \frac{(1\times1 + 1\times0 + 0\times0)}{(|(110)|\times|(100)|)};\quad \cos(\beta_p) = \frac{(1\times0 + 1\times1 + 0\times0)}{(|(110)|\times|(010)|)};\quad \cos(\gamma_p) = \frac{(1\times0 + 1\times0 + 0\times1)}{(|(110)|\times|(001)|)}$$
$$\cos(\alpha_d) = \frac{(1\times1 + (-1)\times0 + 1\times0)}{(|(1\bar{1}1)|\times|(100)|)};\ \cos(\beta_p) = \frac{(1\times0 + (-1)\times1 + 1\times0)}{(|(1\bar{1}1)|\times|(010)|)};\ \cos(\gamma_p) = \frac{(1\times0 + (-1)\times0 + 1\times1)}{(|(1\bar{1}1)|\times|(001)|)} \quad (5)$$

Similarly direction cosines can be calculated for other slip systems and also for (110), and (111) oriented crystals.

The Schmid factor (SF) is computed as follows:

$$SF_{N_1}^{\theta} = |(n_1'.n_p) \times (n_1'.n_d)|. \quad (6)$$

From Eq. (6) it can be noticed that the Schmid factor is a function of in-plane rotation angle, θ. Similarly, compressive forces also acts along the normals of other two faces of Berkovich indenter which are separated by 120^0 and 240^0, respectively and Schmid factor corresponding to other two faces can be determined as $SF_{N_2}^{\theta} = SF_{N_1}^{\theta+240^0}$ and $SF_{N_3}^{\theta} = SF_{N_1}^{\theta+120^0}$. Schmid factor directly beneath the indenter is calculated similarly to the uniaxial compression test.

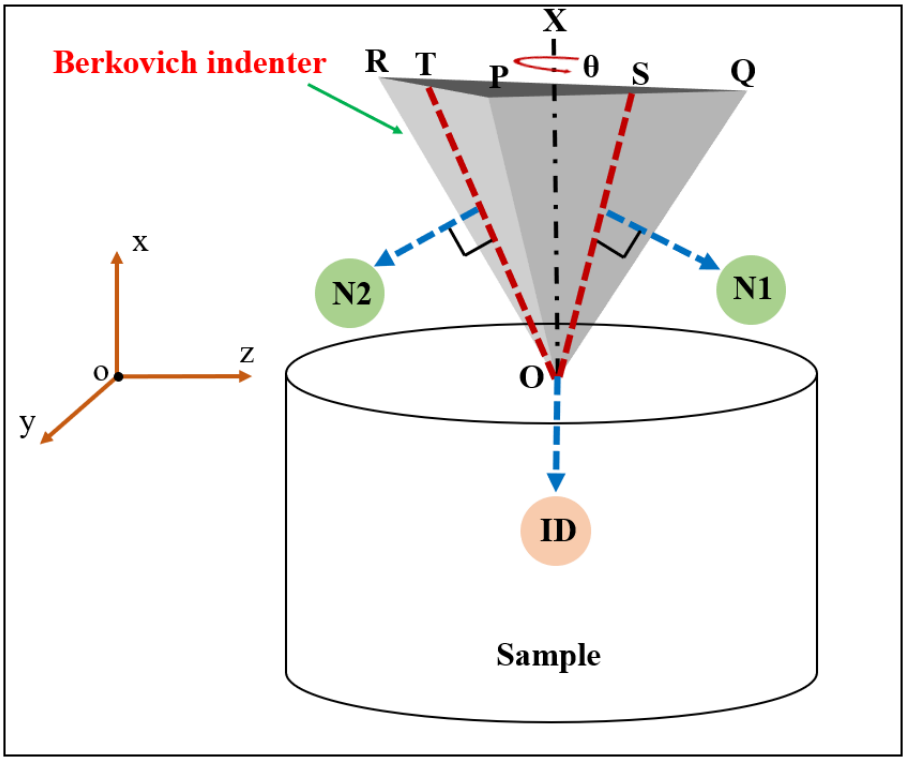

Figure A-1: Schematic showing the pyramidal geometry of the Berkovich indenter, as well as the loading directions N1, N2, N3 normal to the three faces of the Berkovich indenter and the indentation direction (ID) at the apex of the indenter.

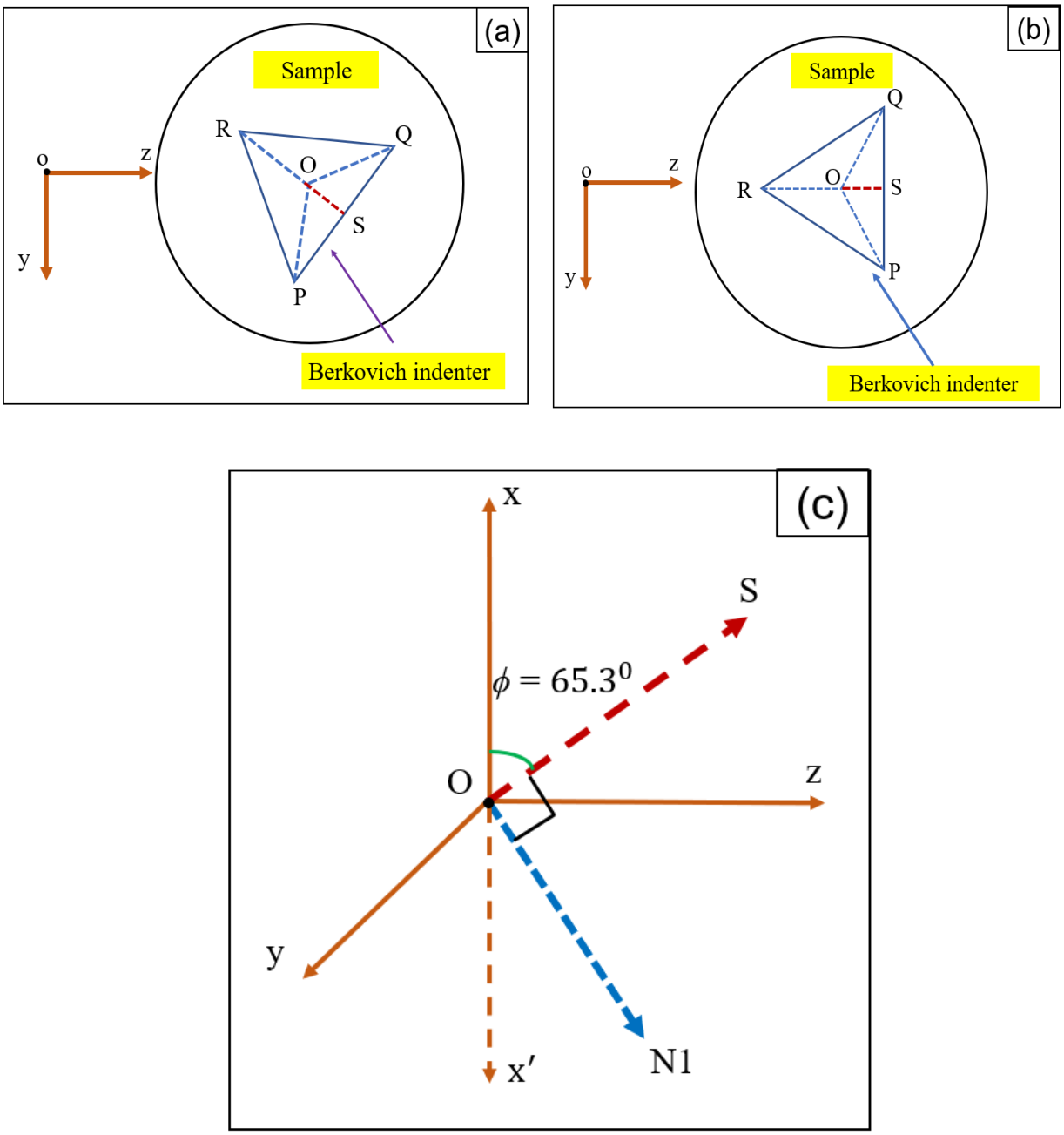

Figure A-2: (a)-(b) Schematic representation of inplane orientation of indenter; c) 2D-representation of loading direction (ON1) and line (OS) on indenter face OPQ.

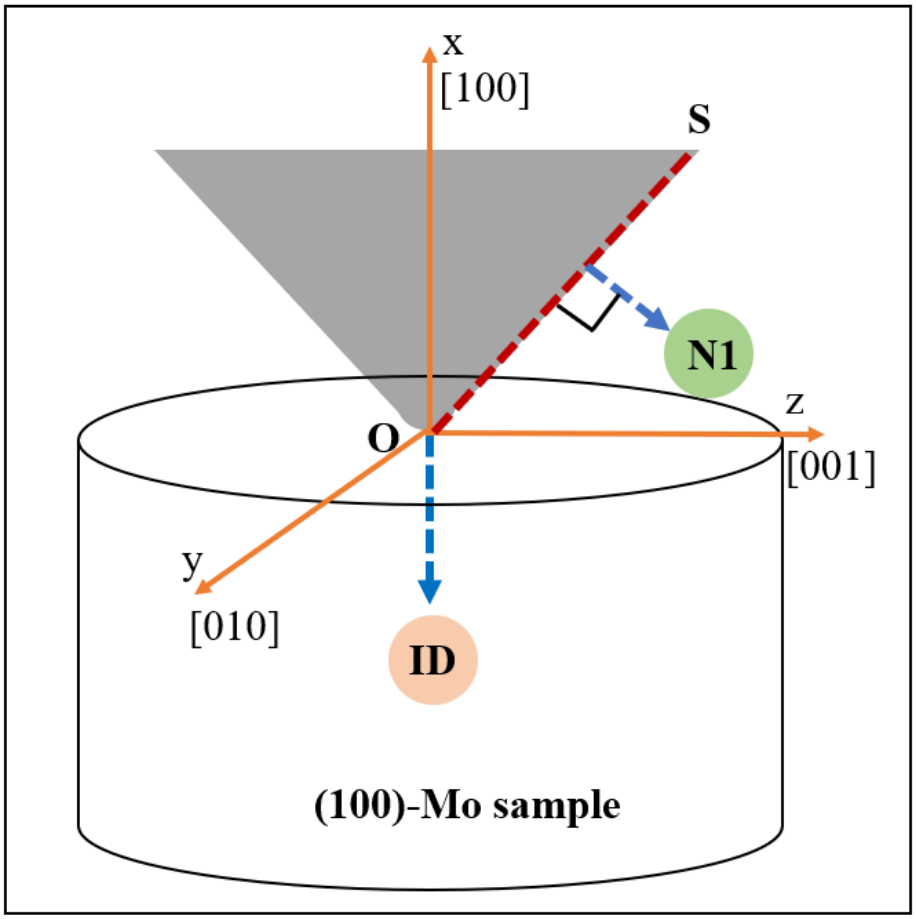

Figure A-3: Schematic showing assumed in plane orientation for (100) oriented Mo crystal for Schmid factor calculation.

REFERENCES

[1] Alcalá, J., Dalmau, R., Franke, O., Biener, M., Biener, J., Hodge, A., 2012. Planar defect nucleation and annihilation mechanisms in nanocontact plasticity of metal surfaces. Phys. Rev. Lett. 109, 17–21. https://doi.org/10.1103/PhysRevLett.109.075502

[2] Ao, Z.M., Li, S., Jiang, Q., 2008. The determination of Young's modulus in noble metal nanowires. Appl. Phys. Lett. 93, 2006–2009. https://doi.org/10.1063/1.2976134

[3] Asaro, R.J., 1983. Crystal plasticity, J. Appl. Mech. 50,921–934. https://doi.org/10.1115/1.3167205

[4] Asaro, R.J., Rice, J.R., 1977. Strain localization in ductile single crystals. J. Mech. Phys. Solids 25, 309–338. https://doi.org/10.1016/0022-5096(77)90001-1

[5] Asaro, R.J., Needleman, A., 1985. Overview no. 42 Texture development and strain hardening in rate dependent polycrystals. Acta Metall. 33, 923–953. https://doi.org/10.1016/0001-6160(85)90188-9

[6] Bahr, D.F., Kramer, D.E., Gerberich, W.W., 1998. Non-linear deformation mechanisms during nanoindentation. Acta Mater. 46, 3605–3617. https://doi.org/10.1016/S1359-6454(98)00024-X

[7] Bassani, J.L., Wu, T., A, P.R.S.L., 1991. Latent hardening in single crystals. II. Analytical characterization and predictions. Proc. R. Soc. London. Ser. A Math. Phys. Sci. 435, 21–41. https://doi.org/10.1098/rspa.1991.0128

[8] Bathe, K.J., Finite Element Procedures, PRH, USA, 1996.

[9] Bassani, J.L., Ito, K., Vitek, V., 2001. Complex macroscopic plastic flow arising from non-planar dislocation core structures. Mater. Sci. Eng. A 319–321, 97–101. https://doi.org/10.1016/S0921-5093(00)02008-6

[10] Bei, H., Gao, Y.F., Shim, S., George, E.P., Pharr, G.M., 2008. Strength differences arising from homogeneous versus heterogeneous dislocation nucleation. Phys. Rev. B - Condens. Matter Mater. Phys. 77, 2–5. https://doi.org/10.1103/PhysRevB.77.060103

[11] Biener, M.M., Biener, J., Hodge, A.M., Hamza, A. V., 2007. Dislocation nucleation in bcc Ta single crystals studied by nanoindentation. Phys. Rev. B – Condens. Matter Mater. Phys. 76, 1–6. https://doi.org/10.1103/PhysRevB.76.165422

[12] Bolef, D.I., De Klerk, J., 1962. Elastic Constants of Single-Crystal Mo and W between 77°and 500°K. J. Appl. Phys. 33, 2311–2314. https://doi.org/10.1063/1.1728952

[13] Brinckmann, S., Kim, J.Y., Greer, J.R., 2008. Fundamental differences in mechanical behavior between two types of crystals at the nanoscale. Phys. Rev. Lett. 100, 1–4. https://doi.org/10.1103/PhysRevLett.100.155502

[14] Čech, J., Haušild, P., Materna, A., 2018. Effect of crystallographic orientation on nanoindentation response of Fe3Si single-crystals. Key Eng. Mater. 784 KEM, 44–48. https://doi.org/10.4028/www.scientific.net/KEM.784.44

[15] Chicot, D., 2009. Hardness length-scale factor to model nano- and micro-indentation size effects. Mater. Sci. Eng. A 499, 454–461. https://doi.org/10.1016/j.msea.2008.09.040

[16] Clayton, J.D., 2019. Nonlinear Elastic and Inelastic Models for Shock Compression of Crystalline Solids, Shock Wave and High Pressure Phenomena.

[17] Csanádi, T., Bl'Anda, M., Chinh, N.Q., Hvizdoš, P., Dusza, J., 2015. Orientation-dependent hardness and nanoindentation-induced deformation mechanisms of WC crystals. Acta Mater. 83, 397–407. https://doi.org/10.1016/j.actamat.2014.09.048

[18] Dassault Systèmes 2017 Abaqus User Subroutines Reference Manual Version 6.17. Dassault Systèmes, 2017

[19] Das, S., Yu, H., Tarleton, E., Hofmann, F., 2019. Orientation-dependent indentation response of helium-implanted tungsten. Appl. Phys. Lett. 114, 221905. https://doi.org/10.1063/1.5097403

[20] Daphalapurkar, N.P., Patil, S., Nguyen, T., Prasad, K.E., Ramesh, K.T., 2018. A crystal plasticity model for body-centered cubic molybdenum: Experiments and simulations. Mater. Sci. Eng. A 738, 283–294. https://doi.org/10.1016/j.msea.2018.09.099

[21] Demiral, M., Roy, A., Silberschmidt, V. V., 2013. Indentation studies in b.c.c. crystals with enhanced model of strain-gradient crystal plasticity. Comput. Mater. Sci. 79, 896–902. https://doi.org/10.1016/j.commatsci.2013.06.057

[22] Dieter, G.E., 1988, Mechanical Metallurgy, McGraw-Hill Book Company-London, pp.45-46

[23] Eliash, T., Kazakevich, M., Semenov, V.N., Rabkin, E., 2008. Nanohardness of molybdenum in the vicinity of grain boundaries and triple junctions. Acta Mater. 56, 5640–5652. https://doi.org/10.1016/j.actamat.2008.07.036

[24] Filippov, P., Koch, U., 2019. Nanoindentation of aluminum single crystals: Experimental study on influencing factors. Materials (Basel). 12, 1–16. https://doi.org/10.3390/ma12223688

[25] Franke, O., Alcalá, J., Dalmau, R., Duan, Z.C., Biener, J., Biener, M.M., Hodge, A.M., 2015. Incipient plasticity of single-crystal tantalum as a function of temperature and orientation. Philos. Mag. 95, 1866–1877. https://doi.org/10.1080/14786435.2014.949324

[26] Frost, H. J. and Ashby, M. F. (1982) Deformation Mechanism Maps. Pergamon Press, New York.

[27] Ganapathysubramanian, S., Zabaras, N., 2005. Modeling the thermoelastic-viscoplastic response of polycrystals using a continuum representation over the orientation space. Int. J. Plast. 21, 119–144. https://doi.org/10.1016/j.ijplas.2004.04.005

[28] Goel, S., Beake, B., Chan, C.W., Haque Faisal, N., Dunne, N., 2015. Twinning anisotropy of tantalum during nanoindentation, Materials Science and Engineering A. https://doi.org/10.1016/j.msea.2014.12.075

[29] Gröger, R., Racherla, V., Bassani, J.L., Vitek, V., 2008. Multiscale modeling of plastic deformation of molybdenum and tungsten: II. Yield criterion for single crystals based on atomistic studies of glide of 1/2<111> screw dislocations. Acta Mater. 56, 5412–5425. https://doi.org/10.1016/j.actamat.2008.07.037

[30] Guiu, F., Pratt, P.L., 1966. The Effect of Orientation on the Yielding and Flow of Molybdenum Single Crystals. Phys. Status Solidi 15, 539–552. https://doi.org/10.1002/pssb.19660150214

[31] Haghshenas, M., Klassen, R.J., Liu, S.F., 2017. Depth-sensing cyclic nanoindentation of tantalum. Int. J. Refract. Met. Hard Mater. 66, 144–149. https://doi.org/10.1016/j.ijrmhm.2017.03.015

[32] Hertz, H., Hertz's miscellaneous papers; Ch. 5 and 6., Macmillan, London, U.K., 1896

[33] Hill, R., 1966. Generalized constitutive relations for incremental deformation of metal crystals by multislip. J. Mech. Phys. Solids 14, 95–102. https://doi.org/10.1016/0022-5096(66)90040-8

[34] Hosford, William F. Mechanical Behavior of Materials. Cambridge; New York :Cambridge University Press, 2010.

[35] Hu, J., Sun, W., Jiang, Z., Zhang, W., Lu, J., Huo, W., Zhang, Y., Zhang, P., 2017. Indentation size effect on hardness in the body-centered cubic coarse-grained and nanocrystalline tantalum. Mater. Sci. Eng. A 686, 19–25. https://doi.org/10.1016/j.msea.2017.01.033

[36] Hull, D., Bacon, D. J., 2011. Introduction to dislocations (5th ed.). Butterworth-Heinemann.

[37] Hutchinson, J.W., A, P.R.S.L., 1976. Bounds and self-consistent estimates for creep of polycrystalline materials. Proc. R. Soc. London. A. Math. Phys. Sci. 348, 101–127. https://doi.org/10.1098/rspa.1976.0027

[38] Irwin, G.J., Guiu, F., Pratt, P.L., 1974. The influence of orientation on slip and strain hardening of molybdenum single crystals. Phys. Status Solidi 22, 685–698. https://doi.org/10.1002/pssa.2210220236

[39] Javaid, F., Xu, Y., Bruder, E., Durst, K., 2018. Indentation size effect in tungsten: Quantification of geometrically necessary dislocations underneath the indentations using HR-EBSD. Mater. Charact. 142, 39–42. https://doi.org/10.1016/j.matchar.2018.05.016

[40] Kaufmann, H. -J, Luft, A., Schulze, D., 1984. Deformation mechanism and dislocation structure of high-purity molybdenum single crystals at low temperatures. Cryst. Res. Technol. 19, 357–372. https://doi.org/10.1002/crat.2170190312

[41] Kim, J.Y., Greer, J.R., 2008. Size-dependent mechanical properties of molybdenum nanopillars. Appl. Phys. Lett. 93, 1–3. https://doi.org/10.1063/1.2979684

[42] Kim, J.Y., Greer, J.R., 2009. Tensile and compressive behavior of gold and molybdenum single crystals at the nano-scale. Acta Mater. 57, 5245–5253. https://doi.org/10.1016/j.actamat.2009.07.027

[43] Kocks, U. F., Argon, A. S. and Ashby, M. F. (1975) Thermodynamics and kinetics of slip. Prog. Mater. Sci. 19, 141-145.

[44] Kopetskii, C. V., Pashkovskii, A.I., 1974. Plastic deformation and dislocation structure of molybdenum single crystals upon extending along 〈110〉 and 〈100〉 axes in the range from 77 to 573 °K. Phys. Status Solidi 21, 741–751. https://doi.org/10.1002/pssa.2210210241

[45] Kothari, M., Anand, L., 1998. Elasto-viscoplastic constitutive equations for polycrystalline metals: Application to tantalum. J. Mech. Phys. Solids 46, 51–67. https://doi.org/10.1016/S0022-5096(97)00037-9

[46] Lawley, A., Gaigher, H.L., 1964. Deformation structures in zone-melted molybdenum. Philos. Mag. 10, 15–33. https://doi.org/10.1080/14786436408224204

[47] Lee, E.H., 1969. Elastic-plastic deformation at finite strains. J. Appl. Mech. Trans. ASME 36, 1–6. https://doi.org/10.1115/1.3564580

[48] Lee, Y.J., Subhash, G., Ravichandran, G., 1999. Constitutive modeling of textured body-centered-cubic (bcc) polycrystals. Int. J. Plast. 15, 625–645. https://doi.org/10.1016/S0749-6419(99)00004-2

[49] Lee, Y.H., Hahn, J.H., Nahm, S.H., Jang, J.I., Kwon, D., 2008. Investigations on indentation size effects using a pile-up corrected hardness. J. Phys. D. Appl. Phys. 41. https://doi.org/10.1088/0022-3727/41/7/074027

[50] Lee, S.W., Meza, L., Greer, J.R., 2013. Cryogenic nanoindentation size effect in [0 0 1]-oriented face-centered cubic and body-centered cubic single crystals. Appl. Phys. Lett. 103, 1–6. https://doi.org/10.1063/1.4820585

[51] Li, H., Bradt, R.C., 1993. The microhardness indentation load/size effect in rutile and cassiterite single crystals. J. Mater. Sci. 28, 917–926. https://doi.org/10.1007/BF00400874

[52] Liao, K.C., Friedman, P.A., Pan, J., Tang, S.C., 1998. Texture development and plastic anisotropy of B.C.C. Strain hardening sheet metals. Int. J. Solids Struct. 35, 5205–5236. https://doi.org/10.1016/S0020-7683(97)00265-5

[53] Liu, Y., Varghese, S., Ma, J., Yoshino, M., Lu, H., Komanduri, R., 2008. Orientation effects in nanoindentation of single crystal copper. Int. J. Plast. 24, 1990–2015. https://doi.org/10.1016/j.ijplas.2008.02.009

[54] Lunk, H.J., Hartl, H., 2017. Discovery, properties and applications of molybdenum and its compounds. ChemTexts 3, 1–23. https://doi.org/10.1007/s40828-017-0048-6

[55] MaTecK Germany, https://mateck.com/info/molybdenum-single-crystal-42mo95-94.html

[56] Matlab. User's Guide and Optimization Toolbox User's Guide; Math Works: Natick, MA, USA, 2020.

[57] McMeeking, R.M., Rice, J.R., 1975. Finite-element formulations for problems of large elastic-plastic deformation. Int. J. Solids Struct. 11, 601–616. https://doi.org/10.1016/0020-7683(75)90033-5

[58] Moran, B., Ortiz, M., Shih, C.F., 1990. Formulation of implicit finite element methods for multiplicative finite deformation plasticity. Int. J. Numer. Methods Eng. 29, 483–514. https://doi.org/10.1002/nme.1620290304

[59] Morris, J.R., Bei, H., Pharr, G.M., George, E.P., 2011. Size effects and stochastic behavior of nanoindentation pop in. Phys. Rev. Lett. 106, 1–4. https://doi.org/10.1103/PhysRevLett.106.165502

[60] Nix, W.D., Gao, H., 1998. Indentation Size Effects in Crystalline Materials: A Law for Strain Plasticity. J. Mech. Phys. Solids 46, 411-425.https://doi.org/10.1016/S0022-5096(97)00086-0

[61] Oliver, G.M., Pharr, W.C., 1992. Measurement of Thin Film Mechanical Properties Using Nanoindentation. MRS Bull. 17, 28–33. https://doi.org/10.1557/S0883769400041634

[62] Oliver, W.C., Pharr, G.M., 2004. Measurement of hardness and elastic modulus by instrumented indentation: Advances in understanding and refinements to methodology. J. Mater. Res. 19, 3–20. https://doi.org/10.1557/jmr.2004.19.1.3

[63] Orowan, E., 1934. Zur Kristallplastizität. I - Tieftemperaturplastizität und Beckersche Formel. Zeitschrift für Phys. 89, 605–613. https://doi.org/10.1007/BF0134147

[64] Pan, J., Rice, J.R., 1983. Rate sensitivity of plastic flow and implications for yield-surface vertices. Int. J. Solids Struct. 19, 973–987. https://doi.org/10.1016/0020-7683(83)90023-9

[65] Patil, S.D., 2009. Constraint Effects on Stationary Crack Tip Fields in Ductile Single Crystals.

[66] Peirce, D., Asaro, R.J., Needleman, A., 1983. Material rate dependence and localized deformation in crystalline solids. Acta Metall. 31, 1951–1976. https://doi.org/10.1016/0001-6160(83)90014-7

[67] Pharr, G.M., Bolshakov, A., 2002. Understanding nanoindentation unloading curves. J. Mater. Res. 17, 2660–2671. https://doi.org/10.1557/JMR.2002.0386

[68] Pharr, G.M., Herbert, E.G., Gao, Y., 2010. The indentation size effect: A critical examination of experimental observations and mechanistic interpretations. Annu. Rev. Mater. Res. 40, 271–292. https://doi.org/10.1146/annurev-matsci-070909-104456

[69] Q. Ma, D.R.C., 2015. Size dependent hardness of silver single crystals Size dependent hardness of silver single crystals. J. Mater. Res. 10, 853–863. https://doi.org/10.1557/JMR.1995.0853

[70] Raineesh, K.P., Sairam, K., Rajesh, K., Prasad, K. E., Novel approach to characterize the deformation under Berkovich and spherical indentations: Study on Magnesium single crystals. PRMaterials. (manuscript under review)

[71] Remington, T.P., Ruestes, C.J., Bringa, E.M., Remington, B.A., Lu, C.H., Kad, B., Meyers, M.A., 2014. Plastic deformation in nanoindentation of tantalum: A new mechanism for prismatic loop formation. Acta Mater. 78, 378–393. https://doi.org/10.1016/j.actamat.2014.06.058

[72] Rice, J. R. (1971). Inelastic constitutive relations for solids: An internal-variable theory and its application to metal plasticity. Journal of the Mechanics and Physics of Solids, 19(6), 433–455. https://doi.org/10.1016/0022-5096(71)90010-X

[73] Schneider, A.S., Kaufmann, D., Clark, B.G., Frick, C.P., Gruber, P.A., Mönig, R., Kraft, O., Arzt, E., 2009. Correlation between critical temperature and strength of small-scale bcc pillars. Phys. Rev. Lett. 103, 1–4. https://doi.org/10.1103/PhysRevLett.103.105501

[74] Seeger, A., 2001. Why anomalous slip in body-centred cubic metals? Mater. Sci. Eng. A 319–321, 254–260. https://doi.org/10.1016/S0921-5093(01)00958-3

[75] Seeger, A., Wasserbäch, W., 2002. Anomalous Slip - a feature of High-Purity and Body-Centred Cubic and Metals. Phys. Stat. Sol. 189, 27–50.

[76] Seeger, A., 2004. Experimental evidence for the {110} ↔ {112} transformation of the screw-dislocation cores in body-centred cubic metals. Phys. Status Solidi Appl. Res. 201, 21–24. https://doi.org/10.1002/pssa.200409031

[77] Sherwood, P.J., Guiu, F., Kim, H.C., Pratt, P.L., 1967. Plastic Anisotropy of Tantalum, Niobium, and Molybdenum. Can. J. Phys. 45, 1075–1089. https://doi.org/10.1139/p67-079

[78] Shields, J., 2013. Applications of Molybdenum Metal and its Alloys, International Molybdenum Association (IMOA).

[79] Shin, C., Shim, S., 2012. Dislocation mechanisms of radius effect on displacement bursts during spherical nanoindentations. J. Mater. Res. 27, 2161–2166. https://doi.org/10.1557/jmr.2012.183

[80] Simmons, G., Wang, H., 1971. Single Crystal Elastic Constants and Calculated Aggregate Properties. A Handbook 320

[81] Smallman, R.E., Ngan, A.H.W., 2014. Introduction to Dislocations. Mod. Phys. Metall. 121–158. https://doi.org/10.1016/b978-0-08-098204-5.00004-3

[82] Smith, R., Christopher, D., Kenny, S.D., Richter, A., Wolf, B., 2003. Defect generation and pileup of atoms during nanoindentation of Fe single crystals. Phys. Rev. B - Condens. Matter Mater. Phys. 67, 1–10. https://doi.org/10.1103/PhysRevB.67.245405

[83] Stelmashenko, N.A., Walls, M.G., Brown, L.M., Milman, Y. V., 1993. Microindentations on W and Mo oriented single crystals: An STM study. Acta Metall. Mater. 41, 2855–2865. https://doi.org/10.1016/0956-7151(93)90100-7

[84] Swadener, J.G., George, E.P., Pharr, G.M., 2002. The correlation of the indentation size effect measured with indenters of various shapes. J. Mech. Phys. Solids 50, 681–694. https://doi.org/10.1016/S0022-5096(01)00103-X

[85] Schuh, C.A., 2006. Nanoindentation studies of materials. Mater. Today 9, 32–40. https://doi.org/10.1016/S1369-7021(06)71495-X

[86] Tabor, D., 1951. The Hardness of Metals, Clarendon Press, Oxford.

[87] Taylor, G.I., 1934. The mechanism of plastic deformation of crystals. Part I.—Theoretical. Proc. R. Soc. London. Ser. A. 145 (855): 362-387. https://doi:10.1098/rspa.1934.0106

[88] Vitek, V., A, P.R.S.L., 1976. Computer simulation of the screw dislocation motion in b. c. c. metals under the effect of the external shear and uniaxial stresses. Proc. R. Soc. London. A. Math. Phys. Sci. 352, 109–124. https://doi.org/10.1098/rspa.1976.0166

[89] Vitek, V., Mrovec, M., Gröger, R., Bassani, J.L., Racherla, V., Yin, L., 2004. Effects of non-glide stresses on the plastic flow of single and polycrystals of molybdenum. Mater. Sci. Eng. A 387–389, 138–142. https://doi.org/10.1016/j.msea.2004.04.066

[90] Voyiadjis, G.Z., Almasri, A.H., Park, T., 2010. Experimental nanoindentation of BCC metals. Mech. Res. Commun. 37, 307–314. https://doi.org/10.1016/j.mechrescom.2010.02.001

[91] Wang, Y.M., Hodge, A.M., Biener, J., Hamza, A. V., Barnes, D.E., Liu, K., Nieh, T.G., 2005. Deformation twinning during nanoindentation of nanocrystalline Ta. Appl. Phys. Lett. 86, 1–3. https://doi.org/10.1063/1.1883335

[92] Wang, L., Bei, H., Li, T.L., Gao, Y.F., George, E.P., Nieh, T.G., 2011. Determining the activation energies and slip systems for dislocation nucleation in body-centered cubic Mo and face-centered cubic Ni single crystals. Scr. Mater. 65, 179–182. https://doi.org/10.1016/j.scriptamat.2011.03.036

[93] Woodward, C., Rao, S.I., 2001. Ab-initio simulation of isolated screw dislocations in bcc Mo and Ta. Philos. Mag. A Phys. Condens. Matter, Struct. Defects Mech. Prop. 81, 1305–1316. https://doi.org/10.1080/01418610108214442

[94] Xie, C.L., Ghosh, S., Groeber, M., 2004. Modeling cyclic deformation of HSLA steels using crystal plasticity. J. Eng. Mater. Technol. Trans. ASME 126, 339–352. https://doi.org/10.1115/1.1789966

[95] Yang, B., Vehoff, H., 2007. Dependence of nanohardness upon indentation size and grain size - A local examination of the interaction between dislocations and grain boundaries. Acta Mater. 55, 849–856. https://doi.org/10.1016/j.actamat.2006.09.004

[96] Yao, W.Z., Krill, C.E., Albinski, B., Schneider, H.C., You, J.H., 2014. Plastic material parameters and plastic anisotropy of tungsten single crystal: A spherical micro-indentation study. J. Mater. Sci. 49, 3705–3715. https://doi.org/10.1007/s10853-014-8080-z

[97] Yao, W.Z., You, J.H., 2017. Berkovich nanoindentation study of monocrystalline tungsten: a crystal plasticity study of surface pile-up deformation. Philos. Mag. 97, 1418–1435. https://doi.org/10.1080/14786435.2017.1299237

[98] Zhang, L., Ohmura, T., 2014. Plasticity initiation and evolution during nanoindentation of an iron-3% silicon crystal. Phys. Rev. Lett. 112, 1–5. https://doi.org/10.1103/PhysRevLett.112.145504

[99] Zhao, J., Wang, F., Huang, P., Lu, T.J., Xu, K.W., 2014. Depth dependent strain rate sensitivity and inverse indentation size effect of hardness in body-centered cubic nanocrystalline metals. Mater. Sci. Eng. A 615, 87–91. https://doi.org/10.1016/j.msea.2014.07.057

[100] Zong, Z., Lou, J., Adewoye, O.O., Elmustafa, A.A., Hammad, F., Soboyejo, W.O., 2006. Indentation size effects in the nano- and micro-hardness of fcc single crystal metals. Mater. Sci. Eng. A 434, 178–187. https://doi.org/10.1016/j.msea.2006.06.137